The old, unique C1 chondrite Flensburg – Insight into the first processes of aqueous alteration, brecciation, and the diversity of water-bearing parent bodies and lithologies

Addi Bischoff [a,*], Conel M. O'D. Alexander [b], Jean-Alix Barrat [c], Christoph Burkhardt [a], Henner Busemann [d], Detlev Degering [e], Tommaso Di Rocco [f], Meike Fischer [f,g], Thomas Fockenberg [h], Dionysis I. Foustoukos [b], Jérôme Gattacceca [i], Jose R.A. Godinho [j], Dennis Harries [k], Dieter Heinlein [l], Jan L. Hellmann [a], Norbert Hertkorn [m], Anja Holm [a], A.J. Timothy Jull [n,o], Imene Kerraouch [a], Ashley J. King [p,q], Thorsten Kleine [a], Dominik Koll [r], Johannes Lachner [s], Thomas Ludwig [t], Silke Merchel [s], Cornelia A.K. Mertens [d], Précillia Morino [d], Wladimir Neumann [t], Andreas Pack [f], Markus Patzek [a], Stefan Pavetich [r], Maximilian P. Reitze [a], Miriam Rüfenacht [d], Georg Rugel [s], Charlotte Schmidt [t], Philippe Schmitt-Kopplin [n,u], Maria Schönbächler [d], Mario Trieloff [t], Anton Wallner [r,s], Karl Wimmer [v], Elias Wölfer [a]

[a] Institut für Planetologie, University of Münster, Wilhelm-Klemm Str. 10, D-48149 Münster, Germany
[b] Earth and Planets Laboratory, Carnegie Institution of Washington, Washington, DC 20015, USA
[c] Université de Bretagne Occidentale, Institut Universitaire Européen de la Mer, Place Nicolas Copernic, F-29280 Plouzané Cedex, France
[d] Institute of Geochemistry and Petrology, ETH Zürich, Clausiusstraße 25, CH-8092 Zurich, Switzerland
[e] VKTA – Strahlenschutz, Analytik & Entsorgung Rossendorf e. V, Bautzner Landstraße 400, D-01328 Dresden, Germany
[f] Universität Göttingen, Geowissenschaftliches Zentrum, Goldschmidtstr. 1, D-37077 Göttingen, Germany
[g] Max-Planck-Institut für Sonnensystemforschung, Justus-von-Liebig-Weg 3, D-37077 Göttingen, Germany
[h] Institut für Geologie, Mineralogie und Geophysik, Ruhr-Universität Bochum, D-44780 Bochum, Germany
[i] CNRS, Aix Marseille Univ, IRD, Coll France, INRAE, CEREGE, Aix-en-Provence, France
[j] Helmholtz-Zentrum Dresden-Rossendorf, Helmholtz Institute Freiberg for Resource Technology, Chemnitzer Str. 40, D-09599 Freiberg, Germany
[k] Friedrich-Schiller-Universität Jena, Institut für Geowissenschaften, Carl-Zeiss-Promenade 10, D-07745 Jena, Germany
[l] German Fireball Network, Lilienstraße 3, D-86156 Augsburg, Germany
[m] Helmholtz-Zentrum München, German Research Center for Environmental Health, Analytical BioGeoChemistry, Ingolstädter Landstraße 1, D-85764 Neuherberg, Germany
[n] University of Arizona AMS Laboratory, 1118 East Fourth St, Tucson, AZ 85721, USA
[o] Isotope Climatology and Environmental Research Centre (ICER), Institute for Nuclear Research, Hungarian Academy of Sciences, Bem ter 18/c, 4026 Debrecen, Hungary
[p] School of Physical Sciences, The Open University, Milton Keynes MK7 6AA, UK
[q] Department of Earth Sciences, Natural History Museum, Cromwell Road, London SW7 5BD, UK
[r] Department of Nuclear Physics, Research School of Physics, The Australian National University, Canberra, ACT 2601, Australia
[s] Helmholtz-Zentrum Dresden-Rossendorf, Bautzner Landstrasse 400, D-01328 Dresden, Germany
[t] Institut für Geowissenschaften, Klaus-Tschira-Labor für Kosmochemie, Universität Heidelberg, Im Neuenheimer Feld 234-236, D-69120 Heidelberg, Germany
[u] Chair of Analytical Food Chemistry, Technische Universität München, D-85354 Freising-Weihenstephan, Germany

ᵛ *RiesKraterMuseum, Eugene-Shoemaker-Platz 1, D-86720 Nördlingen, Germany*

Abstract

On September 12, 2019 at 12:49:48 (UT) a bolide was observed by hundreds of eye-witnesses from the Netherlands, Germany, Belgium, Denmark and the UK. One day later a small meteorite stone was found by accident in Flensburg. The presence of short-lived cosmogenic radionuclides with half-lives as short as 16 days proves the recent exposure of the found object to cosmic rays in space linking it clearly to the bolide event. An exceptionally short exposure time of ∼5000 years was determined. The 24.5 g stone has a fresh black fusion crust, a low density of <2 g/cm^3, and a magnetic susceptibility of logχ = 4.35 (χ in 10^{-9} m^3/kg). The rock consists of relict chondrules and clusters of sulfide and magnetite grains set in a fine-grained matrix. The most abundant phases are phyllosilicates. Carbonates (∼3.9 vol.%) occur as calcites, dolomites, and a Na-rich phase. The relict chondrules (often surrounded by sulfide laths) are free of anhydrous silicates and contain abundant serpentine. Lithic clasts are also surrounded by similar sulfide laths partly intergrown with carbonates. ^{53}Mn-^{53}Cr ages of carbonates in Flensburg indicate that brecciation and contemporaneous formation of the pyrrhotite-carbonate intergrowths by hydrothermal activities occurred no later than 4564.6 ± 1.0 Ma (using the angrite D'Orbigny as the Mn-Cr age anchor). This corresponds to 2.6 ± 1.0 or 3.4 ± 1.0 Ma after formation of CAIs, depending on the exact absolute age of CAIs. This is the oldest dated evidence for brecciation and carbonate formation, which likely occurred during parent body growth and incipient heating due to decay of ^{26}Al.

In the three oxygen isotope diagram, Flensburg plots at the ^{16}O-rich end of the CM chondrite field and in the transition field to CV-CK-CR chondrites. The mass-dependent Te isotopic composition of Flensburg is slightly different from mean CM chondrites and is most similar to those of the ungrouped C2 chondrite Tagish Lake. On the other hand, ^{50}Ti and ^{54}Cr isotope anomalies indicate that Flensburg is similar to CM chondrites, as do the ∼10 wt.% H$_2$O of the bulk material. Yet, the bulk Zn, Cu, and Pb concentrations are about 30% lower than those of mean CM chondrites. The He, Ne, and Ar isotopes of Flensburg show no solar wind contribution; its trapped noble gas signature is similar to that of CMs with a slightly lower concentration of ^{20}Ne$_{tr}$.

Based on the bulk H, C, and N elemental abundances and isotopic compositions, Flensburg is unique among chondrites, because it has the lightest bulk H and N isotopic compositions of any type 1 or 2 chondrite investigated so far. Moreover, the number of soluble organic compounds in Flensburg is even lower than that of the brecciated CI chondrite Orgueil.

The extraordinary significance of Flensburg is evident from the observation that it represents the oldest chondrite sample in which the contemporaneous episodes of aqueous alteration and brecciation have been preserved. The characterization of a large variety of carbonaceous chondrites with different alteration histories is important for interpreting returned samples from the OSIRIS-REx and Hayabusa 2 missions.

1. INTRODUCTION

On September 12, 2019 at 12:49:48 UT a daylight fireball was seen by hundreds of eye-witnesses from the Netherlands and Belgium and a few observers in Northern Germany, Denmark, and the UK. Soon after the event some incidental video recordings (dash, action and security cams) from the Netherlands and Germany appeared in the social media (e.g., Fig. 1a).

More than 580 reports by witnesses were collected by the International Meteor Organization (IMO) via their fireball reporting website operated by Mike Hankey of the American Meteor Society. The bolide at 14:49:48 CEST local time was also observed by one of the authors (A.P.) and was registered by one German AllSky6 meteor camera from Herford (AMS21), which can operate even during daylight hours (Fig. 1b; Fig. S1).

NASA-JPL's Center for Near Earth Object Studies (CNEOS) has released some basic data of the bolide event: The peak brightness of the fireball was reached over 54.5° N, 9.2° E at an altitude of about 42 km. The US Government Sensors determined that the meteoroid had an entry velocity of 18.5 km/s, and a total impact energy of 0.48 kt TNT; however, this latter value can only be regarded as a completely unexaminable estimate, since no details about the calculations are known.

One day after the fireball event, on Friday the 13th of September, a small meteorite was found by accident by Mr. Erik Due-Hansen on the lawn of his front garden in the southwestern part of Flensburg, Schleswig-Holstein, Germany (Fig. S2; coordinates: 54°45.6873′ N, 9°22.7353′ E = 54.761455° N, 9.378922° E) and on September 15th
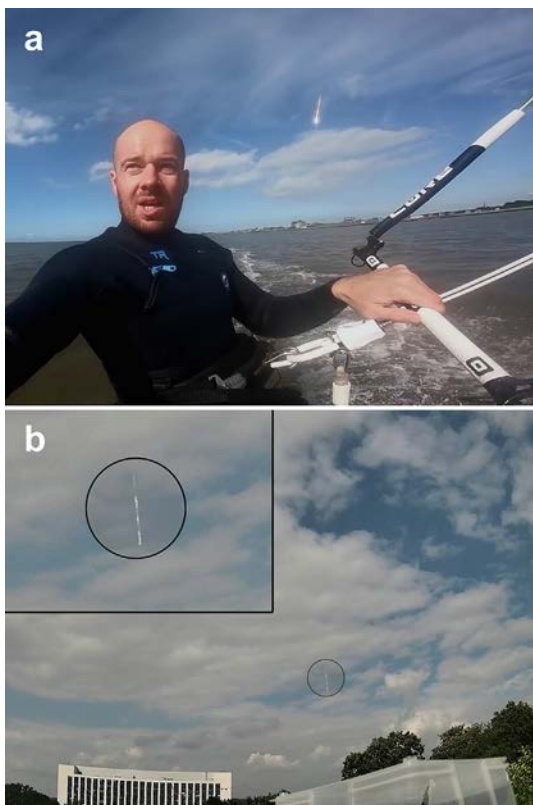
Fig. 1. The observed fireball of the meteoroid entering the atmosphere. (a) A kiteboarder from Bremerhaven recorded the fireball by accident from the mouth of the Weser river near Wremen. He did not hear a detonation sound and did not notice the bolide while filming and editing the action cam video. Image: Dorian Cieloch. (b) The daylight fireball is visible between clouds on this stacked image of a video recorded by the AllSky6 meteor camera AMS21 from Herford. The distance between the meteor camera and the visible part of the bolide is 230 km. Image: Jörg Strunk, Mike Hankey (American Meteor Society).

he reported the meteorite find to the IMO website. More details on the fireball event and on the post-recovery procedures are given in the "Supplementary Material" (SM). The finding of a fresh meteorite is supported by short-lived cosmogenic radionuclide detection by gamma-spectrometry.

In this study, details of the characteristics of Flensburg regarding its mineralogy, chemistry, isotopic and (cosmogenic) nuclide composition are summarized. In addition, some physical properties of the rock will be discussed, as well as details on its soluble organic components.

It was quickly recognized by electron microscopy that Flensburg consists almost entirely of hydrated phases or minerals precipitated from fluids (e.g., phyllosilicates, magnetite, carbonates, pyrrhotite, etc.). Thus, the meteorite was initially classified as an ungrouped C1 chondrite (The Meteoritical Bulletin no. 109). In this respect, Flensburg bears some similarities to those CI, CM, and CR chondrites that have also suffered high degrees of aqueous alteration (e.g., Fuchs et al., 1973; McSween, 1979a; Mackinnon and Zolensky, 1984; Rubin and Wasson, 1986; Tomeoka and Buseck, 1988; Zolensky and McSween, 1988;

Fredriksson and Kerridge, 1988; Grimm and McSween, 1989; Zolensky et al., 1989a,b, 1997, 2002; Endress and Bischoff, 1993; Johnson and Prinz, 1993; Browning et al., 1996; Bischoff, 1998; Brearley, 2006; Morlok et al., 2006; Rubin et al., 2007; Howard et al., 2009; Alexander et al., 2012, 2013; Tonui et al., 2014; Garenne et al., 2014; Visser et al., 2018).

However, as already stated in the Meteoritical Bulletin Database (https://www.lpi.usra.edu/meteor/metbull.php?-code=71098), differences exist between Flensburg and CI, CM, and CR chondrites, which will be discussed in detail in this study in order to achieve an appropriate classification.

2. SAMPLES AND SUMMARY OF METHODS

To date (October 2020), only one piece with a total mass of 24.5 g has been recovered within the fall area (Fig. 2; Fig. S2). Several thin and thick sections were prepared and stored at the Institut für Planetologie, Wilhelms-Universität Münster (two large ones PL19171 ($\sim$71 mm^2) and PL19172 ($\sim$132 mm^2) and two small sections (PL19173 ($\sim$13 mm^2) and PL19174 ($\sim$16 mm^2)).

Different analytical methods were applied to analyze the rock and to classify this meteorite. Here, a brief summary of most of the methods applied is given, and further details are included in the Supplement Material (SM).

After initial scanning electron microscopic (SEM) studies on the complete piece in Münster, the meteorite was cut with a saw into two pieces. The smaller piece of about 6.5 g was broken. To provide representative material for a number of bulk analytical methods, a fusion-crust-free chip from the broken 6.5 g piece of approximately 1 g was crushed using an agate pestle and mortar.

Detailed SEM studies on polished thin and thick sections were performed in Münster and at the Friedrich-Schiller-Universität in Jena, while focused ion beam (FIB) work and transmission electron microscope (TEM) studies on the section PL19173 were performed only in Jena using a FEI Quanta 3D FEG FIB-SEM workstation and a FEI Tecnai G2 with a field emission gun (FEG), respectively. Microprobe analyses (EPMA) were done with a JEOL JXA 8530F in Münster, whereas X-ray computed microtomography (CT) studies were performed at the Helmholtz Institute Freiberg for Resource Technology. By this technique, the 3D microstructures within the rock were deciphered and several phases could be distinguished, e.g. sulfides, silicates, and pores, based on the phase density. A CT scan with 11.7 μm voxel size of the larger part (17.0 g) of the meteorite was performed and processed.

Cosmogenic as well as primordial radionuclide concentrations were analyzed on the complete piece by non-destructive gamma-spectrometry in the underground laboratory "Felsenkeller" (Niese et al., 1998) of the VKTA Rossendorf, and thereafter using a 35.60 mg aliquot of the $\sim$1 g bulk powder by destructive accelerator mass spectrometry (AMS) at the Helmholtz-Zentrum Dresden-Rossendorf for ^{10}Be and ^{26}Al (Rugel et al., 2016), and at the Australian National University, Canberra for ^{41}Ca and ^{60}Fe (Wallner et al., 2015), respectively. Additionally, ^{14}C was measured on a 25 mg homogenized bulk aliquot

at the University of Arizona AMS Laboratory (Jull et al., 2008).

A 104 mg aliquot taken from the homogenized ~1 g sample of the Flensburg meteorite was analysed for major and trace element concentrations by inductively-coupled plasma atomic emission spectrometry (ICP-AES) and inductively-coupled plasma sector field mass spectrometry (ICP-SFMS). The procedure is described by Barrat et al. (2012, 2015, 2016). The concentration reproducibility is generally much better than 5% at the chondritic level.

Several aliquots of the ~1 g bulk powder, totalling about 40 mg were used to determine the bulk water/OH content and C concentration at the University of Bochum (see details in SM). Roughly 4 mg and 16 mg aliquots were used to determine, respectively, the bulk H and the bulk C and N elemental and isotopic abundances using the methods outlined in Alexander et al. (2012, 2013; details in SM).

Bulk oxygen isotope compositions of three ~2 mg samples were obtained by means of laser fluorination. The details on the latter technique and normalization are reported in the SM and previously published studies (see Pack et al. (2016) and Peters et al. (2020) for the protocol and standardization).

Titanium and Cr isotope analyses on 20–50 mg samples of Flensburg were performed in Münster and at the ETH Zürich. Chromium and Ti analyses at the ETH Zürich were carried out on a single 26 mg aliquot of the Flensburg meteorite and used a Thermo Scientific Neptune Plus multi-collector inductively-coupled plasma mass spectrometer (MC-ICPMS). The analytical procedure is described in Bischoff et al. (2019b). In Münster, the Cr isotope data were obtained using a Thermo Scientific Triton Plus Thermal Ionization Mass Spectrometer, while the Te and Ti data were obtained using a Thermo Scientific Neptune Plus MC-ICPMS (details in SM).

The noble gas (He-Xe) isotopic compositions were analyzed in a small "S" and a large "L" aliquot (4.83 ± 0.03 and 18.880 ± 0.014 mg) of the ~1 g powder at ETH Zürich. For details on the techniques see Riebe et al. (2017). The noble gases were extracted by fusion at ~1700°C, which was confirmed to be complete by repeat extractions at ~1750°C. Blank corrections were <0.5% for He in both samples, <5% for Ne, <3.5% for ^{36,38}Ar, ~33% for ^{40}Ar, ~10% for ^{84}Kr, ~2% for ^{132}Xe in the small sample and <1.5% for Ne, ~1% for ^{36,38}Ar, ~6% for ^{40}Ar, ~3% for ^{84}Kr, ~0.6% for ^{132}Xe in the large sample, respectively.

Mn-Cr, C, and O isotope analyses of carbonates were performed by ion probe (SIMS; Cameca IMS 1280-HR) on thin section PL19172 at the Institute of Earth Sciences (University of Heidelberg), while infrared (IR) spectroscopy was performed in vacuum on thin sections at the IR/IS laboratory (Institut für Planetologie, Münster) using a Bruker Vertex 70v instrument with a Bruker A513 bidirectional reflectance stage with varying observation geometries to measure a bulk sample signal (details in SM). The magnetic properties of the rock were studied in
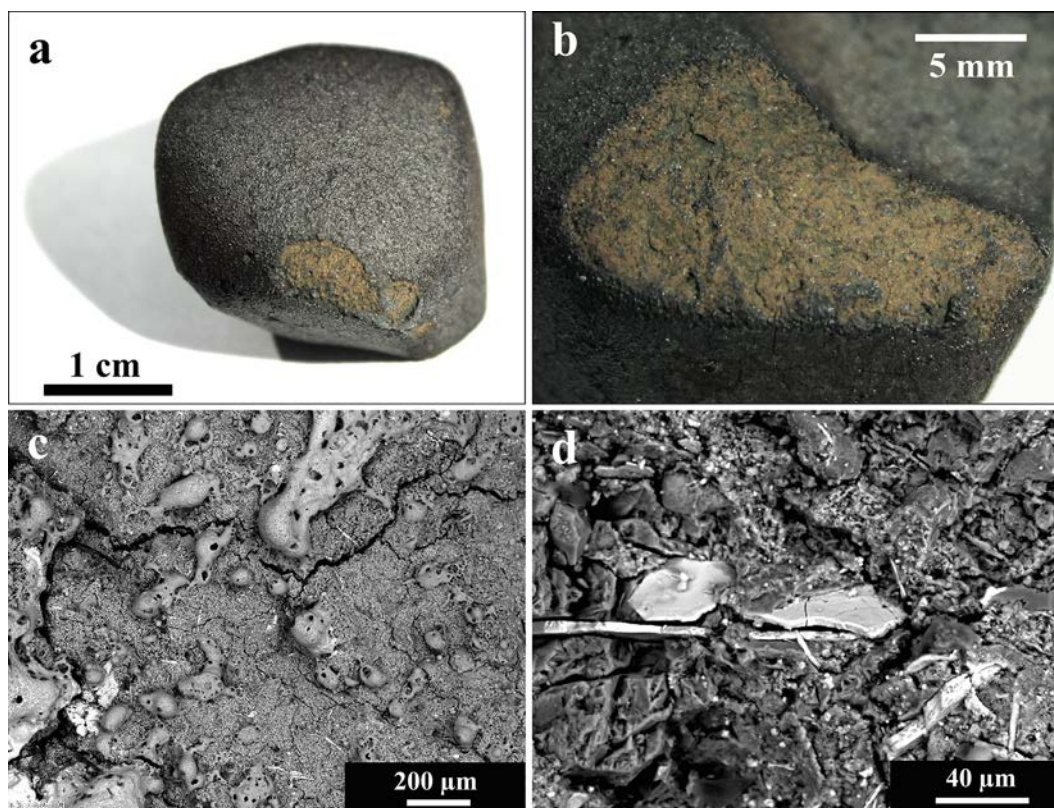

Fig. 2. (a) Bulk meteorite of Flensburg. (b) On parts of the rock, the fusion crust has been broken off. (c) BSE-image of a thin new (secondary) fusion crust that developed on the region where the primary fusion crust had broken off as shown in (b). Porous melt lumps partly cover the modified surface. (d) Sulfide plates (sheets) are visible on the rough broken surface of Flensburg (BSE-image).
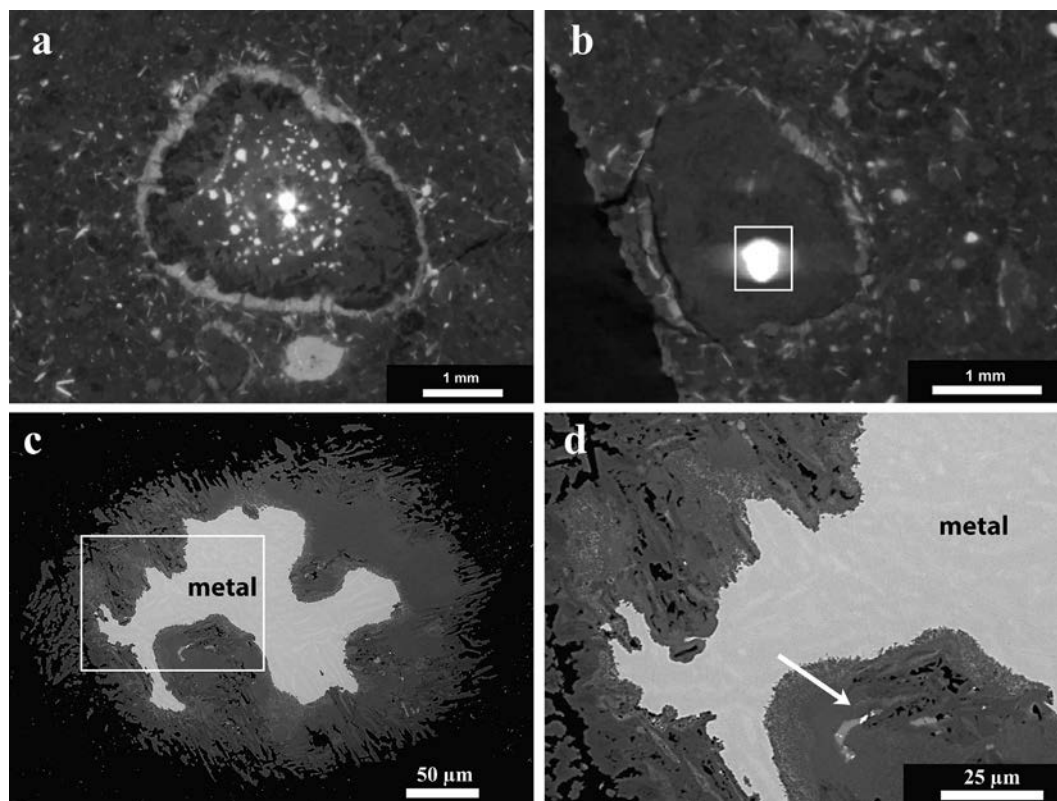
Fig. 3. (a) The largest object in Flensburg (about 3 mm) contains abundant small bright rounded particles indicating heavy element-rich phases. Heavy phases (but less dense than the white round particles) also surround the clast as visible by the light corona; CT-cross section; (b) A similar clast that appears to be internally homogeneous (except for the white blob), is surrounded by a light corona; CT-cross section; this object will be discussed in detail below; (c) within a polished thick section the large rounded, heavy element-rich inclusions of (b) consist of kamacite in its center surrounded by an Fe-oxide also containing considerable amounts of Si, S, and Ni; BSE-image. (d) Area of (c) showing an internal texture within the metal. The brighter areas have on average 8.5 wt.% Ni, while the darker metal has about 6 wt.% Ni. The Fe-rich oxides surrounding the metal core are very heterogeneous in terms of texture and composition. An As,S-rich Fe,Ni-grain is indicated by an arrow; BSE-image.

Aix-en-Provence and Nördlingen using different sample aliquots (bulk sample and later subsamples of 17.0 g, 3.5 g, and ∼0.3 g; details in SM).

The diversity of soluble organic components in the meteorite was obtained from the solid specimen as previously done for Murchison and other extraterrestrial soluble organic matter (SOM; Schmitt-Kopplin et al., 2010, 2012; Popova et al., 2013; Hertkorn et al., 2015). A single 20.6 mg fragment of Flensburg was divided into several aliquots; two pieces (∼5 mg each) were used for Fourier transform ion cyclotron resonance (FTICR) mass spectrometry and nuclear magnetic resonance (NMR) spectroscopy.

The thermal evolution of the Flensburg parent planetesimal was modelled using a 1D thermal evolution code (Neumann and Kruse, 2019; Neumann et al., 2020) adapted to a carbonaceous chondritic composition specific to the Flensburg meteorite (see details in SM).

3. MINERALOGY AND PETROGRAPHY

3.1. Hand specimen observations

A meteorite with a total mass of 24.5 g (roughly 3.5 cm × 3.2 cm × 2.4 cm in size) and a density of 1.984

± 0.016 g/cm^3 was recovered. The rock has a fresh black fusion crust that contains brownish patches (Fig. 2a and b), where the crust has been broken off. SEM studies of these brownish areas revealed that these parts must have been removed in the atmosphere and covered by a thin new secondary fusion crust (Fig. 2c) that only partially covers the internal features and minerals (e.g., sulfide plates; Fig. 2d). No clear indication was found as to why these areas appear brownish in hand specimen.

3.2. CT-observation

The X-ray computed tomography studies showed a fine-grained-rock with some large obvious lithic clasts several mm in size (Fig. 3a and b). CT-cross sections revealed that the densest phase occurs as round inclusions (bright blobs) inside these objects, which are surrounded by light grey coronas including phases having relatively high atomic numbers (Fig. 3). The bright blob studied in a polished thick section from the object shown in Fig. 3b was identified as kamacite surrounded by an unidentified Fe-oxide containing some percent of Si, S, and Ni (Fig. 3c). The coexistence of isolated metal blobs and silicate components is a typical feature of CR chondrites, although the size

Table 1
The mean modal abundances (vol.%) and standard deviations (SD) of various phases in Flensburg determined here and in four CI chondrites (Alfing et al., 2019) by point-counting and through PSD-XRD analysis of a ~50 mg powdered sample. Ranges for CM1s are taken from King et al. (2017).

Phases	Point Counting			PSD-XRD*	
	Mean	SD	4 CIs (range in CIs)[#]	Flensburg	CM1s
Calcite	2.6	± 0.6		0.9 ± 0.6	
Dolomite	1.3	± 0.4		0.6 ± 0.5	
"Carbonates"	3.9	± 1.0	0.48 (0.08–0.99)	1.5 ± 1.1	0.4–1.7
Magnetite[**]	1.9	± 0.3	4.3 (3.4–5.0)	3.9 ± 2.2	2.0–3.3
Sulfides	3.8	± 0.9	1.01 (0.4–1.7)	3.1 ± 1.7	0.1–4.4
Others (metals, ilmenite, phosphate)	<0.2				
Phyllosilicates	90.2	± 0.8[##]	94.0 (93.2–94.9)	91.5 ± 4.4	84.3–90.0

[#] Alfing et al. (2019) determined only grains >5 μm.
[##] Phyllosilicates and porosity were determined by difference.
[*] Uncertainties for the PSD-XRD analysis are relatively high due to the short measurement time and overlap between diffraction peaks (e.g., magnetite and Fe-sulfide peaks, since Flensburg has a relatively high abundance of sulfides).
[**] Includes traces of chromite.

ranges of the constituents are different. The kamacite consists of two lamellae-like areas of different compositions. Both contain about 0.5 wt.% Si, but the brighter areas have about 8.5 wt.% Ni, while 6 wt.% Ni were analyzed for the darker ones.

3.3. General petrology and mineralogy

Based on SEM and EPMA analyses of the thin sections, here we summarize the main petrological and mineralogical features of Flensburg. Rounded to ellipsoidal relict chondrules (~0.05–1 mm in apparent diameter) and clusters of sulfide and magnetite grains are set in a dark, fine-grained matrix. Ca,Al-rich inclusions (CAIs) were not found, but irregularly-shaped, phyllosilicate-rich aggregates are present that optically resemble fine-grained CAIs or AOAs (Fig. S3; Holm, 2020). In an area of 15 mm^2, the sizes and abundances of all relict chondrules were determined: The 134 relict chondrules have a mean size of 168 μm revealing an abundance of ~20 vol.% (see SM for details). The most abundant phases are phyllosilicates (~90 vol.% (including porosity); Table 1). TEM studies (see below) indicate that tochilinite is rare or absent. Locally the matrix contains some S, but this may result from the presence of nano-sized sulfide grains. Magnetite mainly occurs as aggregates. Carbonate grains exhibit a diverse mineralogy, including calcites, Mn-bearing dolomites, and a Na-rich phase. The relict chondrules are free of any anhydrous silicates (such as olivine and pyroxene), contain abundant phyllosilicates and carbonates, and are often surrounded by sulfide laths (Fig. 4). These laths consist of exsolved troilite within non-stoichiometric pyrrhotite. Pentlandite is absent in the laths, but occurs as separate grains in the matrix. In addition to the relict chondrules, lithic fragments are also present (Fig. 4e and f). The lithic fragment shown in Fig. 4f has a well-preserved chondritic texture and is surrounded by abundant sulfide laths that are similar to those around relict chondrules. The relevance of these observations will be discussed in Section 7.11.

The modal mineral abundances obtained by optical means given in Table 1 are the averages of four independent

analyses determined by means of point counting (in all cases more than 1500 points were registered on areas of different sizes ranging from 8 mm^2 to 20 mm^2 covering a total area of about 56 mm^2). The data are slightly different to the results obtained by X-ray techniques. A total abundance of ~3.8 vol.% sulfides and ~1.9 vol.% magnetite was obtained from point counting. All these phases are heterogeneously distributed throughout the Flensburg meteorite. Minor amounts of chromite, ilmenite, Ca-phosphate (Fig. S3; Holm, 2020), and traces of a Fe,Ni,As(Te,S)-rich phase (see below) were also detected.

3.3.1. Carbonates

The point counting suggests that carbonate abundances total about 4 vol.%, making them the second most abundant mineral group after that of the phyllosilicates (Table 1). Three different carbonates occur: calcite, dolomite and a (rare) Na-rich carbonate (Fig. 5). Representative carbonate compositions are given in Table S1.

3.3.2. Sulfides

Three major sulfides are observed in Flensburg: Pyrrhotite, troilite, and pentlandite. Their total abundance is about 3.8 vol.%. In general, pyrrhotite and troilite occur as small-scale lamellar intergrowths (Fig. 6), whereas the pentlandites occur as individual grains in the matrix. Representative compositions determined by EPMA are given in Table S2. The composite crystals of pyrrhotite/troilite are tabular to lath-shaped and are distributed in the matrix as well as rimming chondrules and larger objects (Fig. 4). Often, the crystals are surrounded by phyllosilicate sheaths and occasionally they are embedded in carbonates (Fig. 5a). In order to obtain details on the pyrrhotite/troilite intergrowth and to resolve their relationship to the surrounding phyllosilicates, three FIB sampling sites were selected to target sulfide crystals and adjacent phyllosilicates of interest. Representative compositions of sulfide minerals are given in Table S2.

The tabular to lath-shaped, low-Ni iron sulfide crystals are predominantly non-stoichiometric pyrrhotite [$(Fe,Ni)_{1-x}S$; $x \leq 0.09$] with variable amounts of exsolved troilite (FeS). The sizes and morphologies of the troilite
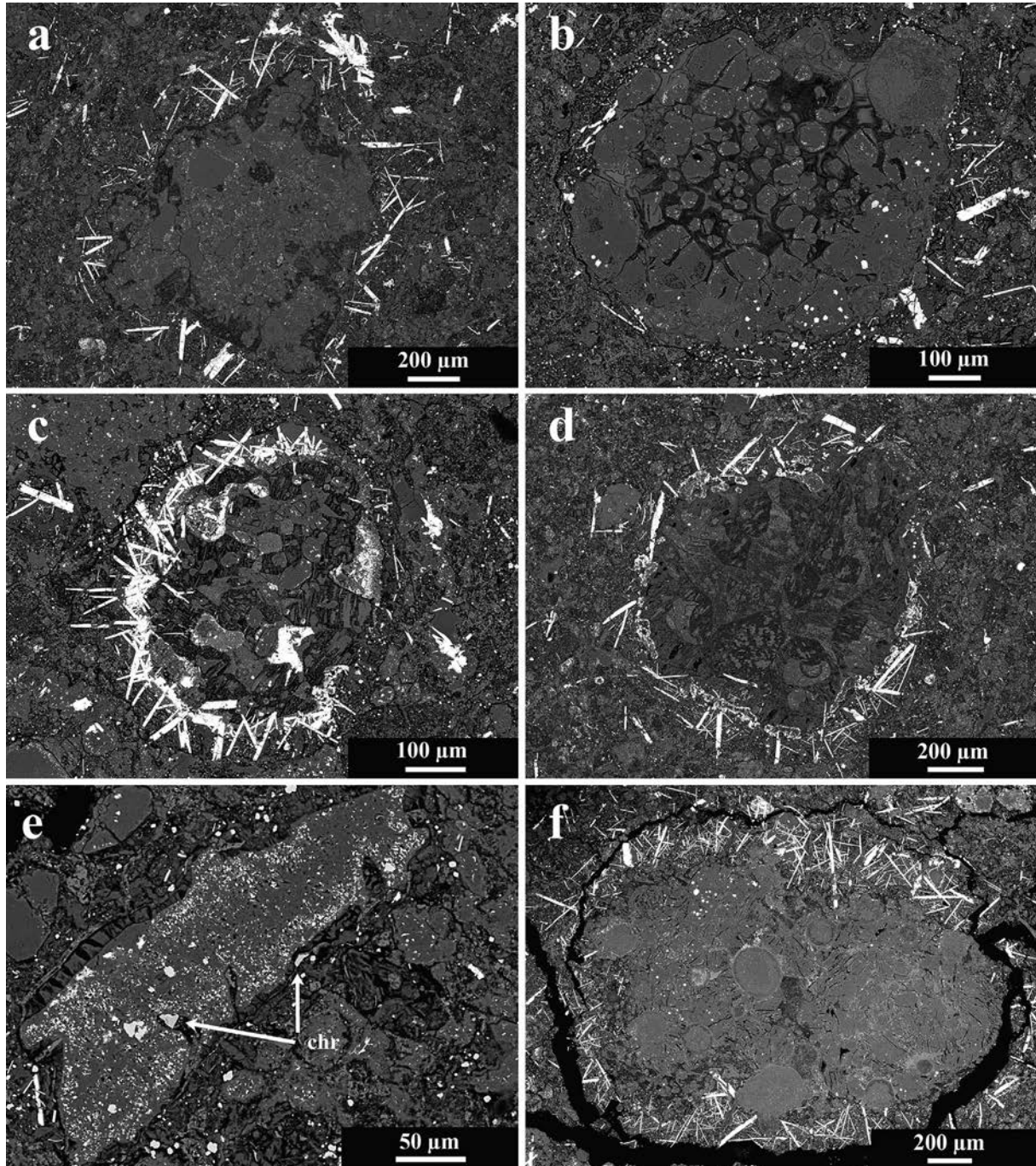
Fig. 4. BSE images of representative relict chondrules and fragments in Flensburg. The chondrules in (a)–(d) do not contain any olivine or pyroxene and often show abundant sulfide laths at their boundaries. (e) Vein-like fragment with abundant small magnetite grains and some large chromites. A reaction zone is clearly visible on the left-hand side. (f) One of the largest objects (shown in Fig. 3b; different slice) in the Flensburg meteorite. The clast has an internal "chondritic" texture that differs from that of the Flensburg host. The clast is consisting of about 20 relict chondrules of various sizes (all mafic silicates have been transformed into phyllosilicates). Thus, it is an impact-generated fragment in the bulk rock and completely surrounded by a zone that is rich in sulfide laths.

exsolution lamellae vary considerably (Figs. 6 and 7), from lenticular bodies just a few nm wide to flame-like lamellae several μm wide and up to 30 μm long. The former are hardly visible even in TEM images (sample F02), but become apparent as diffuse superstructure reflections in selected area electron diffraction (SAED) patterns

(Fig. 7). The coexisting pyrrhotite shows diffuse reflections, indicating that troilite exsolved from an initial monosulfide solid solution (MSS), which was the original state of the sulfide crystals during formation.

The superstructure reflections of pyrrhotite arise from the ordering of Fe-site vacancies and can be understood
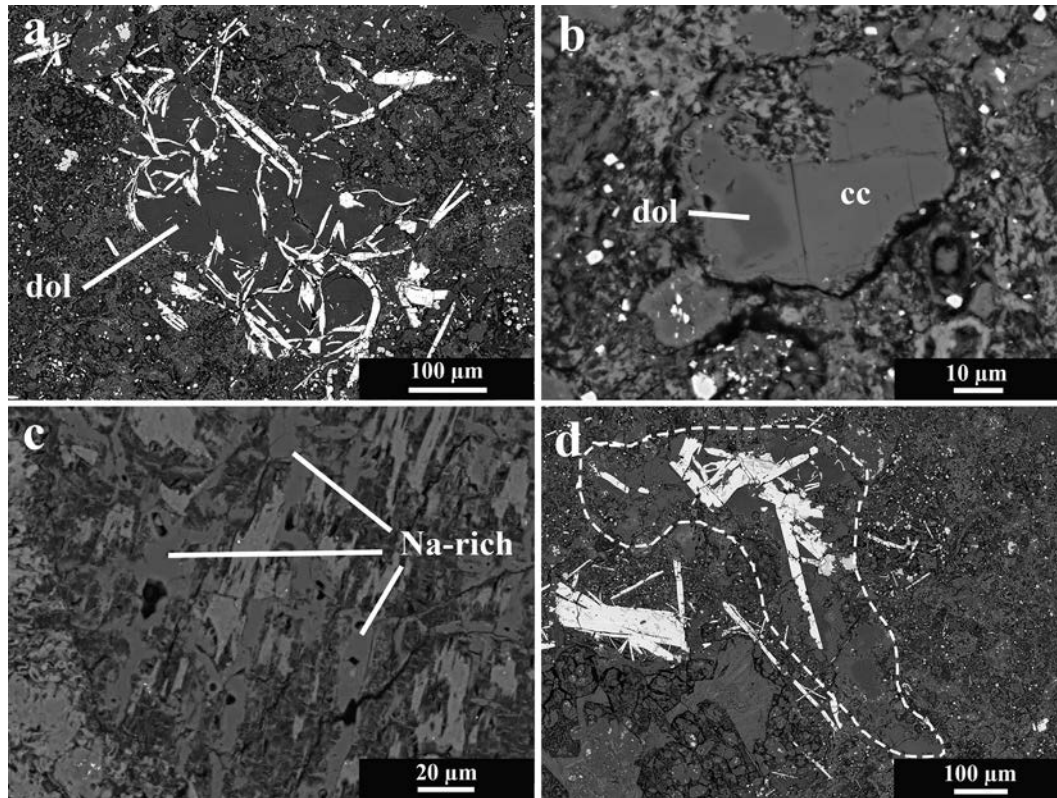
Fig. 5. Carbonates in Flensburg; (a) dolomite-pyrrhotite intergrowth; (b) dolomite (dol) embedded within calcite (cc); (c) oriented Na-rich carbonates (Na-rich) in a replaced radial-pyroxene chondrule (?); (d) carbonate vein (indicated by dashed lines) consisting of dolomite and calcite embedding sulfide laths. BSE-images.
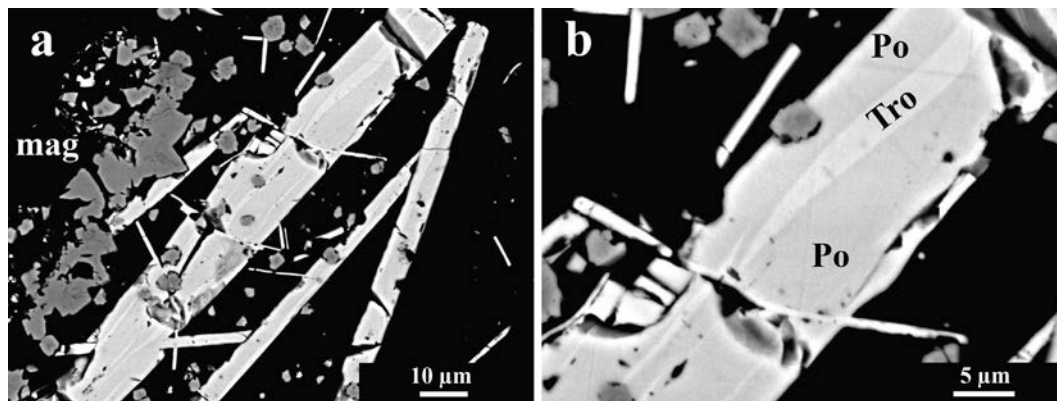

Fig. 6. (a) Typical appearance of exsolved troilite (Tro) within pyrrhotite (Po); (b) detail of (a); mag = magnetite; BSE-image.

as a quasi-periodic structural modulation that is characterized by the repeat parameter N along the crystallographic c axis (Harries et al., 2011). As in many cases of NC-pyrrhotites (Harries and Langenhorst, 2013), N is a non-integral number between 4 and 6. TEM samples F01 and F03 show unusual and variable superstructure reflections of pyrrhotite that cannot be indexed consistently (Fig. 7a–c). In sample F02, the observed N value is consistently about 5.39 (Fig. 7c) and corresponds to an Fe-rich pyrrhotite composition close to $(Fe,Ni)_{0.91}S$, i.e. intermediate between $(Fe,Ni)_9S_{10}$ (5C-pyrrhotite) and $(Fe,Ni)_{11}S_{12}$

(6C-pyrrhotite). This agrees well with the compositions measured by EPMA (Table S2). Because the pyrrhotite-troilite exsolution assemblage contains abundant stoichiometric troilite, the metal/sulfur ratio must be >0.91 in the bulk sulfide and is estimated to be ~0.95 in most cases (i.e., about equal volume fraction of pyrrhotite and troilite).

The bulk Ni content of the pyrrhotite crystals typically ranges between 0.18 and 0.57 wt.% (Table S2; Fig. S4; mean molar $Ni/(Fe + Ni) \approx 0.004$), but some crystals show zones with no Ni detectable by TEM-EDS. No evidence for exsolved pentlandite was found in the pyrrhotite crystals
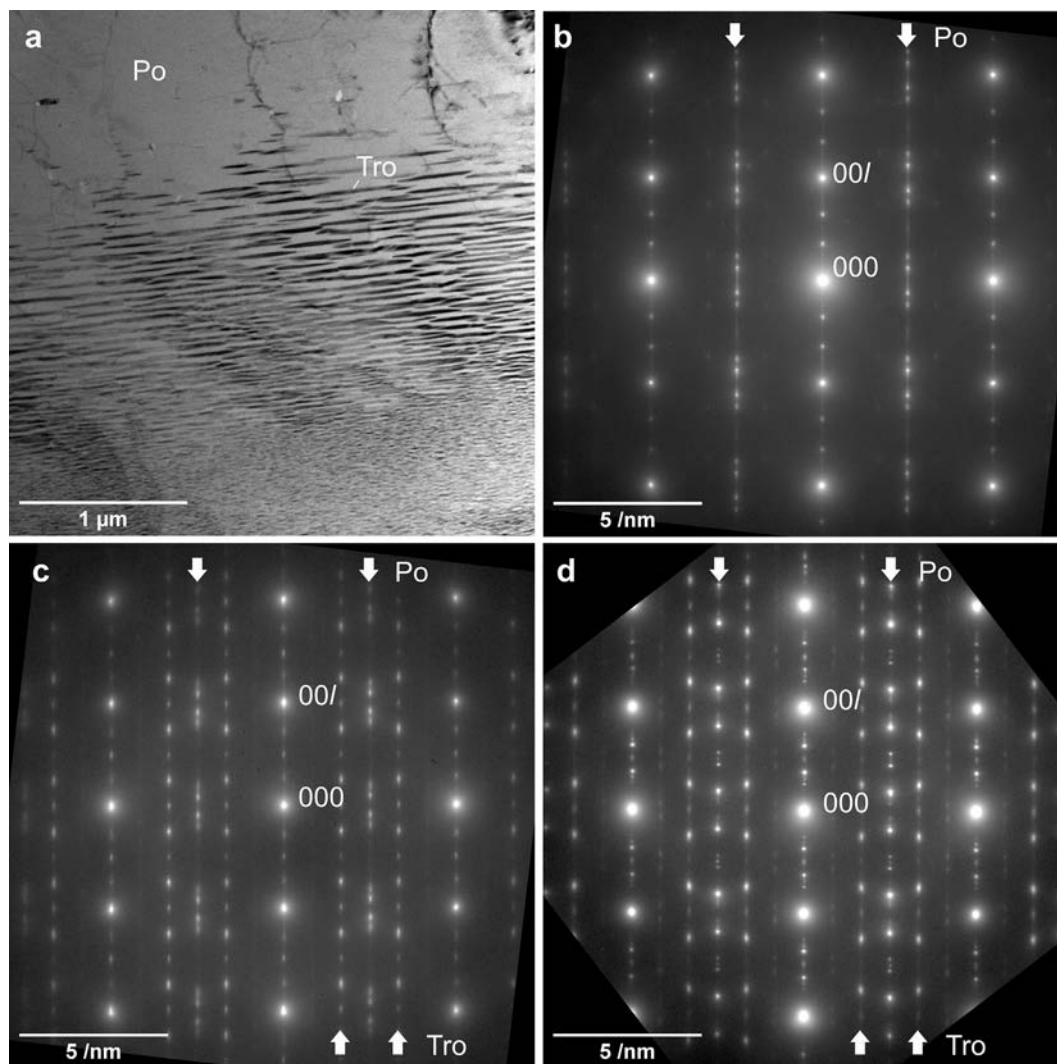
Fig. 7. TEM analysis of low-Ni iron sulfide in Flensburg. Po: pyrrhotite, Tro: troilite. (a) TEM bright-field image of dark (diffracting) troilite lamellae within pyrrhotite. The center of the crystal is at the top, the rim is close to the bottom. The change of troilite size and abundance likely reflects a chemical gradient of the metal/sulfur ratio. (b) SAED pattern of the troilite-poor region showing diffuse pyrrhotite reflections (arrows). (c) SAED pattern of the troilite-rich region showing additional troilite reflections. The pyrrhotite superstructures in (b) and (c) are distinct, but cannot be indexed with typical NC-pyrrhotite, possibly due to poor vacancy ordering or unusual coexisting ordering schemes. (d) SAED pattern from a different low-Ni iron sulfide crystal showing reflections of pyrrhotite and troilite. Here, the pyrrhotite can be consistently indexed as NC superstructure with $N \approx 5.39$, suggesting a bulk metal/sulfur ratio >0.91.

of Flensburg. In Flensburg, pentlandite only occurs as separate grains with molar Ni/(Fe + Ni) of 0.42 (EPMA) to 0.48 (TEM-EDS). Even at the TEM scale pentlandite grains show sharp boundaries with the surrounding matrix and no signs of alteration to other Ni-rich sulfides.

3.3.3. Phyllosilicates

TEM samples included phyllosilicates of three distinct compositional and morphological types within the Flensburg chondrite: sheath, vein, and matrix serpentine (Fig. S5; Table 2).

Sheath serpentine surrounds pyrrhotite as well-formed crystal stacks (Fig. 8a and b) that are subparallel to the tabular faces of the pyrrhotite crystals. It predominantly consists of lizardite-type serpentine that shows the characteristic 0.7 nm basal interplanar spacing. The sheath-

ing phyllosilicates of Flensburg do not display any intimate intermixing of serpentine and chlorite. Only one ~120 nm wide chlorite stack showing the characteristic 1.4 nm basal lattice spacing was found in sample F03 (Fig. 8c–f). A narrow stack showing ~1 nm basal lattice spacing in sample F01 is possibly a talc-like structure or a dehydrated/collapsed smectite-group phyllosilicate, but these appear to be rare. EDS measurements show that the sheath serpentine has a high atomic Mg/(Mg + Fe) ratio of ~0.85 and contains additional Na and Al. Attempts to quantify the Fe^{2+}/Fe^{3+} ratio by electron energy loss spectroscopy (EELS) failed due to rapid oxidation of the sample, probably due to H loss (Garvie et al., 2004). During cumulative spectrum acquisition, some initial Fe edge spectra showed evidence for Fe^{2+}, which rapidly changed to dominant Fe^{3+}. Based on TEM-EDS measurements (Table 2), crystal

Table 2
Averaged TEM-EDS analyses of distinct serpentine types in Flensburg. All data in wt.%; n.d. = not detected; O calculated assuming a molar Fe^{3+}/Fe_{total} that results in filled octahedral and tetrahedral sites, H calculated by stoichiometry (totals normalized to 100 wt.%). Detection limits of Ca, V, Ti, and Ni are about 0.05 to 0.1 wt.%, Mn is not detected below about 0.2 wt.% due to overlap of Cr $K\beta$.

	O	Na	Mg	Al	Si	Fe^{2+}	Fe^{3+}	Cr	H	Total
Sheath low-Al (n = 9)	49.4 ± 0.2	1.15 ± 0.25	18.9 ± 0.6	1.94 ± 0.13	18.4 ± 0.23	6.40 ± 0.41	2.13 ± 0.14	0.25 ± 0.06	1.38 ± 0.01	100
Sheath high-Al (n = 17)	49.6 ± 0.3	1.18 ± 0.45	19.1 ± 0.8	2.65 ± 0.21	18.1 ± 0.6	5.56 ± 0.51	1.85 ± 0.17	0.44 ± 0.21	1.39 ± 0.01	100
Vein high-Fe (n = 9)	48.9 ± 0.3	<0.05	19.0 ± 0.7	1.61 ± 0.23	18.4 ± 0.4	10.3 ± 0.81	n.d.	0.34 ± 0.11	1.37 ± 0.01	100
Vein low-Fe (n = 6)	50.8 ± 0.2	<0.05	23.7 ± 0.8	1.07 ± 0.10	19.2 ± 0.5	3.82 ± 0.30	n.d.	<0.05	1.42 ± 0.01	100
Matrix high-Fe (n = 10)	45.1 ± 2.0	~0.2	12.8 ± 3.2	1.40 ± 0.46	15.6 ± 1.1	18.2 ± 5.4	5.12 ± 1.5	~0.2	1.26 ± 0.06	100
Matrix low-Fe (n = 2)	48.1	0.46	16.6	1.03	18.9	13.1	n.d.	0.28	1.35	100

stoichiometry can be established by assuming ~25% of the total Fe being Fe^{3+} on octahedral and tetrahedral sites:

$$(Mg_{2.28},Fe^{2+}_{0.30},Al_{0.17},Na_{0.15},Fe^{3+}_{0.07},Cr_{0.02})_{\Sigma 2.99}(Si_{1.89},Al_{0.08},Fe^{3+}_{0.03})_{\Sigma 2.00}O_5(OH)_4$$
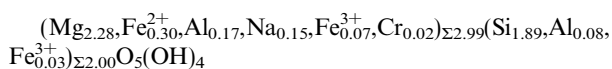
The high Na contents of 1–2 wt.% Na_2O are unusual for serpentines, but are balanced stoichiometrically via a coupled substitution with Al: The high Si occupancy on the tetrahedral sites does not allow for much Tschermak-type charge compensation $(M^{2+}_{oct} + Si^{4+}_{tet} = M^{3+}_{oct} + M^{3+}_{tet})$ and, therefore, the high Al contents must be assigned to the octahedral sites. This is consistent with the observed Na contents, which provide additional charge compensation by monovalent ions on the octahedral sites $(2\,M^{2+}_{oct} = M^{3+}_{oct} + M^{+}_{oct})$.

Vein serpentine forms short, vein-like structures several tens of μm in length within the matrix and is composed of interlocking stacks of lizardite-type serpentine crystals reaching sizes on the order of 10 μm (Fig. 8g and h). Compared to the sheathing phyllosilicates, the vein serpentine contains almost no Na and shows zonal variations of the Mg/Fe ratio, from $(Mg_{2.76},Fe^{2+}_{0.19},Al_{0.06})_{\Sigma 3.01}(Si_{1.94},Al_{0.06})_{\Sigma 2.00}O_5(OH)_4$ in the Mg-rich center of crystals to $(Mg_{2.30},Fe^{2+}_{0.54},Al_{0.08},Cr_{0.02},Na_{0.01})_{\Sigma 2.95}(Si_{1.93},Al_{0.09})_{\Sigma 2.02}O_5(OH)_4$ in Fe-rich outer zones (Table 2). As described above, EELS quantification of the Fe^{2+}/Fe^{3+} ratio was inconclusive. Stoichiometric balancing suggests that there is little Fe^{3+}, as it would produce excess occupancy of the tetrahedral sites and a deficit on the octahedral sites. This observation also points to a distinct phase of phyllosilicate formation relative to the sheath serpentine.

Matrix serpentine constitutes fine-grained, highly porous material (Fig. 9a and b; Table 2). Most of it appears to be lizardite-type stacks of <1 μm in size, often randomly arranged to form interlocking, felty aggregates (Fig. 9c

and d). TEM investigations did not show unambiguous evidence for chrysotile-type serpentine, although some smaller, elongated particles (<200 nm long) in the matrix might be tubular or curled serpentine. The matrix serpentine contains more Fe than the other two occurrences of serpentine described above, but the Mg/Fe ratios vary considerably. In the Mg-rich matrix serpentine there seems to be little to no Fe^{3+}, indicated by high Si contents:

$$(Mg_{2.04},Fe^{2+}_{0.70},Al_{0.08},Na_{0.06},Cr_{0.02})_{\Sigma 2.90}(Si_{2.01},Al_{0.03})_{\Sigma 2.04}O_5(OH)_4.$$
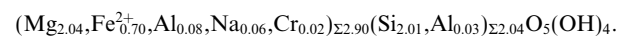
The Fe-rich matrix serpentine appears to have about 20–25% of its total Fe as Fe^{3+}, as indicated by its low Si contents:

$$(Mg_{1.67},Fe^{2+}_{1.05},Fe^{3+}_{0.15},Al_{0.09},Na_{0.02},Cr_{0.01})_{\Sigma 2.99}(Si_{1.78},Fe^{3+}_{0.15},Al_{0.08})_{\Sigma 2.00}O_5(OH)_4.$$

3.3.4. Magnetite and chromite

Based on point-counting, magnetite makes up about 1.9 vol.% of Flensburg (Table 1), whereas chromite is much less abundant (≪0.5 vol.%; Fig. 10). A high Si content was found in the magnetite, as well as high Ti in chromite (Table S3). Small grains of magnetite are dispersed throughout the matrix or occur in relict chondrules probably replacing metals.

In the FIB section (Fig. 11), magnetite occurs as small crystals in the matrix and as an overgrowth on a chromite grain. The magnetite is Si-bearing. In the composite grain, the magnetite epitactically overgrows the chromite grain. The chromite grain contains substantial amounts of Mg-spinel and ulvöspinel components, but no apparent Fe^{3+}. The average composition of the chromite is

$$(Fe^{2+}_{0.61},Mg_{0.39})(Cr_{0.90},Al_{0.81},Fe^{2+}_{0.13},Ti_{0.14})_{\Sigma 1.98}O_4.$$

At the TEM-scale, parts of the magnetite grains are chemically heterogeneous due to nanoscale inclusions
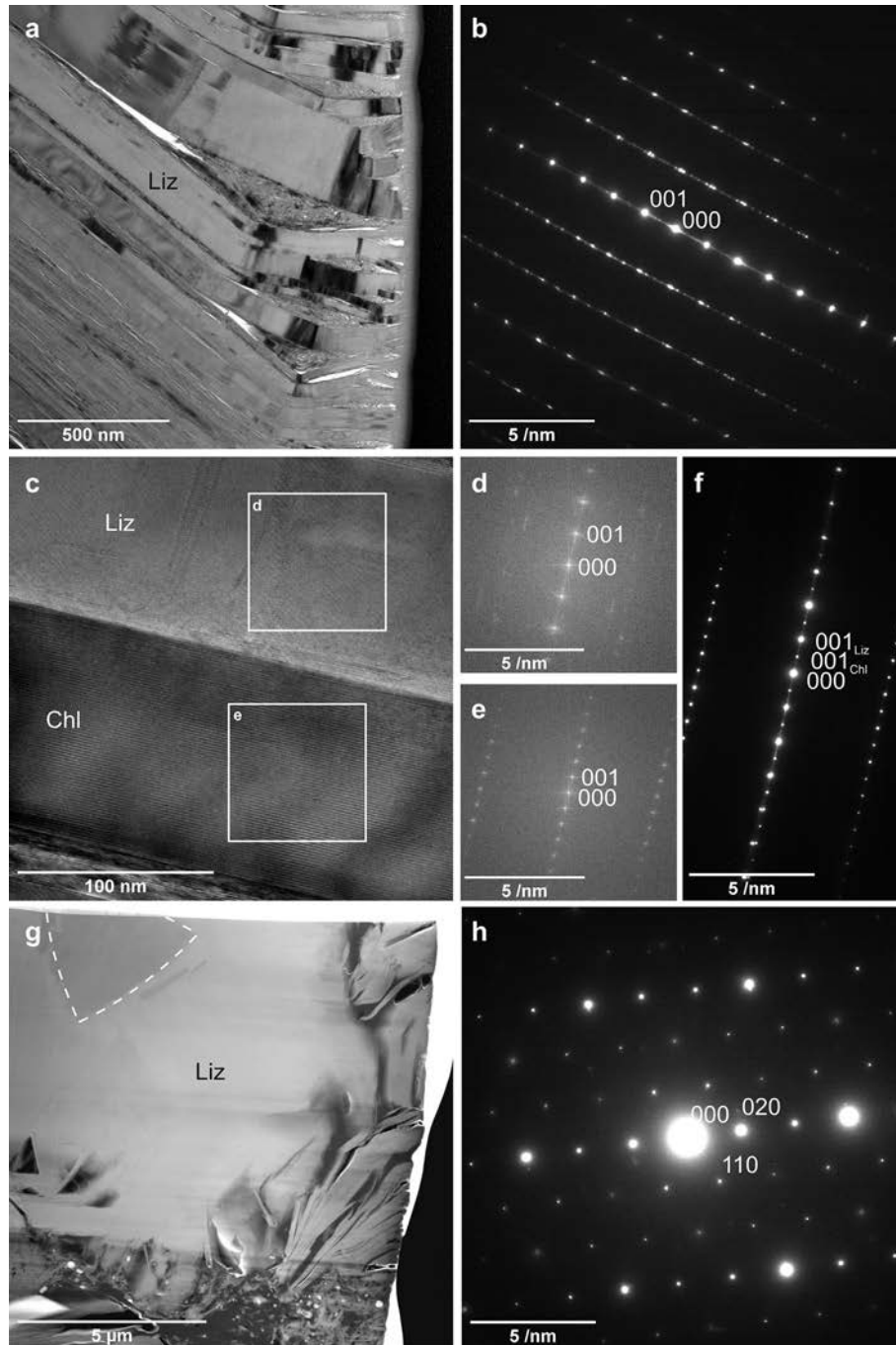
Fig. 8. TEM analysis of coarse-grained phyllosilicates in Flensburg. Liz: lizardite, Chl: chlorite. (a) Sheath serpentine surrounding a pyrrhotite crystal (out of view). The bending of lizardite stacks is probably due to the preparation of the thin section. (b) SAED pattern of the lizardite in (a), showing the characteristic 0.7 nm 001 interplanar spacing. (c) Isolated stack of chlorite about 120 nm thick in sheathing serpentine of Flensburg. The chlorite shows the characteristic 1.4 nm interplanar spacing and sharply borders lizardite. The boxes mark locations of Fast Fourier Transform (FFT) patterns shown in (d) and (e). (d) FFT pattern of lizardite in (c). (e) FFT pattern of chlorite in (c). (d) and (e) demonstrate the doubling of the periodicity in the chlorite stack. (f) SAED pattern of the mixed region of lizardite and chlorite. (g) Scanning TEM high-angle annular dark-field (STEM-HAADF) image of vein serpentine. The dashed line marks the Mg-rich core of the crystal, and the outer zone is Fe-rich. (h) SAED pattern of the serpentine crystal in (g) in the same orientation. The zone axis is perpendicular to the basal layer stacking and indexed for a monoclinic polytype due to the asymmetric intensity distribution.

(Fig. 11b). These inclusions appear to be Fe-rich silicates, but their compositions and mineralogies have not been determined conclusively. Regions of apparently inclusion-free magnetite also show elevated Si contents of about 0.22 atoms per formula unit, suggesting that Si is substituted into the structure.
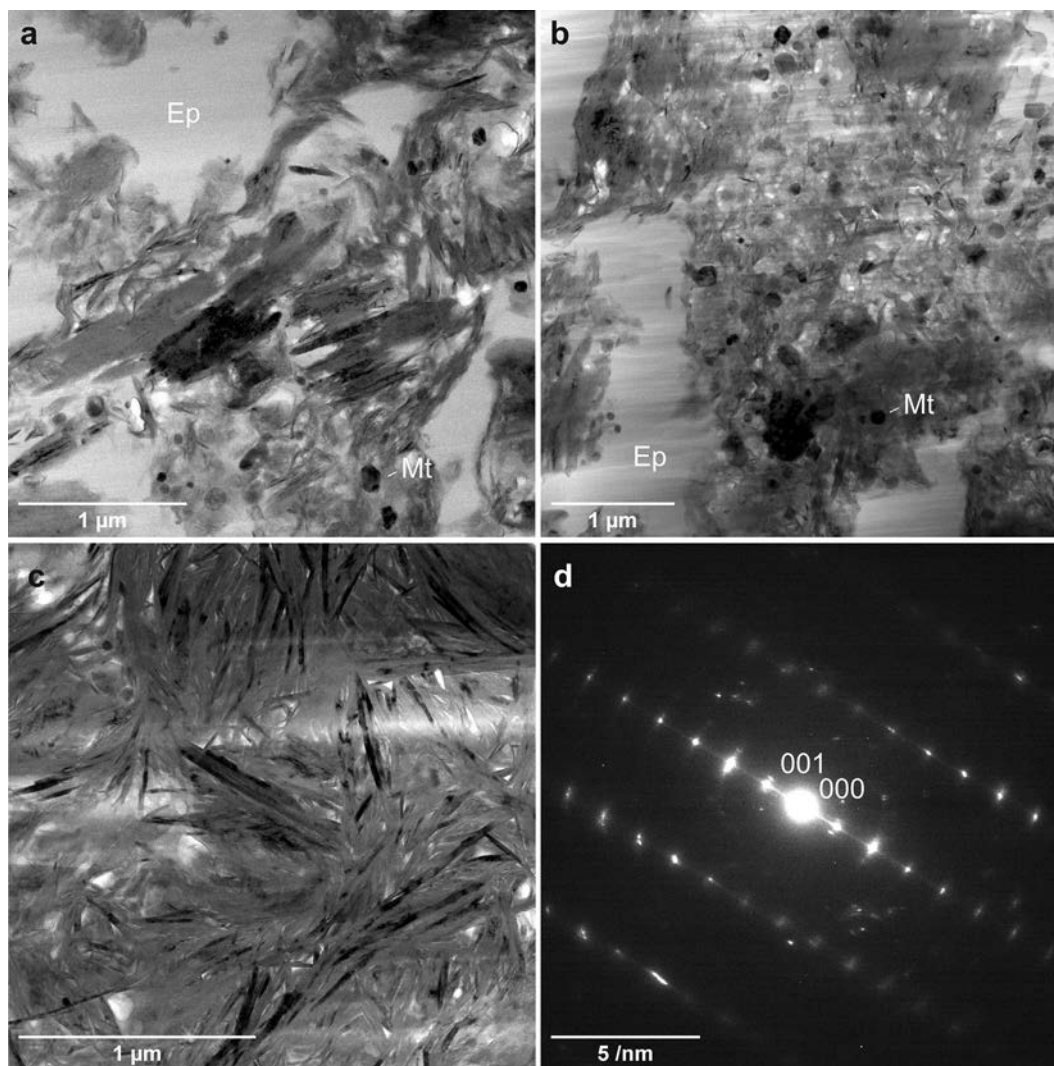
Fig. 9. TEM analysis of fine-grained matrix phyllosilicates in Flensburg. Ep: epoxy, Mt: magnetite. Subhorizontal streaks are due to FIB sample preparation. (a) Small stacks of lizardite and possibly tubular forms of serpentine. Small, rather isometric grains are mostly magnetite. The pore space is filled by epoxy resin. (b) Different location than in (a) showing smaller serpentine aggregates and more abundant magnetite. (c) Coarser-grained, relative Mg-rich matrix serpentine forming felty aggregates. These may be curled aggregates, but no clearly tubular cross-section has been found. (d) SAED pattern of the serpentine crystal in the center of (c).

3.4. Isotopic studies on carbonates

Concerning the O isotopes, the analyzed calcite grains in Flensburg range in $\delta^{18}O_{VSMOW}$ from $+13.5‰$ to $+32.4‰$ with $\Delta^{17}O_{VSMOW}$ ranging from -3.8 to $-1.1‰$ defining a line with a slope of ~0.62 (Fig. 12a, Table 3). There is no apparent systematic difference between calcite grains with different petrologic context, i.e. sulfide-associated calcite and zoned calcite grains overlap significantly. Typical calcite grains (in the matrix) exhibit a rather small range in $\delta^{18}O_{VSMOW}$ from $+13.5$ to $+24.3‰$ (Fig. 12b). The O isotope compositions of dolomite grains in Flensburg range from $+11.8$ to $+17.9‰$ in $\delta^{18}O_{VSMOW}$ with $\Delta^{17}O_{VSMOW}$ ranging from -4.1 to $-2.4‰$ defining a line with a slope of ~0.39 (Fig. 12a, Table 3). On average, the dolomite grains that are associated with sulfides tend to be more enriched in ^{16}O when compared to other dolomite grains (Fig. 12c).

Fig. 13a displays single spot simultaneous measurements of both C and O isotopic compositions (Schmidt, 2020; Table S4). Flensburg dolomites do not only show a limited range in O isotopic composition ($+11.8‰$ to $+17.9‰$ in $\delta^{18}O_{VSMOW}$), but are also restricted in C compositions ($+48‰$ to $+60‰$ in $\delta^{13}C_{VPDB}$), with sulfide associated dolomites tending to have both lighter O and C isotopic compositions. The calcites are compositionally more variable, extending to higher $\delta^{18}O_{VSMOW}$ and lower $\delta^{13}C_{VPDB}$ values in a seemingly uncorrelated and unsystematic way. There is no clear difference between isolated calcites or those associated with sulfides.

The decay system ^{53}Mn-^{53}Cr can be used to constrain the formation age of carbonates, because the carbonates are characterized by very high Mn/Cr ratios and, provided that they formed during the lifetime of ^{53}Mn, highly radiogenic $^{53}Cr/^{52}Cr$ ratios. Calcites and dolomites from the
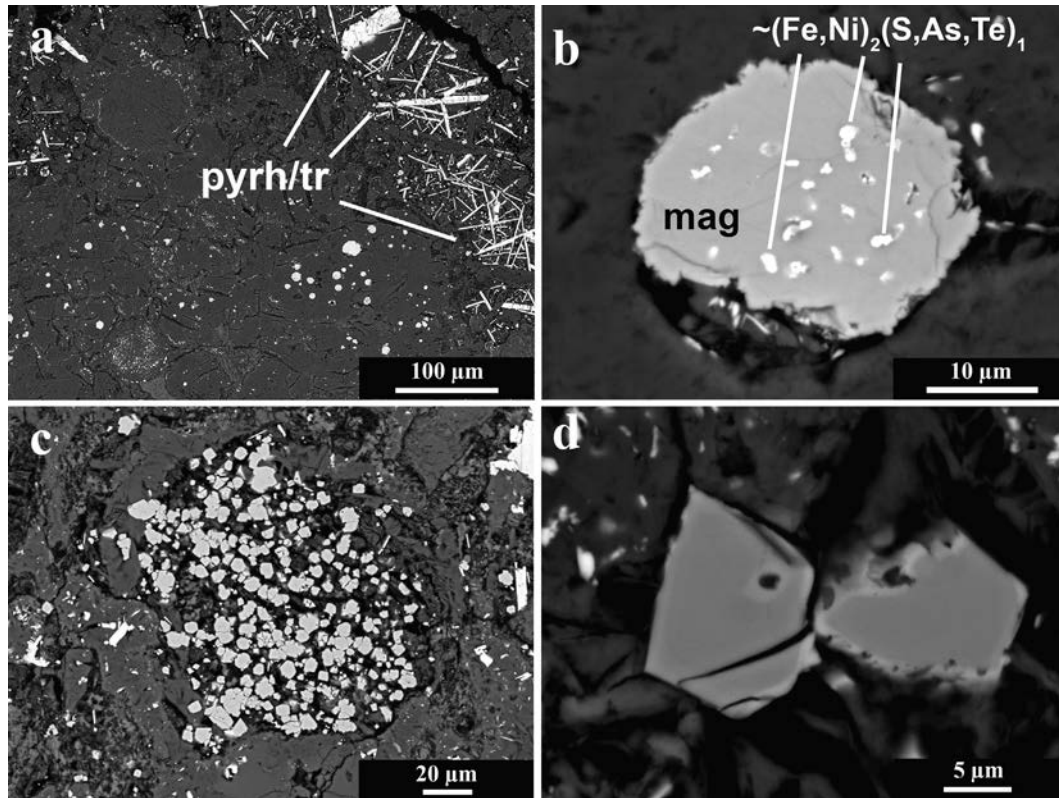
Fig. 10. (a) Part of a clast within the Flensburg meteorite showing a relict chondrule-like object with round magnetite-rich inclusions (lower right) embedded in phyllosilicates. The clast is surrounded by a zone of pyrrhotite/troilite laths (pyrh/tr). (b) Magnetite grains contain small inclusions of an Fe,Ni,As-rich phase that may be close to $(Fe,Ni)_2As$; (c) aggregate of small magnetite grains, texturally different to the typical magnetite framboids in CI chondrites; (d) chromite grains; BSE-images.
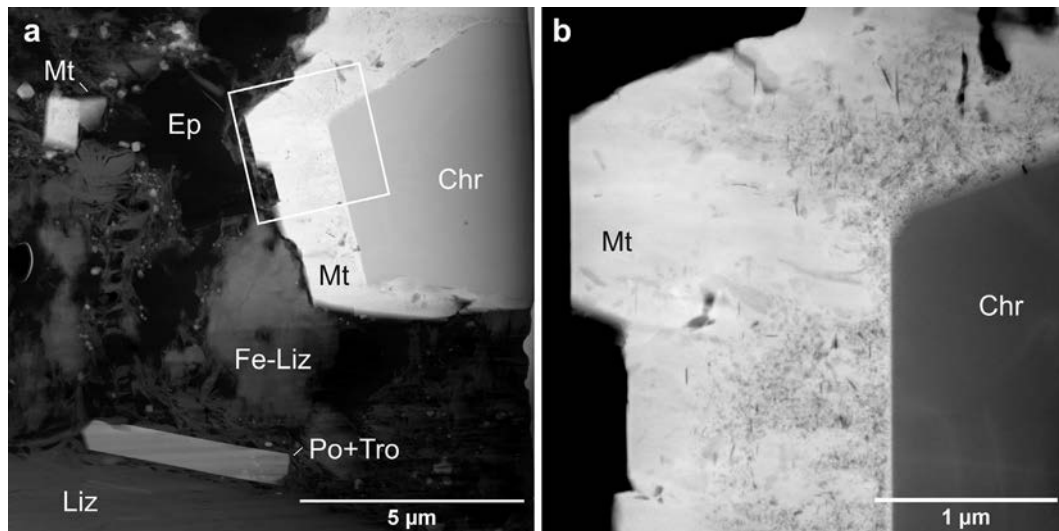
Fig. 11. Scanning TEM high-angle annular dark-field (STEM-HAADF) images of a composite magnetite-chromite grain in Flensburg. Chr: chromite, Ep: epoxy, Liz: lizardite, Mt: magnetite, Po: pyrrhotite, Tro: troilite. a) Overview image with sheath serpentine at the bottom, an attached low-Ni iron sulfide crystal, and adjacent Fe-rich matrix serpentine (Fe-Liz). Magnetite occurs as small octahedral crystals in the matrix and as an overgrowth on a chromite grain. b) Detail of (a) showing the internally heterogeneous structure of the magnetite rim. Nanoscale inclusions are likely a Fe-rich silicate, possibly with a spinel-like structure, as there are no obvious extra reflections in SAED patterns.

Fig. 12. Three O isotope diagrams of calcite and dolomite grains from Flensburg. (a) Overview of calcite and dolomite grains and the bulk values obtained for Flensburg. (b) Detailed view of calcite grains of different petrologic context. (c) Detailed view of dolomite grains of different petrologic context. (d) Overview of calcite and dolomite grains compared to literature data of calcites in CM chondrites. Literature data from Tyra et al. (2012, 2016), Horstmann et al. (2014b), Verdier-Paolett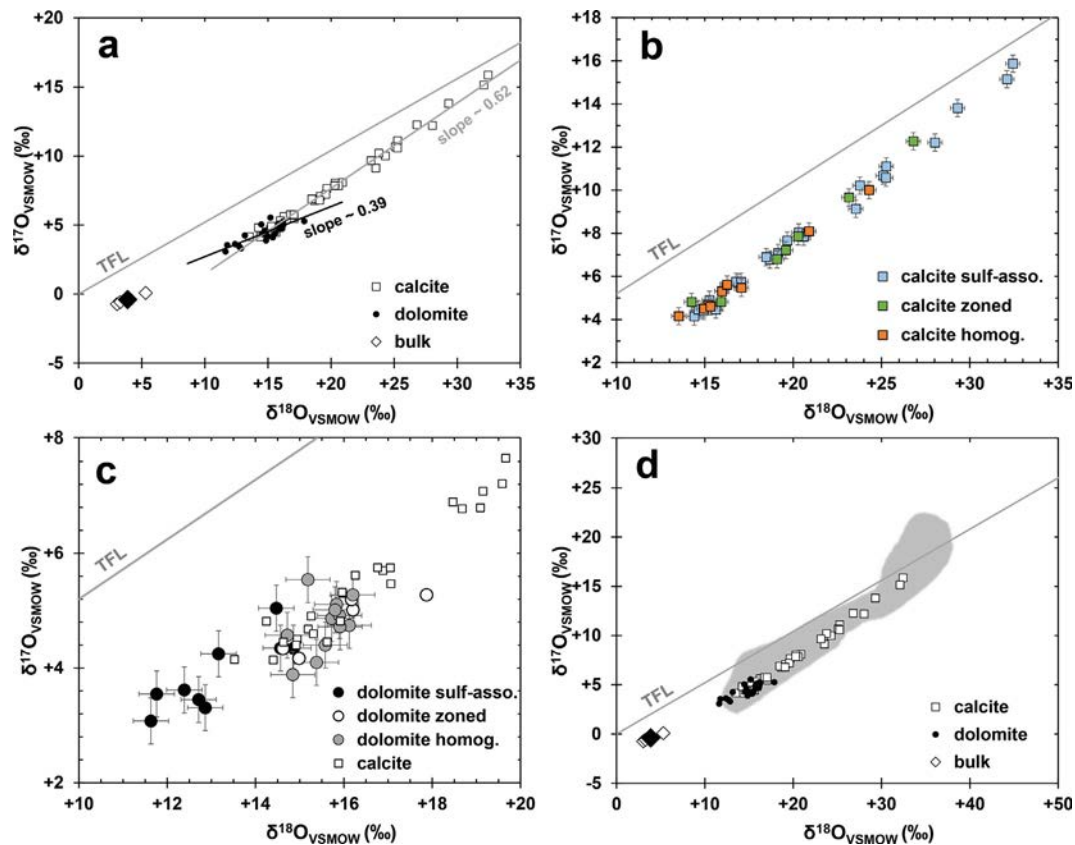i et al. (2017), and references therein (grey field). TFL = terrestrial fractionation line; sulf-asso. = sulfide-associated; homog. = homogeneous.

Flensburg chondrite display well-defined isochrons (Fig. 14; Table S5a,b), which yield initial $^{53}Mn/^{55}Mn$ ratios at the time of carbonate formation of $(4.43 \pm 0.80) \times 10^{-6}$ and $(4.50 \pm 1.08) \times 10^{-6}$, respectively. Note that uncertainties on the $^{53}Mn/^{55}Mn$ ratios include errors of relative ion yields (RIY) determined on HIGP calcite (Donohue et al., 2019, see SM), and dolomite (the same calibration, but corrected for dolomite-calcite matrix effect using data from Steele et al., 2017).

As the solar system initial $^{53}Mn/^{55}Mn$ is not well constrained, the initial $^{53}Mn/^{55}Mn$ ratios of the carbonates cannot be directly translated into ages relative to the beginning of the solar system (i.e., to the time of CAI formation), but they must first be converted to absolute ages. Relative to the angrite D'Orbigny with an initial $^{53}Mn/^{55}Mn = (3.54 \pm 0.18) \times 10^{-6}$ (McKibbin et al., 2015) and a (U isotope corrected) Pb-Pb age of 4563.37 ± 0.25 Ma (Brennecka and Wadhwa, 2012), the initial $^{53}Mn/^{55}Mn$ ratios of the Flensburg carbonates correspond to absolute ages of 4564.6 ± 1.0 Ma for calcites and 4564.6 ± 1.3 Ma for dolomites (2σ errors, including uncertainties on RIY, the absolute age of D'Orbigny, and the ^{53}Mn decay constant). Relative to an absolute Pb-Pb age of 4567.16 ± 0.30 Ma for CAIs (Connelly et al., 2012; Amelin et al.,

2010), the Mn-Cr ages of the carbonates correspond to relative ages of 2.6 ± 1.0 Ma and 2.5 ± 1.3 Ma after CAI formation, respectively. These ages would change to 3.4 ± 1.0 Ma and 3.3 ± 1.3 Ma if the Pb-Pb age of 4567.94 ± 0.31 Ma for CAIs reported by Bouvier et al. (2011) is used. Note that both Pb-Pb ages have been calculated using the measured U isotope composition of the CAIs, although the U isotope composition of Bouvier et al. (2011) has only been reported in an abstract. Further, the CAI used by Bouvier et al. (2011) was analysed also for ^{26}Al-^{26}Mg systematics, which yield an initial $^{26}Al/^{27}Al$ ratio of $(5.5 \pm 0.3) \times 10^{-6}$ (Wadhwa et al., 2013), which is consistent with canonical $^{26}Al/^{27}Al$ at the start of the solar system and indicates that the Al-Mg system in this particular CAI has not been disturbed by post-formation processes.

Prior studies have shown that carbonates from CM and CR chondrites have initial $^{53}Mn/^{55}Mn$ ratios of between $\sim 0.8 \times 10^{-6}$ and $\sim 3.7 \times 10^{-6}$ (Fujiya et al., 2012, 2013; Jilly-Rehak et al., 2017 – only studies using carbonate standards for RIY evaluation are considered, see SM), indicating that these carbonates formed ~ 1.0–9.2 Ma later than the carbonates in Flensburg. As such, the carbonates in Flensburg carbonates are the oldest yet identified in carbonaceous chondrites.

Table 3
$\delta^{18}O_{VSMOW}$, $\delta^{17}O_{VSMOW}$, and $\Delta^{17}O_{VSMOW}$ values for calcites and dolomites within the unique Flensburg carbonaceous chondrite. C. = code; N = homogenous grains; S = sulfide-associated grains; Z = zoned grains. Errors are ± 1 s.

Calcite	C.	$\delta^{17}O$ (‰)	$\delta^{18}O$ (‰)	$\Delta^{17}O$ (‰)	Dolomite	C.	$\delta^{17}O$ (‰)	$\delta^{18}O$ (‰)	$\Delta^{17}O$ (‰)
#004	N	+5.3 ± 0.3	+16.0 ± 0.1	−3.1 ± 0.3	#021	N	+4.9 ± 0.2	+15.7 ± 0.2	−3.4 ± 0.3
#121	N	+4.7 ± 0.5	+15.2 ± 0.3	−3.3 ± 0.6	#023	N	+3.9 ± 0.3	+14.8 ± 0.2	−3.9 ± 0.3
#137	N	+4.2 ± 0.3	+13.5 ± 0.2	−3.0 ± 0.3	#173	N	+4.1 ± 0.3	+15.4 ± 0.2	−4.0 ± 0.3
#166	N	+8.1 ± 0.4	+20.9 ± 0.5	−2.9 ± 0.5	#183	N	+4.4 ± 0.4	+15.6 ± 0.1	−3.8 ± 0.4
#198	N	+10.0 ± 0.4	+24.3 ± 0.5	−2.8 ± 0.5	#214	N	+5.1 ± 0.3	+15.8 ± 0.2	−3.2 ± 0.4
#206	N	+4.5 ± 0.3	+14.9 ± 0.3	−3.4 ± 0.3	#218	N	+4.7 ± 0.3	+16.1 ± 0.2	−3.7 ± 0.3
#277	N	+4.6 ± 0.3	+15.3 ± 0.3	−3.5 ± 0.3	#257	N	+4.9 ± 0.3	+15.9 ± 0.2	−3.5 ± 0.3
#328	N	+5.6 ± 0.3	+16.3 ± 0.3	−2.9 ± 0.3	#260	N	+4.6 ± 0.3	+14.7 ± 0.2	−3.2 ± 0.3
#350	N	+5.5 ± 0.3	+17.1 ± 0.2	−3.5 ± 0.3	#268	N	+5.5 ± 0.2	+15.2 ± 0.1	−2.4 ± 0.2
#002	S	+13.8 ± 0.3	+29.3 ± 0.3	−1.6 ± 0.3	#273	N	+4.7 ± 0.3	+15.9 ± 0.2	−3.6 ± 0.3
#016	S	+11.1 ± 0.5	+25.3 ± 0.4	−2.2 ± 0.5	#283	N	+5.0 ± 0.2	+15.8 ± 0.2	−3.3 ± 0.2
#025	S	+6.8 ± 0.4	+18.7 ± 0.3	−3.0 ± 0.4	#301	N	+5.3 ± 0.2	+16.2 ± 0.2	−3.2 ± 0.3
#038	S	+4.5 ± 0.3	+14.6 ± 0.2	−3.2 ± 0.4	#045	S	+3.6 ± 0.2	+12.4 ± 0.2	−2.9 ± 0.3
#061	S	+4.4 ± 0.2	+14.9 ± 0.2	−3.4 ± 0.2	#080	S	+4.3 ± 0.3	+14.9 ± 0.2	−3.5 ± 0.3
#062	S	+7.8 ± 0.4	+20.6 ± 0.6	−3.0 ± 0.5	#131	S	+3.5 ± 0.3	+11.8 ± 0.2	−2.6 ± 0.3
#078	S	+9.1 ± 0.3	+23.5 ± 0.5	−3.2 ± 0.4	#168	S	+3.5 ± 0.2	+12.7 ± 0.2	−3.2 ± 0.3
#082	S	+5.3 ± 0.3	+16.0 ± 0.3	−3.1 ± 0.4	#201	S	+3.1 ± 0.3	+11.6 ± 0.2	−3.0 ± 0.3
#099	S	+12.2 ± 0.4	+28.0 ± 0.3	−2.5 ± 0.4	#211	S	+3.3 ± 0.3	+12.9 ± 0.2	−3.5 ± 0.3
#120	S	+10.2 ± 0.3	+23.8 ± 0.3	−2.3 ± 0.3	#261	S	+5.0 ± 0.3	+14.5 ± 0.2	−2.6 ± 0.3
#153	S	+6.9 ± 0.4	+18.5 ± 0.4	−2.8 ± 0.4	#325	S	+4.3 ± 0.3	+14.6 ± 0.2	−3.3 ± 0.3
#161	S	+10.7 ± 0.4	+25.1 ± 0.4	−2.5 ± 0.5	#330	S	+4.2 ± 0.3	+13.2 ± 0.2	−2.7 ± 0.3
#167	S	+15.9 ± 0.3	+32.4 ± 0.3	−1.1 ± 0.3	#011	Z	+4.3 ± 0.3	+14.6 ± 0.2	−3.3 ± 0.3
#167a	S	+15.1 ± 0.3	+32.1 ± 0.3	−1.7 ± 0.3	#101	Z	+5.0 ± 0.3	+16.2 ± 0.2	−3.5 ± 0.3
#177	S	+4.5 ± 0.3	+15.6 ± 0.3	−3.8 ± 0.3	#175	Z	+4.2 ± 0.3	+15.0 ± 0.2	−3.7 ± 0.3
#181	S	+5.7 ± 0.3	+16.9 ± 0.3	−3.2 ± 0.4	#179	Z	+5.3 ± 0.3	+17.9 ± 0.2	−4.1 ± 0.3
#184	S	+4.1 ± 0.3	+14.4 ± 0.3	−3.4 ± 0.3	#250	Z	+5.2 ± 0.2	+16.2 ± 0.2	−3.3 ± 0.2
#208	S	+7.1 ± 0.3	+19.1 ± 0.4	−3.0 ± 0.4					
#215	S	+4.9 ± 0.3	+15.3 ± 0.3	−3.1 ± 0.4					
#234	S	+5.7 ± 0.3	+17.1 ± 0.2	−3.2 ± 0.3					
#272	S	+7.7 ± 0.3	+19.7 ± 0.5	−2.7 ± 0.4					
#306	S	+8.0 ± 0.4	+20.3 ± 0.4	−2.6 ± 0.4					
#312	S	+10.6 ± 0.3	+25.2 ± 0.3	−2.7 ± 0.3					
#323	S	+5.7 ± 0.3	+16.8 ± 0.2	−3.1 ± 0.3					
#010	Z	+4.8 ± 0.3	+15.9 ± 0.3	−3.6 ± 0.3					
#020	Z	+4.8 ± 0.3	+14.2 ± 0.3	−2.7 ± 0.4					
#107	Z	+12.3 ± 0.3	+26.8 ± 0.3	−1.8 ± 0.4					
#180	Z	+7.2 ± 0.3	+19.6 ± 0.2	−3.1 ± 0.3					
#205	Z	+7.9 ± 0.4	+20.3 ± 0.4	−2.8 ± 0.5					
#231	Z	+6.8 ± 0.4	+19.1 ± 0.4	−3.2 ± 0.5					
#264	Z	+9.7 ± 0.4	+23.2 ± 0.3	−2.5 ± 0.5					

4. CHEMISTRY AND ISOTOPIC COMPOSITIONS

4.1. Bulk composition

The chemical bulk composition determined by ICP-AES and ICP-SFMS is given in Table 4. The composition of Flensburg is very similar to the median composition of 14 CM chondrites analyzed by Braukmüller et al. (2018), except for somewhat lower concentrations of Zn, Cu, and Pb (about 30%) in Flensburg. These data will be discussed below.

4.2. Bulk H, C, and N abundances and isotopic compositions

The bulk H, C and N elemental abundances and isotopic compositions of the Flensburg meteorite are given in Table 5. The H abundances were determined by two different techniques and agree very well. They clearly show that

Flensburg is a carbonaceous chondrite of the petrologic types 1–2. A H concentration of 1.10 ± 0.03 wt.% was obtained at the Earth and Planets Laboratory (CIW), whereas in Bochum the water-content of the meteorite was determined as being 10.15, 9.56 and 9.92 wt.% for three dried samples (mean: 9.88 ± 0.5 wt.%) revealing a very similar H concentration (Table 5).

The C contents were also determined by two different techniques on approximately the same amounts of material taken from the large powdered sample of Flensburg. Unlike for H, there is significant disagreement in the two measured C contents for reasons that are unclear.

As illustrated in Figs. 15–17, compared to other type 1 and 2 chondrites (Robert and Epstein, 1982; Kerridge, 1985; Eiler and Kitchen, 2004; Alexander et al., 2012, 2013) Flensburg is unique. It has the lightest bulk H isotopic composition of any measured type 1 or 2 chondrite (Fig. 15). Its bulk H content is similar to a fairly typical
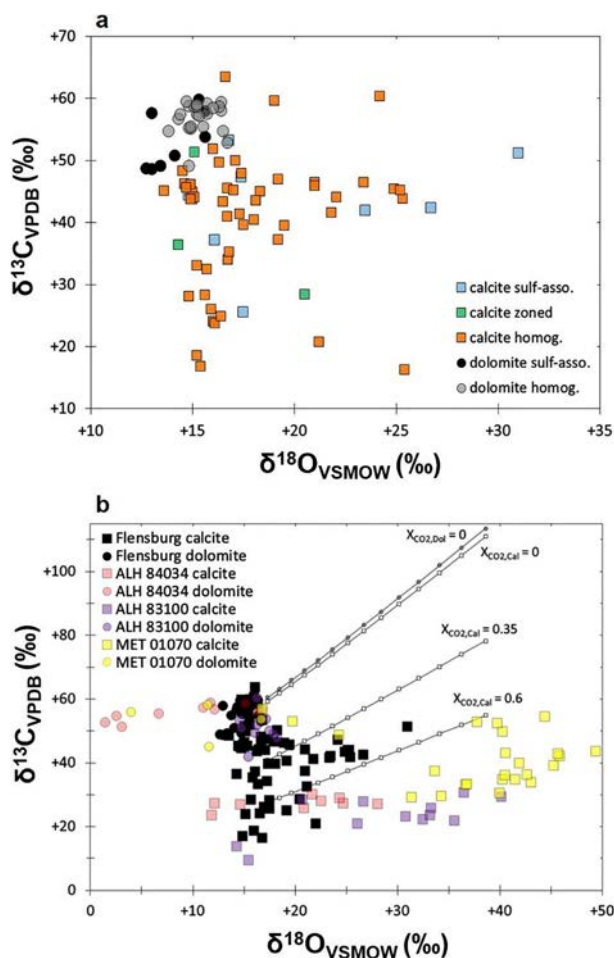
Fig. 13. (a) Simultaneous single-spot carbon and oxygen isotope analyses of Flensburg dolomites and calcites. (b) Comparison with CM carbonate data by Telus et al. (2019). Scatter of dolomite data is lower than for calcites, which may have formed from gas with varying CO/CO_2 ratios resulting in significant $\delta^{13}C$ variation as indicated by model curves calculated according to Alexander et al. (2015). Most dolomites and Flensburg calcites formed at rather high temperatures (i.e., low $\delta^{18}O$ values), when compared to the majority of CM calcite data.

unheated CM chondrite, and significantly less than in type 1 CI, CM or CR chondrites. Its bulk C content, on the other hand, is lower than most unheated CMs, as well as all CIs and Tagish Lake, but higher than all CRs except the anomalous Al Rais. Its $\delta^{13}C$ value is higher than that for almost all CMs, CRs, and CIs (Fig. 16). Only the Tagish Lake lithologies have higher bulk $\delta^{13}C$ values. There is a crude correlation between bulk N content and bulk $\delta^{15}N$ (Fig. 17) amongst type 1 and 2 chondrites, except for the very ^{15}N-rich CRs and the anomalous CM Bells. Flensburg has the lowest bulk N content and $\delta^{15}N$ value of any measured type 1 and 2 chondrites (Fig. 17).

4.3. Bulk O isotope compositions

The O isotope compositions of the three analyzed chips are listed in Table 6. The data for Flensburg plot within the field of CM chondrites, but at the ^{16}O-rich end and marginally overlap with data from CV and CR chondrites (Fig. 18). The possible relationships between Flensburg and other carbonaceous chondrite groups will be considered in the discussion.

4.4. Noble gas components

The results of the noble gas measurements for the two samples are summarized in Tables 7a–7d. All noble gases consist almost entirely of trapped (tr) components with a very small cosmogenic (cos) contribution, which renders decomposition and determination of the latter difficult. The composition of the pure Ne_{tr} endmember was determined by extrapolating a line from a mean Ne_{cos} through the measured data points and finding the intercept with the Ne-E-Ne-Q mixing line (Fig. 19).

As the gas mixture is dominated by trapped components, the cosmogenic $^{22}Ne/^{21}Ne$ cannot be determined. Therefore, a mean cosmogenic $^{21}Ne/^{22}Ne$ of 1.11 was assumed, following Scherer and Schultz (2000). This ratio commonly serves as a shielding indicator, and is e.g., used in the depth- and chemistry-dependent model of Leya and Masarik "LM" (2009) applied here to determine production rates. The chemistry was taken from Table 4 (ICP-SFMS, where ICP-AES data are not available assuming an average 42.5 wt.% O, see section "bulk composition").

ReVelle (1979) estimated mass loss due to atmospheric ablation for ordinary chondrites. The authors concluded that a minimum of 35% of the mass is lost during flight through the atmosphere, and modelled for a velocity of 18 km/s a mass loss between 85 and 95%. These estimates are probably still conservative considering that Flensburg is more fragile and more volatile than the ordinary chondrites used in the model. Alexeev (2003) estimated a mean ablation percentage of $91.5^{+2.1}_{-2.6}\%$ for ordinary chondrites.

A most probable range of production rates was calculated assuming 85% of the mass has been lost in ablation. Additionally, production rates were restricted by excluding 22% of the inner radius for each allowed size. The volume of this part of a sphere only makes up <1% of the total volume. Very large radii above 200 cm were not included, as Flensburg's size and density makes such a pre-atmospheric size highly unlikely. A range of possible production rates is given in Table S6. All measured isotope ratios for He, Ne, and Ar are consistent with essentially no exposure to cosmic rays (e.g. Fig. 19). Maximum possible cosmogenic ^3He, ^{21}Ne, and ^{38}Ar were determined and maximum CRE ages calculated accordingly and are given in Table S7. Large variations in the determined CRE ages are due to the unknown $^{22}Ne/^{21}Ne$ ratio.

The density used in the LM model is 2.25 g/cm^3, whereas Flensburg's density is lower (1.984 ± 0.016 g/cm^3), leading to an increase of all calculated possible pre-atmospheric sizes by 13.4%. Fig. S7 shows the Xe isotopic composition of Flensburg and that air contamination due to weathering or oxidation is negligible as might be
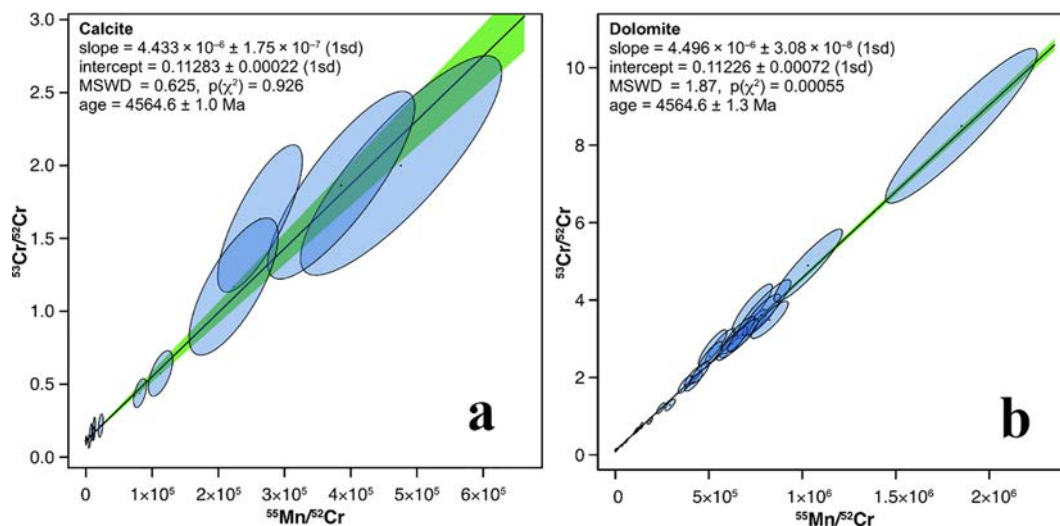
Fig. 14. (a) ^{53}Cr-^{53}Mn-age of calcites from the unique C1 chondrite Flensburg. Calcites formed very early in the planetesimal from which Flensburg originated. (b) ^{53}Mn-^{53}Cr age of dolomites. As confirmed by mineralogical observations, particularly calcite overgrowth of dolomite, most dolomites formed before calcite. The remarkably nearly perfect alignment of dolomite data along the isochron (corresponding to a 0.7% error of the slope) indicates dolomite formation in a narrow time interval of about 70 000 years.

Table 4
The bulk chemical composition of Flensburg compared with CM data. Oxides in wt.%, all other elements in ppm (µg/g).

wt.%	ICP-AES	ICP-SFMS	CM[*]	ppm	ICP-SFMS	CM[*]
SiO$_2$/S[**]						
TiO$_2$	0.09	0.099	0.093	Zr	4.91	4.73
Al$_2$O$_3$	2.20		2.25	Nb	0.375	0.368
FeO	27.4		28.3	Cs	0.119	0.119
MnO	0.22	0.202	0.229	Ba	3.24	2.98
MgO	19.7		20.1	La	0.343	0.290
CaO	1.82	1.78	1.76	Ce	0.876	0.758
Na$_2$O	0.64		0.356	Pr	0.131	0.122
K$_2$O	0.05	0.050	0.046	Nd	0.661	0.624
P$_2$O$_5$	0.23	0.245	0.226	Sm	0.215	0.204
ppm				Eu	0.0813	0.0773
Cr	3036		3176	Gd	0.296	0.321
Li				Tb	0.055	0.0515
Be		0.0287		Dy	0.296	0.351
K		413	382	Ho	0.082	
Sc		8.37		Er	0.240	0.221
V		65.4	67.3	Tm	0.0375	0.0346
Mn		1568	1775	Yb	0.235	0.229
Co		536	597	Lu	0.0352	0.0346
Ni	13,000		13,236	Hf	0.152	0.139
Cu		102	140	Ta	0.0194	
Zn		154	197	W	0.130	0.125
Ga		7.15	6.86	Pb	1.166	1.50
Rb		1.70	1.60	Th	0.0433	0.0369
Sr		10.33		U	0.0099	0.0087
Y		2.26				

[*] Median CM data (n = 14) of Braukmüller et al. (2018).
[**] SiO$_2$ and S concentrations of ~28 and ~2.3 wt.%, respectively, were calculated from microprobe analysis (controlled and correlated by the ICP-AES data for Mg, Al, and Ca; see SM).

expected given the short period of one day between fall and find. The Xe isotopic composition is similar to Q with possibly a small HL contribution (~2%). Corrections for a cosmogenic contribution to the heavy noble gases are therefore not necessary.

4.5. Radionuclide activities

Gamma-lines were detected from primordial radionuclides, members of the natural decay series of ^{238}U and ^{232}Th, as well as of ^{40}K (Table 8), and short-lived

Table 5
The bulk H, C, and N elemental abundances and isotopic compositions. The uncertainties are 1σ.

H (wt.%)[1]	1.10 ± 0.03	δD (‰)	−311 ± 4
H (wt.%)[2]	1.10 ± 0.03		
C (wt.%)[1]	1.54 ± 0.01	δ13C (‰)	+3.5 ± 0.9
C (wt.%)[2]	1.14 ± 0.2		
N (wt.%)[1]	0.027 ± 0.001	δ15N (‰)	−25 ± 2

[1] Analysed at the Earth and Planets Laboratory (CIW).
[2] Analysed at the University of Bochum. The uncertainties are based on the measurements of standards and results for 2–3 sample aliquots.
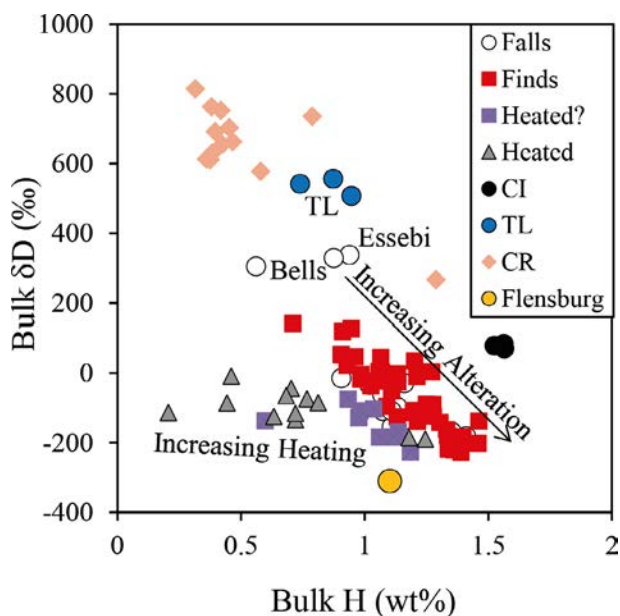

Fig. 15. The bulk H elemental abundances and isotopic compositions of type 1–2 carbonaceous chondrites (Alexander et al., 2012, 2013), including Flensburg. In general, for unheated members of a chondrite group, the H contents increase and the δD values decrease with increasing degree of alteration. This is due to the mixing of H in two components, a D-rich organic matter and D-poor H_2O/OH. Where a meteorite plots in this figure depends on its water/organic ratio and the initial H isotopic compositions of these two components. Almost all type 1–2s seem to have accreted water and organic matter with similar compositions (roughly −450‰ and 3000–3500‰, respectively). The principle exceptions are the CRs whose water was significantly more D-rich (∼100‰). Heating of altered meteorites, mostly through shock, drives them to lower H contents. Flensburg occupies a unique position in this diagram, being isotopically lighter than any other measured type 1–2 chondrite. It cannot be ruled out from this figure that Flensburg has been heated and partially dehydrated, but from other evidence this seems unlikely. TL = Tagish Lake.
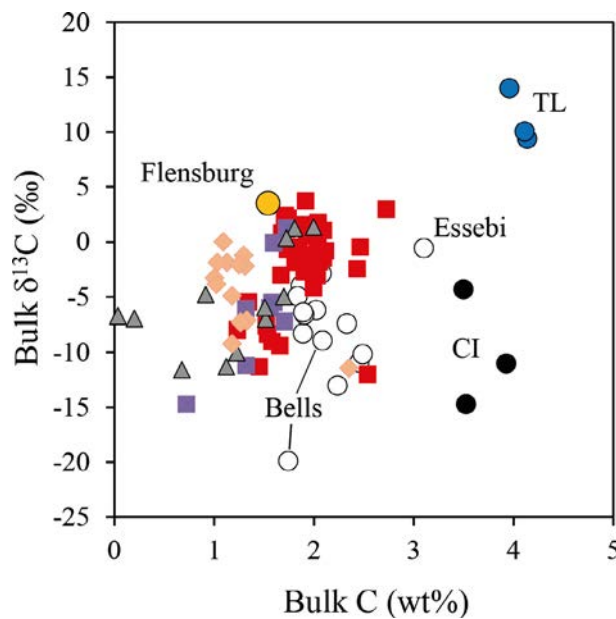

Fig. 16. The bulk C elemental abundances and isotopic compositions of type 1–2 carbonaceous chondrites (Alexander et al., 2012, 2013), including Flensburg. The symbols are as in Fig. 15. Where unheated meteorites plot in this figure depends on their relative abundances of isotopically light organic material (typically −34‰ to −14‰) and isotopically heavy carbonate (typically 23–80‰). Heating will destroy both organic matter and carbonates, though probably not always in the same proportions. Flensburg has a bulk C content that is intermediate between most CMs and CRs, but a high δ13C value that is consistent with the fact that Flensburg is carbonate-rich. TL = Tagish Lake.

cosmogenic nuclides. All given specific activities in units of disintegration per minute (dpm) per kg are corrected to 12th September 2019 including decay-correction during the measurement time itself.

The radionuclide data do not allow any statement about possible disequilibria in the decay series. However, assuming an equilibrium state of the decay series, the terrestrial isotope ratios and a homogenous distribution in the sample, the U, Th, and K concentrations of the sample would be (18 ± 3) ng g^{−1}, (68 ± 9) ng g^{−1}, and (420 ± 40) μg g^{−1}, respectively. A comparison of the gamma-spectrometric values to those from ICP-SFMS for Flensburg presented in Table 4 show clearly higher values for U and Th.

For the only long-lived cosmogenic radionuclide usually detectable by gamma-spectrometry, 26Al, only an upper limit of 1.7 dpm kg^{−1} could be given, providing evidence for a short or complex exposure history of the meteoroid.

The relevant AMS data for Flensburg and corresponding processing blanks, and specific activities for 10Be, 26Al, and 41Ca for Flensburg have been calculated from AMS ratios, ICP-MS results of the liquid aliquot (27Al and natCa) or carrier addition (9Be), sample weight and half-lives. The concentrations of the three lighter radionuclides are extremely low (10Be: 0.0539 ± 0.0016 dpm kg^{−1}, 26Al: 0.209 ± 0.030 dpm kg^{−1}, 41Ca: 0.37 $^{+0.32}_{-0.26}$ dpm kg^{−1}). These values are one to more than two orders of magnitude lower than saturation activities under typical irradiation geometries. The 26Al specific activity, determined from the AMS data, is about a factor of ten lower than the detection limit of gamma-spectrometry. These results suggest a very short exposure age. The concentration of 14C is 31.3 ± 1.3 dpm kg^{−1}, which can be e.g. compared to the expected saturation of ∼60 dpm kg^{−1} for a CI meteorite (Jull et al., 1998) for a meteoroid of a radius of ∼30 cm. The measured 60Fe/Fe ratio of Flensburg is not distinguishable from that
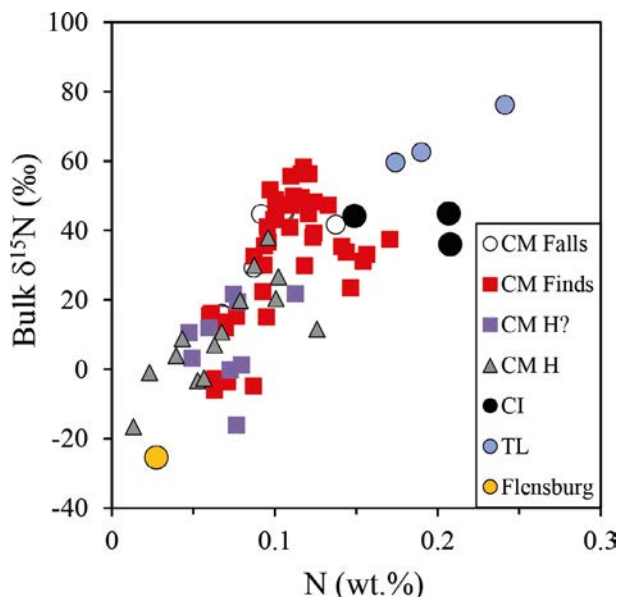
Fig. 17. The bulk N elemental abundances and isotopic compositions of type 1–2 carbonaceous chondrites (Alexander et al., 2012, 2013), including Flensburg (Table 5). The anomalous CM, Bells, and the CRs are not shown because their bulk isotopic compositions are >100‰. There is a rough correlation between N abundance and isotopic composition, but the cause of this is unknown. Flensburg occupies a unique position in this figure having both the lightest N isotopic composition and the lowest N content of any unheated type 1–2 chondrite (compare Fig. S6). TL = Tagish Lake; CM H = heated CM chondrite; CM H? = possibly heated CM chondrite.

Table 6
Results of O isotope analyses of three different chips of the Flensburg meteorite. The $\delta^{17,18}O$ values are reported relative to VSMOW, and the $\Delta^{17}O$ is reported relative to a mass dependent isotope fractionation reference line with a slope of 0.528 (equation 1; SM).

Analysis ID	Mass (mg)	$\delta^{17}O$ (‰)	$\delta^{18}O$ (‰)	$\Delta^{17}O$ (‰)
6871	1.943	−0.730	3.03	−2.33
6870	2.036	−0.578	3.30	−2.32
6718	2.181	0.081	5.30	−2.72

of the processing blank ($(4–6) \times 10^{-17}$). The value is about three orders of magnitude lower than that expected for saturation values for stony meteorites (e.g. Knie et al., 1999) and by far the lowest $^{60}Fe/Fe$ ratio ever measured in any meteorite so far.

4.6. Titanium, Cr, and Te isotope compositions

The Cr and Ti isotope compositions of Flensburg were obtained in Zürich and Münster and the data are very similar (Table 9). The Cr isotope data show the best overlap with CM chondrites. The Ti isotope data from Zürich fall close to the field of CV/CO chondrites, whereas the Münster data overlaps with CM chondrites (Table 9, Fig. 20; Figs. S8 and S9). The combined ^{54}Cr and ^{50}Ti isotope data
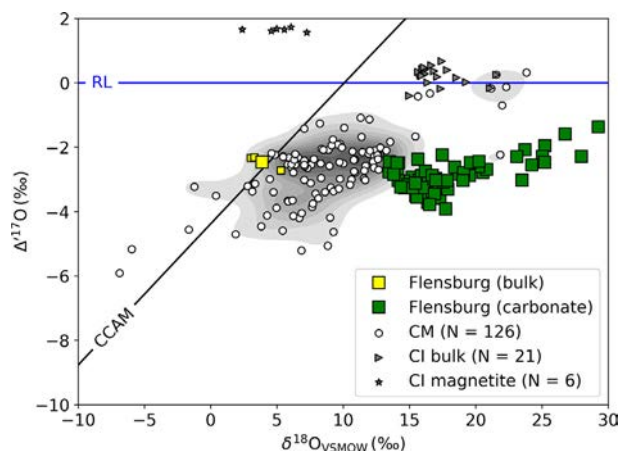

Fig. 18. Plot of the O isotope composition of Flensburg in comparison to published compositions of CM and CI chondrites and components. The $\Delta^{17}O$ data have been calculated using Equation 1 (Supplement). The chondrite data were obtained from the Meteoritical Bulletin database (https://www.lpi.usra.edu/meteor/, access February 2020; Clayton et al., 1976; Clayton and Mayeda, 1984; Mayeda et al., 1987; Rowe et al., 1994; Clayton and Mayeda, 1999). The carbonaceous chondrite anhydrous minerals mixing line (CCAM, $\delta^{17}O_{VSMOW} = 0.9467 \delta^{18}O_{VSMOW} –4.3674‰$) is taken from Clayton (2008). Terrestrial samples plot on the mass fractionation line termed "RL" (reference line).

place Flensburg between the CM and CV chondrites, with the closest link to CM chondrites (Fig. 20).

It has recently been shown that carbonaceous chondrites (except CR chondrites) exhibit correlated variations of mass-dependent Te isotope composition and Te concentration, indicating that increasingly volatile- and, hence, Te-depleted samples are increasingly isotopically light (Hellmann et al., 2020). This correlation reflects varying amounts of CI-like matrix in the different groups of carbonaceous chondrites and, as such, can be used as an additional tool to assess genetic relationships among and between different carbonaceous chondrites. The Te isotopic data obtained in this study reveals that Flensburg has one of the heaviest Te isotopic composition observed among carbonaceous chondrites ($\delta^{128/126}Te = 0.12 \pm 0.02$), overlapping only with CI chondrites and Tagish Lake. Compared to CM chondrites, Flensburg has a slightly higher $\delta^{128/126}Te$ value, yet its Te concentration of 1399 ± 51 ng/g is very similar to that of CM chondrites (Fig. 21). The Te isotopic data, therefore, link Flensburg to CM-like and other volatile-rich carbonaceous chondrites.

5. ORGANICS

The volatile elements C, H, O, N, and S were the most abundant elements in the early Solar nebula, and many accreted as ices or organic compounds on planetesimals (Calvin, 1999), with a continuum ranging from small defined molecules (e.g. H_2O, CO_2, SO_2, NH_3, CH_4, CO, N_2, in decreasing order of freezing temperature) to larger $C_nH_mO_pN_qS_r$ molecules of considerable mass range and chemical diversity (Schmitt-Kopplin et al., 2010). The

Table 7a
He and Ne isotope concentrations (in 10^{-8} cm^3 STP/g) and isotopic ratios in the two samples.

	^{3}He$_{(cos)}$	^{4}He	^{3}He/^{4}He × 10,000	^{20}Ne	^{20}Ne/^{22}Ne	^{21}Ne/^{22}Ne	^{21}Ne$_{cos}$
S	0.365 ± 0.011	3052 ± 45	1.195 ± 0.040	8.45 ± 0.26	8.86 ± 0.19	0.0348 ± 0.0013	0.0332 ± 0.0014
L	0.2873 ± 0.0025	2442 ± 21	1.177 ± 0.014	7.71 ± 0.10	8.866 ± 0.081	0.03233 ± 0.00062	0.02813 ± 0.00059

Table 7b
Ar isotope concentrations (in 10^{-8} cm^3 STP/g) and isotopic ratios in the two samples.

	^{36}Ar	^{36}Ar/^{38}Ar	^{40}Ar/^{36}Ar	^{36}Ar$_{tr}$	^{38}Ar$_{cos}$
S	47.64 ± 0.94	5.34 ± 0.11	19.1 ± 5.0	48.37 ± 0.95	0.01 ± 0.01
L	41.851 ± 0.034	5.339 ± 0.019	41.6 ± 2.6	41.846 ± 0.0034	0.007 ± 0.001

Table 7c
Kr isotope concentrations (in 10^{-10} cm^3 STP/g) and isotopic ratios in the two samples (×100).

	^{84}Kr	^{78}Kr/^{84}Kr	^{80}Kr/^{84}Kr	^{82}Kr/^{84}Kr	^{83}Kr/^{84}Kr	^{86}Kr/^{84}Kr
S	53.2 ± 3.7	0.597 ± 0.058	3.83 ± 0.39	20.0 ± 2.0	20.0 ± 1.9	31.1 ± 3.1
L	50.0 ± 1.1	0.611 ± 0.017	3.90 ± 0.11	20.10 ± 0.55	20.14 ± 0.53	30.86 ± 0.84

Table 7d
Xe isotope concentrations (in 10^{-10} cm^3 STP/g) and isotopic ratios in the two samples (×100).

	^{132}Xe	^{124}Xe/^{132}Xe	^{126}Xe/^{132}Xe	^{128}Xe/^{132}Xe	^{129}Xe/^{132}Xe	^{131}Xe/^{132}Xe	^{134}Xe/^{132}Xe	^{136}Xe/^{132}Xe
S	59.8 ± 1.3	0.4754 ± 0.0100	0.4275 ± 0.0091	8.29 ± 0.12	108.5 ± 1.6	81.9 ± 1.3	38.56 ± 0.62	32.37 ± 0.51
L	48.53 ± 0.75	0.4785 ± 0.0057	0.4102 ± 0.0051	8.122 ± 0.056	107.62 ± 0.78	80.97 ± 0.58	37.82 ± 0.25	31.97 ± 0.20

Table 8
Specific activities of radionuclides determined by gamma-spectrometry. All activity data are referenced to the date of fall, 12th September 2019. Half-lives are from the Decay Data Evaluation Project (DDEP, 2020) or for ^{26}Al from Norris et al. (1983); d = days; a = years.

Radionuclide	Half-life	Specific activity (dpm kg^{-1})	σ (%)
Cosmogenic			
^{7}Be	53.22 d	121	14
^{22}Na	2.6029 a	65	8.8
^{26}Al	7.05 10^5 a	<1.7	
^{46}Sc	83.787 d	12.6	13
^{48}V	15.9735 d	26	17
^{51}Cr	27.704 d	116	21
^{54}Mn	312.19 d	150	8
^{56}Co	77.236 d	7.3	19
^{57}Co	271.81 d	13.5	13
^{58}Co	70.85 d	16.4	13
^{60}Co	5.2711 a	98	8.1
Primordial & decay series			
^{238}U decay series			
^{238}U	4.468 10^9 a	<22	
^{226}Ra	1600 a	13.3	18
^{210}Pb	22.23 a	<27	
^{232}Th decay series			
^{228}Ra	5.75 a	<24	
^{228}Th	1.9126 a	16.6	13
^{40}K	1.2504 10^9 a	780	8.4

Fourier Transform mass spectra (FTMS) obtained from the Flensburg methanolic extract showed ~1400 assigned molecular compositions, substantially fewer than those obtained for the CM2.5-CM6 chondrite breccia Murchison (n = 9850), CM1 Meteorite Hills (MET)01070 or CI Orgueil, as well as selected metamorphosed ordinary chondrites (Fig. 22). No CHOMg-species were observed in the Flensburg soluble organic matter (SOM), in contrast to the ~60 samples previously analyzed by FT mass spectrometry (Ruf et al., 2017).

Table 9
Titanium and Cr isotope compositions of the Flensburg meteorite.

Sample	$\varepsilon^{46}Ti$	2 SE	$\varepsilon^{48}Ti$	2 SE	$\varepsilon^{50}Ti$	2 SE	n*	$\varepsilon^{53}Cr$	2 SE	$\varepsilon^{54}Cr$	2 SE	n*
Flensburg (Zürich)	+0.53	0.05	−0.02	0.02	+3.31	0.08	11	+0.20	0.04	+0.95	0.05	17
Flensburg (Münster)	+0.54	0.11	±0.00	0.08	+2.98	0.10	13	+0.19	0.05	+1.06	0.11	6

* n: Number of measurements; SE = Standard Error.

Table 10
The ^1H NMR section integrals for key substructures of Flensburg and Murchison methanolic extracts of soluble organic matter (SOM) (asterisk *: sizable proportions of formic acid, HCOOH). Murchison data were extracted from Fig. 2 in Hertkorn et al. (2015); this reference includes detailed interpretations on aliphatic branching patterns in Murchison SOM, which are grossly similar for Flensburg SOM as well.

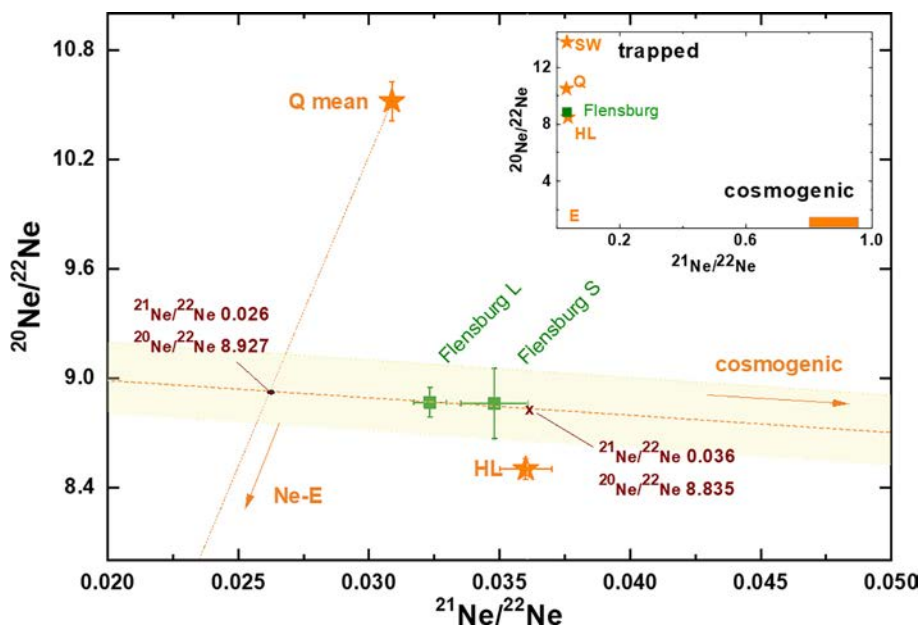| δ (^1H) [ppm]	key substructures	Flensburg %	Murchison %
10 … 5.2	$C_{ar}\underline{H}$, =C$\underline{H}$, $O_2C\underline{H}$	3	5.0*
4.7 … 3.1	OC$\underline{H}$	7	7.6
3.1 … 2.0	$C_{ar}C\underline{H}$, OCC$\underline{H}$	19	14.7
2.0 … 1.85	$\underline{H_3}$CCOH	12	5.3
1.85 … 1.35	OCCC$\underline{H}$, alicyclic CCC$\underline{H}$	15	19.8
1.35 … 1.25	$C_2C\underline{H_2}$, complex branching	17	20.8
1.25 … 0.30	$OC_nC\underline{H_3}$; n ≥ 3	25	26.4
∼0	Si(O$\underline{H}$)$_4$ derivatives	2	minuscule

Fig. 19. Three-isotope plot showing the Ne isotopic composition of Flensburg, plotting very close to trapped Ne compositions found in carbonaceous chondrites (see inset for typical cosmogenic endmember composition ($^{20}Ne/^{22}Ne)_{cos} = 0.83 \pm 0.11$ and ($^{21}Ne/^{22}Ne)_{cos} = 0.87 \pm 0.08$ (Wieler, 2002). The isotopes plot within a triangle of the trapped Ne components Q (Busemann et al., 2000), Ne-E (Amari et al., 1995) and HL (Huss and Lewis, 1994) and can thus be explained entirely without a cosmogenic contribution. The position of the data point that allows us to determine a maximum contribution of cosmogenic ^{21}Ne is marked by "x". The composition of the pure trapped endmember in Flensburg (($^{20}Ne/^{22}Ne)_{tr} = 8.93 \pm 0.29$ and ($^{21}Ne/^{22}Ne)_{tr} = 0.03 \pm 0.01$) is determined by the crossing of the extrapolated line from Ne$_{cos}$ through the measured data points and the Ne-E-Ne-Q mixing line.

The ^1H NMR spectra (Fig. S10) demonstrated that both Murchison and Flensburg SOM shared analogous fundamental aliphatic branching units. However, Flensburg SOM showed higher proportions of hump-like background NMR resonances from δ_H ∼0.7–2.7 ppm that in part represent remote O functionalization (OCC$\underline{H}$-units; $\delta_H > 2$ ppm) and alicyclic rings (Table 10). Acetic acid represents ∼12% of the total ^1H NMR integral, and in combination, directly (OC$\underline{H}$ units; δ_H ∼3.1–4.7 ppm) and remotely (OCC$\underline{H}$ units; δ_H ∼2.0–3.1 ppm) oxygenated aliphatic compounds were
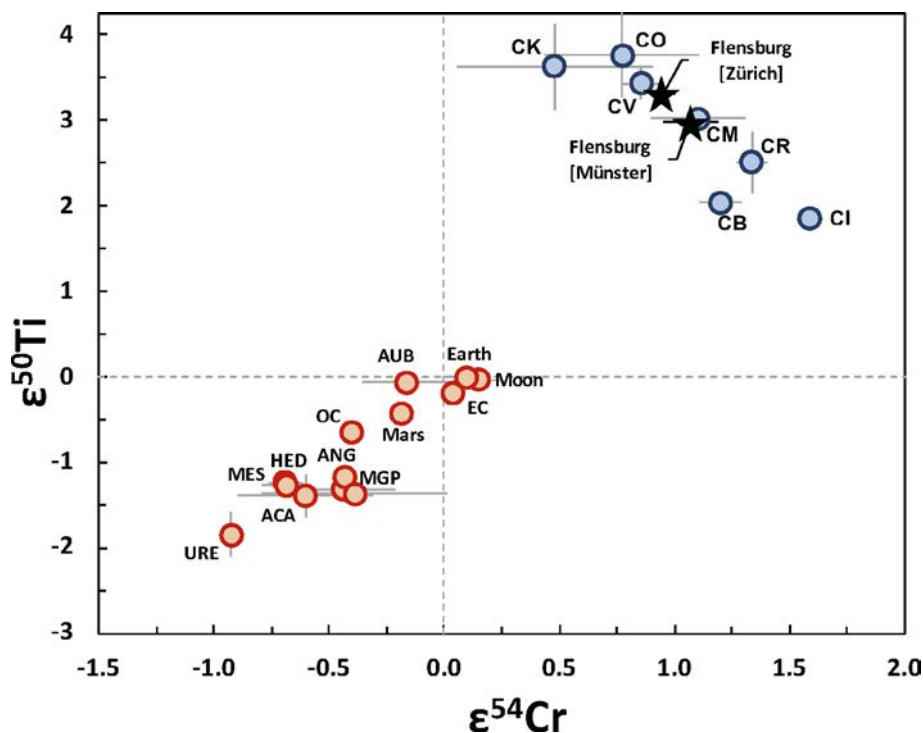
Fig. 20. Titanium versus Cr isotope compositions obtained in this study compared to literature data of various meteorite groups. Epsilon values are given relative to Earth. Uncertainties are 2 SE for data of this study (or 95% CI) and 2 SD for averages of meteorite groups in order to illustrate the scatter of the data in each meteorite group. EC: enstatite chondrites, OC: ordinary chondrites, AUB: aubrites, ANG: angrites, ACA: acapulcoites, BRA: brachinites, HED: howardite-eucrite-diogenite group, MGP: main group pallasites, MES: mesosiderites, URE: ureilites. Literature data: e.g., Niederer et al., 1981; Shukolyukov and Lugmair, 2006; Trinquier et al., 2007, 2008a, 2008b, 2009; Qin et al., 2010; Yamashita et al., 2010; Yamakawa et al., 2010; Göpel and Birck, 2010; Zhang et al., 2011, 2012; Petitat et al., 2011; Larsen et al., 2011; Schiller et al., 2014; Sanborn et al., 2015; Williams, 2015; Göpel et al., 2015; Burkhardt et al., 2017, 2019; Bischoff et al., 2017a; Goodrich et al., 2017; Gerber et al., 2017; Mougel et al., 2018; Sanborn et al., 2019; Zhu et al., 2019.
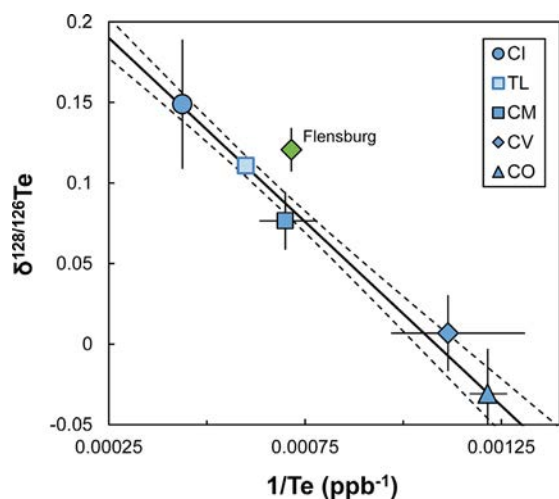

Fig. 21. Te isotope characteristics of Flensburg. The $\delta^{128/126}$Te–1/Te mixing line is defined by carbonaceous chondrite groups. TL: Tagish Lake. Data from Hellmann et al. (2020). Uncertainties on $\delta^{128/126}$Te and [Te] represent two standard deviation (2 s.d.).

more abundant in Flensburg SOM than in Murchison SOM (Fig. S10).

6. PHYSICAL CHARACTERISTICS

6.1. IR-spectroscopy

The infrared (IR) reflectance spectra between 8 μm and 18 μm (spectral resolution of 4 cm^{-1}) of a thin section of the Flensburg meteorite were compared to those from selected CI, CM, CV and CH chondrites (Fig. 23a). Details about the analyzed samples are given in Table S8.

The Christiansen feature (CF) is visible as a characteristic minimum in reflection spectra (maximum emission spectra). Its wavelength can be related to several different sample properties, e.g. the chemical composition of the sample (e.g., Pieters and Englert (1993), and references therein). The CF of the Flensburg sample measured with an angle of incidence (i) of 25° and angle of emergence (e) of 15° is at 8.98 μm. Measured at i20;e15, the CF shifts slightly to 9.07 μm. Both values are comparable to the wavelength of the CF of the two CI1 samples Alais (CF = 8.83 μm) and Orgueil (CF = 8.90 μm). For comparison, in the Murchison thin section the CF is at 8.80 μm and in that of Cold Bokkeveld at 8.85 μm. The samples of Allende (CV) and Acfer 182 (CH) show CFs at shorter wavelengths.
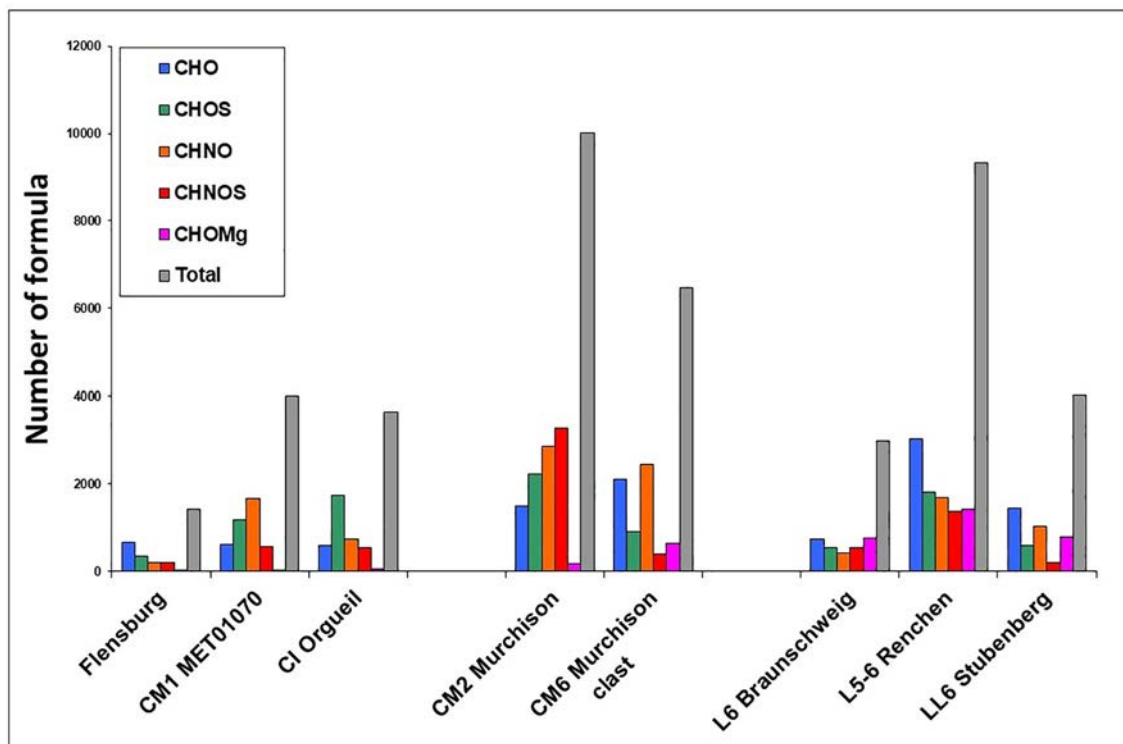
Fig. 22. Number of distinct FTMS-derived molecular compositions indicating the relatively minor number of species for soluble organic matter (SOM) of Flensburg in comparison with that of bulk Murchison and its CM6 fragment. In addition, the number of species for selected CM1, CI, and metamorphosed ordinary chondrites of recent German meteorite falls (Bartoschewitz et al., 2017; Bischoff et al., 2017a, 2019b) are provided.

Reststrahlen bands (RBs) are characteristic IR bands related to the stretching and bending of the Si-O ions and therefore to the chemical composition of the sample (e.g., Pieters and Englert (1993) and references therein). The most intense RB is at 9.92 μm, which is again comparable to the CI1 samples analyzed. The other four samples clearly display different RB in terms of position and shape. Measured at the i20;e15 geometry, the most intense RB of the Flensburg thin section is at 10.11 μm.

The spectrum of Flensburg contains three shoulders between 10 μm and 12 μm that are not present in the spectra of Alais and Orgueil. However, the Flensburg spectrum has a small feature at 12.08 μm which is also seen in the CI1 spectra.

Fig. 23b shows the IR spectra of Flensburg, Alais, Orgueil and Cold Bokkeveld in the wavelength region between 2 μm and 4 μm. All four spectra contain a sharp absorption trough at around 2.7 μm with varying "intensity". Especially in the spectra of Alais and Cold Bokkeveld between approximately 2.7 μm and 3.2 μm a broad trough is visible, but also a very shallow one in Orgueil and Flensburg. At around 3.48 μm, three absorption bands arise that are associated with aliphatic C-H bonds.

6.2. Magnetic properties

Magnetic mineralogy. The most characteristic magnetic properties of Flensburg are summarized in Fig. S11. The coercivity spectrum of Flensburg shows a simple coercivity distribution peaking at 11 mT, suggesting that the magnetic mineralogy is dominated by a single and relatively low coercivity mineral. The presence of a magnetic Verwey transition observed at 120 K in the low temperature magnetic measurements indicate that this mineral is magnetite. The S_{-300} value of 0.985 indicate the absence of any significant amount of high-coercivity ferromagnetic minerals, such as monoclinic pyrrhotite, in the meteorite, which is consistent with TEM observations. This is also suggested by the low B_C and B_{CR} values (10.9 mT and 33.0 mT). The M_{RS}/M_S ratio of 7.96 x 10^{-2}, and B_{CR}/B_C ratio of 3.02 indicate a pseudo-single domain grain size, i.e., magnetite grains in the micron size range. This small grain size also accounts for the rather smooth and small Verwey transition observed in the magnetic susceptibility signal.

Saturation magnetization M_S is 3.52 Am^2/kg, corresponding to 3.83 wt.% of magnetite using $M_S = 92$ Am^2/kg for the magnetite. Indeed, the substitution by a few wt.% of SiO_2 has an insignificant effect on M_S at room temperature (Yamanaka and Okita, 2001). Thus, Flensburg contains much more magnetite than CM chondrites. This value of 3.83 wt.%, combined with the meteorite bulk density of 1.98 g/cm^3 (see above), corresponds to a magnetite abundance of 1.46 vol%, in reasonable agreement with the 1.9 vol% obtained by point-counting (Table 1). The magnetic susceptibility of Flensburg is $\log\chi = 4.35$ (where χ is in 10^{-9} m^3/kg; Fig. S12). It was measured on five
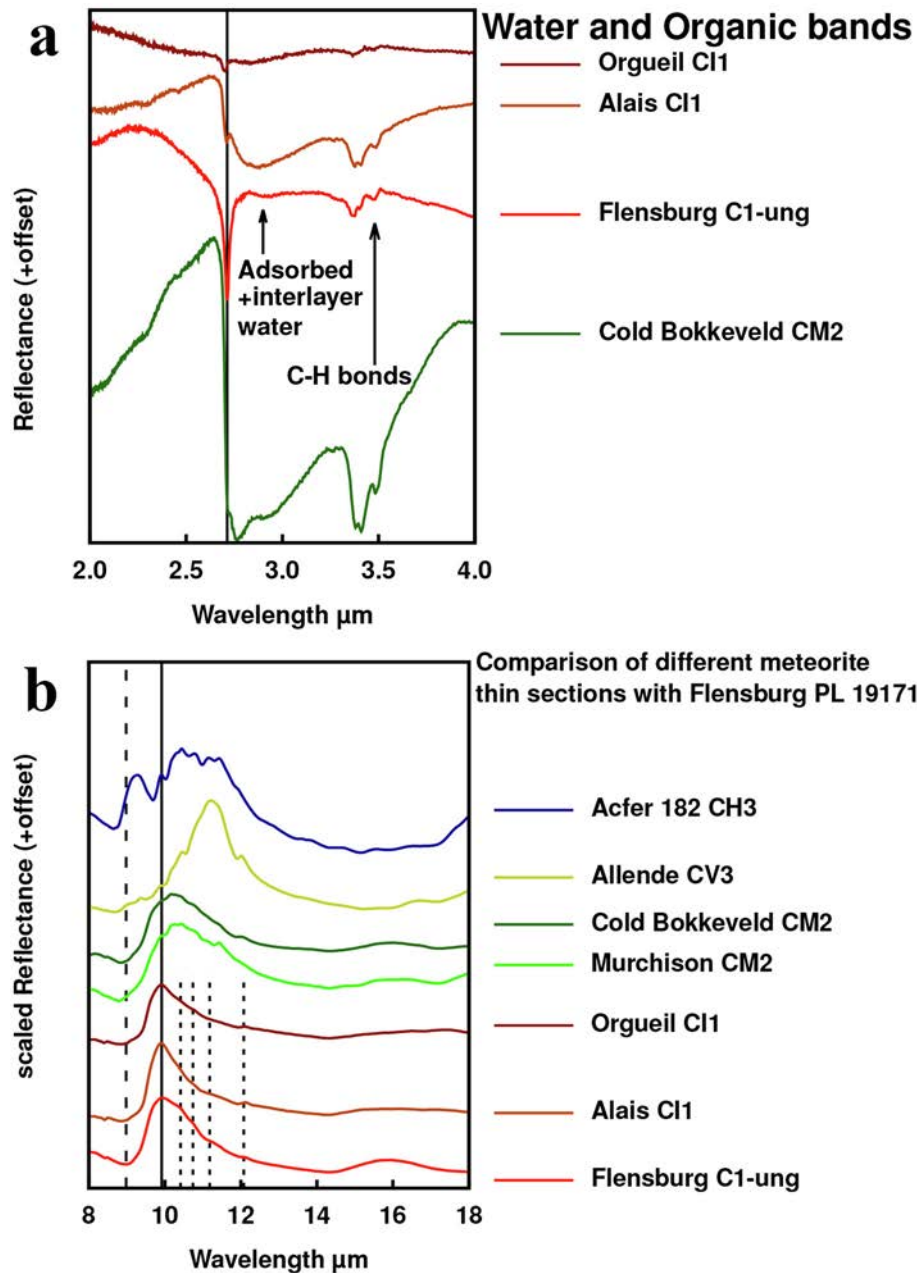
Fig. 23. (a) The infrared spectra of Flensburg, Alais, Orgueil, and Cold Bokkeveld in the wavelength region between 2 μm and 4 μm. (b) The infrared spectrum (IR) between 8 μm and 18 μm of a thin section of the Flensburg meteorite compared to spectra of other meteorites.

samples with mass ranging from 267 mg to 24.5 g (the main mass and sub-samples from the main mass), with identical results (standard deviation: 0.011). This is evidence of a very homogeneous magnetite concentration down to small size (a few dozens of mg at least).

Paleomagnetism. The paleomagnetic record of meteorites is a unique tool to estimate the past magnetic field in the solar systems. In particular, the paleomagnetism of meteorites that have suffered intense aqueous alteration, like Flensburg, has given insights to the intensity of the disk magnetic fields generated within the solar nebula (Cournède et al., 2015), or to the location of formation of meteorite

parent asteroids (Bryson et al., 2020). However, although the meteorite sample reached the laboratory within days after its fall, the natural remanent magnetization (NRM) of the studied 267 mg Flensburg sample show all the characteristics of complete remagnetization by a strong magnetic field originating from a magnet: curved demagnetization paths, and high NRM/sIRM ratio (0.21; sIRM = saturation isothermal remanent magnetization). The evolution of the remnant magnetization REM' with an alternating field (see Gattacceca and Rochette (2004) for a detailed explanation about this method) shows that the strong field remagnetization affects the whole coercivity

spectrum of the meteorite, up to 100 mT. In other words, any extraterrestrial magnetic record has been erased. This is unfortunate and highlights the extremely bad habit of testing meteorites with magnets. It is noteworthy that the measurement of magnetic susceptibility that is more quantitative than any "magnet test", does not result in any remagnetization, and is easy to perform even in the field (e.g., Folco et al., 2006); this should be encouraged among meteorite hunters, collectors and dealers.

7. DISCUSSION

7.1. General remarks

The short-lived radionuclides of the complete Flensburg meteorite measured from October 11 until October 28 clearly confirmed the connection of the Flensburg meteorite with the bolide event over Schleswig-Holstein on September 12, 2019. Thus, Flensburg is the 33rd meteorite fall in Germany and the fourth recovery fall in the last seven years after Braunschweig (2013), Stubenberg (2016), and Renchen (2018) (Bartoschewitz et al., 2017; Bischoff et al., 2017a, 2019b).

7.2. Significance of mineralogical features for classification

As shown in the results, many different aspects of the mineralogical, chemical, and isotopic data suggest that Flensburg is best classified as a unique carbonaceous chondrite rather than a member of the CI, CM, or CR groups. Considering the primary petrographic properties for classification, this assessment is based on (a) the lack of olivine and pyroxene grains (transformed into phyllosilicates; main characteristic of a type 1 chondrite), (b) the rather small mean size (~170 µm) of relict chondrules and their abundance (chondrules in CM and CR chondrites are larger and their abundances in CR chondrites are much higher (Weisberg et al., 2006; Weisberg and Huber, 2007)), and (3) the high abundance and mineralogy of carbonates compared to those in CI and CM1 chondrites (Table 1). These mineralogical features alone indicate that Flensburg is a C1-ung chondrite. The following discussion will further describe different mineralogical, chemical, and isotopic aspects of Flensburg that clearly prove Flensburg is a unique C1 chondrite.

The overall texture of Flensburg is chondritic with aqueously-altered chondrules embedded in a fine-grained groundmass. The chondrules do not have typical accretionary dust mantles as found in CM chondrites (e.g., Metzler et al., 1992; Metzler and Bischoff, 1996), but often contain areas rich in sulfide laths (Fig. 4). The average size of the relict chondrules in Flensburg (~170 µm) is certainly significantly lower than that of CM chondrites (270 µm) as determined for Murray by Rubin and Wasson (1986). Thus, Flensburg cannot result from further alteration of a Murray-type carbonaceous chondrite. Apparent differences also exist considering the matrix texture and mineralogy. While in primary accretionary clasts of Maribo and Cold Bokkeveld (Fig. 24) an internal matrix texture is visible – the TCI-objects (Tochilinite-Cronstedtite-Intergrowth) are
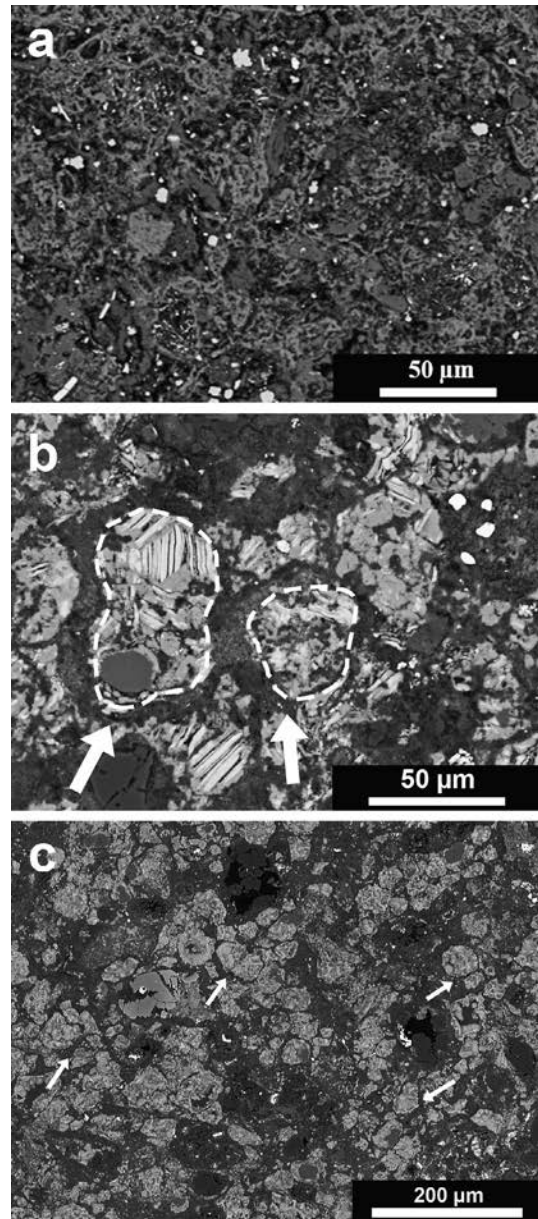
Fig. 24. Comparison between the internal matrix textures of (a) Flensburg, (b) Maribo, and (c) Cold Bokkeveld. The matrix of Flensburg is almost featureless, whereas in Maribo TCI-rich objects are coarse-grained and surrounded by thin layers of accretionary dust (arrows). Some of these objects are indicated by dashed lines. In a clast of the Cold Bokkeveld (CM-breccia) the TCI-objects (light grey) are well-separated from each other by thin rims (dark grey; arrows). BSE-images.

surrounded by thin dust rims – no distinct features can be recognized in the matrix of Flensburg (Fig. 24a). The absence of these TCI-objects is related to the scarcity or even complete absence of tochilinite in Flensburg as determined by TEM-studies. This observation is in good agreement with the high abundance of sulfides in Flensburg (Table 1), since most S is present in sulfides rather than in tochilinite. The 3.8 vol.% of sulfides within the bulk

meteorite obtained by point-counting indicate a S concentration of roughly 1.4 ± 0.4 wt.%, which is similar to the value of ~ 2.0 wt.% obtained by defocused-beam microprobe analysis (n = 135; The Meteoritical Bulletin no. 109).

The abundances and sizes of troilite lamellae in TEM sample F01 are strongly variable and suggest that there are gradients of the bulk Fe,Ni/S ratio across the crystals. This is also consistent with the variability of pyrrhotite diffraction patterns observed. The variable troilite/pyrrhotite volume ratios indicate that the bulk Fe,Ni/S ratios of the original MSS spanned a wide range and suggests changing fS_2 during crystal growth.

The unique breccia Kaidun contains clasts that may be related to Flensburg (e.g., Zolensky and Ivanov, 2003; Zolensky et al., 1996). The microstructures of the exsolved troilite and the overall appearance of the phyllosilicate-sheathed low-Ni iron sulfide crystals in Flensburg are strikingly similar to those observed in the Kaidun CM1 lithology (Harries and Zolensky, 2016). In analogy to their results, the formation temperature of the sulfide must have been greater than 100°C, because troilite exsolution requires that the initially MSS precursor formed homogeneous above this solvus temperature.

The TEM samples F01 and F03 show unusual and variable superstructure reflections of pyrrhotite that cannot be indexed consistently (Fig. 7a–c). They are streaked out along the reciprocal c^* direction and appear to represent poor or atypical vacancy ordering from initially disordered MSS (1C-pyrrhotite). This is possibly a result of insufficient time during cooling through temperatures below the onset of vacancy ordering (<200°C for Fe,Ni/S ratios > 0.91 at.).

The observation that no exsolved pentlandite was found in the pyrrhotite crystals of Flensburg is in sharp contrast to the composite sulfide crystals in the Kaidun CM1 lithology, which contain about 1.8 at.% Ni in bulk (molar Ni/(Fe + Ni) ≈ 0.04). In principle, the Flensburg pyrrhotite should have exsolved pentlandite (Fig. S4), but the process was apparently hindered by slow kinetics.

Because the pyrrhotite crystals in Flensburg have substantially lower Ni contents than those in Kaidun, it appears that they formed at lower temperatures – possibly at 150–200°C, if the original sulfide before troilite exsolution was in equilibrium with the separately coexisting pentlandite and had intermediate metal/sulfur ratios around 0.95 (Fig. S4). Using the relations of Harries and Zolensky (2016), the bulk composition of the sulfide and its co-formation with magnetite suggest S fugacities (fS_2) between about −20 (150°C) and −17 (200°C) log units (bar) and O fugacities (fO_2) between about −50 (150°C) and −44 (200°C) log units (bar). This points to high fS_2 that should have stabilized pentlandite against other Ni-rich sulfides such as heazlewoodite (e.g., Klein and Bach, 2009).

The temperature interval of 150–200°C requires hydrostatic pressures of >4 to >18 bar, respectively, to stabilize liquid water along its vapor pressure curve. Hence, catastrophic decompression by collision events or pressure-driven disruption might have led to volatile degassing and rapid cooling (Wilson et al., 1999).

Unlike similar sheath serpentines surrounding the pyrrhotite of the Kaidun CM1 lithology, the sheathing phyllosilicates of Flensburg do not display the frequent intermixing of serpentine and chlorite. The sheath phyllosilicates of two previously studied Kaidun FIB samples (Harries and Zolensky, 2016) were re-analyzed using the same conditions as the Flensburg samples. They are considerably less Na-rich (~ 0.01 atoms per formula unit) and contain more Fe ($\sim 10\%$ Fe^{3+} in total Fe).

In a Mg-Fe-(Si + Al) ternary compositional diagram (Fig. S5), the Flensburg serpentines extend the compositional trend of serpentines observed in CM2 and Kaidun CM1 lithologies (Zolensky et al., 1996) toward Mg- and Al-rich compositions. This is consistent with a high degree of hydrothermal alteration in which serpentines progressively become enriched in Mg relative to Fe (Browning et al., 1996).

The variable compositions of serpentine in Flensburg, the Mg-Fe zoning of vein serpentine, and the dolomite to calcite transition in composite carbonate grains suggest variable fluid compositions during alteration. The remarkable Na content in the sheath serpentines of Flensburg suggests a large Na activity in the aqueous fluid (e.g., as Na carbonate) that formed them during sulfide precipitation. This was apparently distinct from the conditions in the clast of Kaidun. Sodium could have been leached from the altered chondrule mesostases and subsequently been concentrated in the fluid after a significant amount of water had already been incorporated into the previously formed phyllosilicates.

Considering magnetite and chromite, the high Ti content of the chromite and the high Si content of the magnetite are unusual in chondrites (e.g., Johnson and Prinz, 1991; Wlotzka, 2005; Bjärnborg and Schmitz, 2013). Because chromite is strongly resistant to aqueous alteration, the chromite core of the composite grain likely represents a primary mineral of the chondritic lithology prior to alteration and served as a site of heterogeneous nucleation for later magnetite growth. In TEM, the contact between the chromite core and the magnetite rim is very sharp on the nm scale. It shows no resolvable diffusion profile, suggesting that virtually no chemical equilibration took place. The lack of detectable Fe^{3+} and the elevated Mg, Al, and Ti abundances in the chromite core suggest formation under reducing nebula conditions from refractory-rich material.

At the TEM-scale, parts of the magnetite rims and larger grains are heterogeneous due to nanoscale inclusions (Fig. 11b). These appear to be Fe-rich silicates, but these have not been identified conclusively. Regions of apparently inclusion-free magnetite also show elevated Si contents of about 0.22 atoms per formula unit, suggesting that Si is substituted into the structure. A review of the earlier studied Kaidun samples also revealed one magnetite grain that contains very similar nanoscale inclusion of Fe-rich silicates. However, the inclusion-free regions of this grain contain little Si. Silicon-bearing magnetite and nanoscale segregation of Si-rich phases are quite common in terrestrial samples, but little is known about the physicochemical conditions that facilitate Si substitution (Xu et al., 2014). This requires further study to understand the significance for the hydrothermal environment.

7.3. Significance of the isotopic study of carbonates

A comparison of O and C isotopic compositions with CM literature values (Fig. 13b) by Telus et al. (2019) demonstrates that dolomites in Allan Hills (ALH) 83100 are quite similar to those of Flensburg, while ALH84034 and MET01070 dolomites scatter to lower $\delta^{18}O_{VSMOW}$ values rather but comparable $\delta^{13}C_{VPDB}$ values. This indicates similar dolomite formation conditions concerning temperature and oxygen fugacity and/or carbon source(s). The isotopic compositions of calcites in these Antarctic carbonaceous chondrites frequently range to significantly higher $\delta^{18}O_{VSMOW}$ values (+50‰) and many of them (particularly ALH calcites) are at the low end of the Flensburg calcite $\delta^{13}C_{VPDB}$ values (+10 to +30‰). Obviously, Flensburg calcites therefore appear to fill the gap between dolomite and most CM calcite data with $\delta^{13}C_{VPDB}$ values of +30 to +50‰ and $\delta^{18}O_{VSMOW}$ values of +15 to +25‰. This indicates a somewhat closer genetic relationship between Flensburg dolomites and calcites than for CM chondrite carbonates. The very similar Mn-Cr ages and very similar $\delta^{18}O_{VSMOW}$ values indicate that there was most probably a shorter formation time interval between Flensburg calcites and dolomites at similar conditions (particularly similar formation temperatures) during prograde carbonate formation. The modeling curves in Fig. 13b were calculated according to Alexander et al. (2015) from a starting composition of $\delta^{13}C = +5$ and $\delta^{18}O = +5$ and indicate that many Flensburg calcites formed at relatively higher temperatures than those present in CM chondrites. Flensburg carbonate data could be explained by a scenario involving early formation of dolomite and many calcites from a CO dominated fluid at high temperatures, followed by calcite formation from fluids with higher CO_2 content, and partly lower temperatures.

A distinction between type 1 and type 2 calcites in Flensburg, as is observed for CM chondrites (e.g., Tyra et al., 2012, 2016; Lee et al., 2013) was not found in this study. The $\delta^{18}O_{VSMOW}$ composition of calcites in Flensburg does not extend to values as high as those observed for the least altered CM chondrites Paris and Maribo, but are at the lower end of the compositional range of calcites in other CM chondrites of lower petrologic type (Verdier-Paoletti et al., 2017). There is no simple correlation between the O and C isotope composition of homogenous calcites, zoned calcites, and sulfide-associated calcites, but the latter occasionally extend to higher $\delta^{18}O$ values indicating that some Flensburg calcite grains possibly formed continuously from an evolving aqueous solution. However, episodic fluid pulses cannot be excluded, particularly if the difference in $\delta^{18}O_{VSMOW}$ of sulfide-associated dolomites and other dolomite grains is considered (Fig. 12c). This would imply that they formed during different events, probably starting with the sulfide-associated dolomites from slightly different fluids. This may require an interruption of the aqueous alteration possibly induced by a slight discontinuity of the thermal evolution possibly caused by early brecciation and relocation of the Flensburg sample in the parent body during the collisional growth of the parent body (see below).

The Mn-Cr ages for Flensburg calcite and dolomite of 4564.6 ± 1.0 Ma and 4564.6 ± 1.3 Ma, respectively, are nominally the oldest carbonate ages obtained so far for carbonaceous chondrites, if compared to previous studies using carbonate standards for determinations of the RIY (Jilly-Rehak et al., 2017; Fujiya et al., 2012, 2013). The intergrowth relationships suggest that the carbonates formed more or less contemporaneously with the pyrrhotites. Carbonate formation in CI or CM chondrites is generally considered to have occurred before or close to reaching peak temperatures of aqueous alteration in CI and CM parent bodies (Krot et al., 2015). Formation temperatures were estimated based on their O isotopic composition and thermodynamic modelling (Clayton and Mayeda, 1984; Zolensky et al., 1989a,b; Guo and Eiler, 2007) suggesting 100–150°C for CI chondrites, and 20–70°C for CM chondrites. Verdier-Paoletti et al. (2017) inferred even higher average formation temperatures of 110°C for CM chondrites, perhaps ranging from 50°C to 300°C. However, the Flensburg planetesimal was likely heated to higher peak metamorphic temperatures, i.e., >200°C based on the evidence from the pyrrhotites (see above). We suggest that the Mn-Cr age of 4564.6 ± 1.0 Ma is the age of prograde formation of carbonates, soon after accretion of the parent body followed by metamorphic heating due to ^{26}Al decay (see below). Although Mn-Cr ages of calcite and dolomite are indistinguishable by means of Mn-Cr chronology – mainly due to the relatively large errors associated with relative ion yields from the two types of carbonates – mineralogical observations, particularly calcite overgrowth of dolomite, indicate that most dolomites formed before calcite. Remarkably, the SIMS analyses of the dolomites yield a nearly perfect alignment of dolomite data along the isochron, corresponding to a 0.7% error of the slope only. This indicates dolomite formation in a narrow time interval of ca. 70 000 years and would be consistent with an intense and short pulse of dolomite formation, preceded by a period of aqueous alteration allowing significant alteration to drive the pH of fluids sufficiently up.

7.4. Significance of bulk chemical and isotopic properties

7.4.1. Minor and trace elements

As described above, for most elements the concentrations in Flensburg are very similar to those of the median composition of 14 CM chondrites analyzed by Braukmüller et al. (2018). However, there are some distinct differences. Flensburg has about 30% lower concentrations of Zn, Cu, and Pb and slightly higher Na concentrations than the concentrations of these elements in other CM chondrites given by Braukmüller et al. (2018). However, Na does not seem anomalous because the abundances are similar to those for the CM chondrites Boriskino, Nogoya, and Paris (~0.6 wt.% Na_2O; Hewins et al., 2014) and of literature data from Murchison (0.58; Kallemeyn and Wasson, 1981). Of course, Cu, Zn, and Pb in Flensburg seem marginally low considering the data of Hewins et al. (2014), but the data are certainly not sufficiently different enough to make Flensburg chemically a completely different rock, when comparing it with the values for other

CM chondrites. The C content (Table 5) is also lower than is typical for a CM (~2 wt.%; Kerridge, 1985; Alexander et al., 2012, 2013). The low Zn and C may suggest a low initial matrix content, although it is possible that the organic C has been destroyed somehow. A low matrix content would raise the issue of why the water/OH content is so high.

7.4.2. Hydrogen, C, and N elemental and isotopic compositions

As illustrated in Figs. 15–17 the Flensburg carbonaceous chondrite is unique. Its H content (Table 5) is similar to that of a fairly typical CM2 (Kerridge, 1985; Alexander et al., 2012, 2013; Braukmüller et al., 2018). If Flensburg was carbonate-free, then using a C content of 1.54 wt.% and assuming a CM-like H/C≈0.055 (wt.) for its organics, the H in H_2O/OH would be roughly 1.02 ± 0.03 wt.% (9.2 $\pm$ 0.2 wt.% H_2O) and it would have a petrologic type of 1.5 on the 1–3 scale of Alexander et al. (2013). The 1σ uncertainties only take into account the uncertainties in the bulk measurements (Table 5) because at present there is no information on the H/C ratio of the bulk organics. This H_2O/OH content is probably a minimum estimate, not only because it uses the higher of the two measured C contents but also because in situ measurements suggest that Flensburg may contain 3.9 ± 1.0 vol.% carbonate (Table 1). Assuming a density of 2.71 g/cm³ and a C content of 11.98 wt.% for the carbonate (those of calcite) and a bulk rock density of 1.98 g/cm³ (see above), the volume fraction of carbonate would account for ~0.63 wt.% C in the bulk meteorite. Hence, it is possible that about half of the bulk C is in carbonate, which would translate to a somewhat higher proportion of the H in OH/H_2O than estimated above. The bulk H content is lower than those of typical CI1s, CM1s, and CR1s (1.3–1.5 wt.%; Kerridge, 1985; Alexander et al., 2012, 2013; Braukmüller et al., 2018). This is surprising because olivine and pyroxene have been completely altered to phyllosilicates in Flensburg, whereas other chondrites classified as CM1 and CI1 still contain several vol.% of olivine and pyroxene (Howard et al., 2015; King et al., 2015, 2017). The relatively low H_2O might be due to the absence of saponite-like clay minerals, which contain additional interlayer H_2O.

The range of H abundances and isotopic compositions amongst the unheated type 1–2 s can, to first order, be explained by mixing between D-rich organic matter and D-poor H_2O/OH (Alexander et al., 2012). This can be seen in plots of δD vs. C/H (Fig. 25). Here, the C content determined at the Earth and Planets Laboratory (CIW) is used for consistency with the other data shown. The initial isotopic composition of the organic material appears to have been quite similar for all type 1–2 s (δD ≈ 3000–3500‰). For the CIs, CMs, and Tagish Lake the H_2O/OH seems to have had a composition of δD ≈ −450‰, but in the CRs it must have been significantly heavier (δD ≈ 100‰). The bulk H in Flensburg is not only isotopically lighter than even the most altered CM, but it is also displaced to higher C/H than the CM trend. Taken at face value, this would imply that Flensburg accreted water, and possibly organics, that was even more D-poor than that accreted
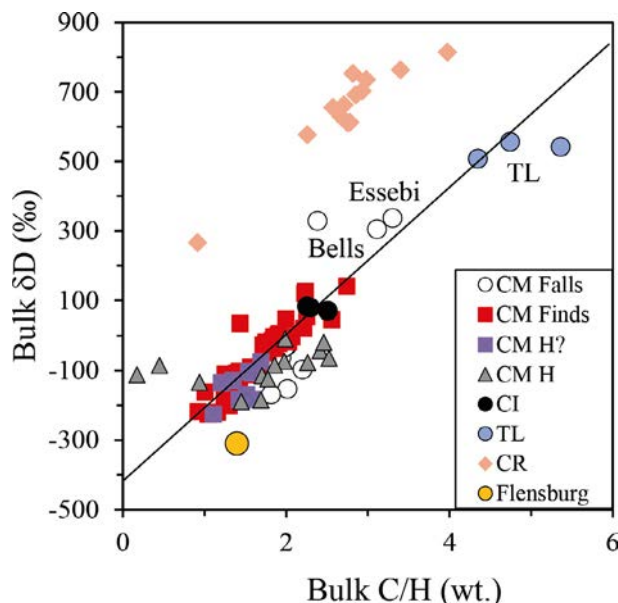

Fig. 25. The bulk δD vs. bulk C/H for type 1–2 carbonaceous chondrites (Alexander et al., 2012, 2013), including Flensburg. This figure illustrates how the H isotopic compositions are primarily determined by mixing of H in C- and D-rich organic matter with C- and D-poor H_2O/OH. The line is a linear fit to the unheated CM finds, but the CIs, the anomalous CMs Bells and Essebi, and the Tagish Lake (TL) lithologies all scatter about this line. The CRs form a separate trend apparently because they accreted more D-rich water ice than the other type 1–2s. Flensburg has a lighter H isotopic composition than any other measured type 1–2. It also falls well to the right of the CM fall line, but this could be due, at least in part, to its apparently high carbonate content. CM H = heated CM chondrite; CM H? = possibly heated CM chondrite.

by the CIs, CMs, and Tagish Lake. However, if Flensburg contains about 0.6 wt.% carbonate C, almost half of the bulk C is in carbonate, which is a higher proportion than in any other type 1–2 chondrite, except perhaps some Tagish Lake lithologies (Grady et al., 2002; Zolensky et al., 2002). Since the δD vs. C/H trend strictly only applies to organic C, after subtracting the carbonate C Flensburg's C/H would decrease by roughly half and it would then fall quite close to the CM trend. Hence it is possible that Flensburg accreted water with a similar isotopic composition to the other type 1–2 chondrites, excluding the CRs.

The bulk C content of Flensburg is intermediate between CMs and CRs. Generally, in chondrites most of the C is in organic material (Alexander et al., 2015). However, in Flensburg almost half of its bulk C might be in carbonate, in which case its organic C content is similar to or less than that in CR and CO chondrites. It has been suggested that the organic C in chondrites is carried by CI-like matrix, which would imply a matrix abundance that is similar to or less than that in CR and CO chondrites (i.e., ≤30 vol.%). Alexander (2019) concluded that water-ice was also accreted in the matrix and generally in roughly CI-like abundances. However, to explain the range of degrees of alteration amongst the CMs and CRs requires either rather heterogeneous accretion of ices or post

accretion redistribution of water. One or other of these processes is also needed to explain the high H to organic C ratio of Flensburg.

Carbonates in unheated C1-2 chondrites typically have high average δ^{13}C values (23–80‰) (Grady et al., 1988; Alexander et al., 2015), while their bulk organic matter is much lighter (−13‰ to −36‰) (Robert and Epstein, 1982; Yang and Epstein, 1983, 1984; Alexander et al., 2007). Flensburg does have one of the highest bulk δ^{13}C values of any type 1–2.

7.4.3. O isotopes

Two principal processes controlled the O isotope compositions of early solar system materials. One process is the exchange between silicate/oxides and ^{16}O-poor H_2O that was produced by CO self-shielding (Clayton, 2002). Materials that were affected by this process fall roughly on a trend with slope 1 in the δ^{17}O vs. δ^{18}O space, which is well-defined by the carbonaceous chondrite anhydrous mixing line (CCAM, e.g., Clayton, 2008). The other process is mass-dependent fractionation, which leads to a correlated shift in δ^{17}O and δ^{18}O roughly along a trend with slope 0.528 (see e.g., Pack and Herwartz (2014) for more details of mass-dependent triple isotope fractionation). The two trends are indicated in Fig. S13a. The CM chondrites span a wide range in both Δ'^{17}O and δ^{18}O, neither following the pure mass-independent nor the pure mass-dependent trend and were affected by exchange with a ^{16}O-poor reservoir and mass-dependent enrichment in δ^{18}O typical of interaction with liquid water.

Clayton and Mayeda (1984) presented an evolution model to understand the composition of components in the CM2 chondrite Murchison. They suggested that the primordial dust fell on the CCAM line and that interaction with liquid water in the CM chondrite parent body shifted the isotope compositions towards higher δ^{18}O values. Depending on the water/rock ratio (W/R), either the rocks shift in δ^{18}O towards higher values (high W/R) or the water shifts towards higher δ^{18}O (low W/R).

The O isotope composition of Flensburg falls on the CCAM (Clayton, 2008) in the field of CM chondrites (Fig. 18), and only marginally overlaps with CR and CV chondrites (Figs. S13a and b). The isotope composition of Flensburg does not overlap with published data on CO chondrites (Fig. S13c). Recently a CM1 clast in Mukundpura was found that also has a light O isotope composition (Findlay et al., 2020).

Assuming similar anhydrous silicate and water O isotopic compositions to those in the CMs, as well as similar alteration conditions, the formation of the hydrous minerals in Flensburg must have occurred at low W/R ratios. Otherwise, its bulk O isotopic composition would have been mass-fractionated away from the CCAM line towards higher δ^{18}O values, which is not the case (Fig. 18).

In terms of the O isotopes only, it is feasible that Flensburg silicates and oxides exchanged O at high temperatures with a ^{16}O-poor H_2O reservoir produced by CO self-shielding (Clayton, 2002). A low-temperature process would lead to mass-fractionation and hence move the materials toward higher δ^{18}O values, away from the CCAM line.

7.4.4. Titanium, Cr, and Te isotopes

The Cr isotopes indicate that Flensburg is similar to CM chondrites. The Ti isotope data analyzed in Münster is also consistent with a CM chondrite affinity, while the Zürich data show a slightly higher, more CV-like, enrichment in ^{50}Ti. This could be due to a nugget effect in the sample aliquot analyzed at ETH Zürich. Hibonites are well documented in CM chondrites and they have been shown to contain highly variable and extreme ^{50}Ti compositions (e.g., Kööp et al., 2016). Mass balance considerations show that a single additional 30–50 μm hibonite grain in the Zürich aliquot could explain the small deviation from the average CM value.

The analyses of the Te concentration and isotopes revealed that Flensburg has a $\delta^{128/126}$Te value different to that of mean CM chondrites (Hellmann et al., 2020), but similar to that of Tagish Lake (C2-ungrouped); however, its Te concentration is indistinguishable to that of CM chondrites (Fig. 21).

7.5. Significance of the noble gas budget

The extremely low abundance of cosmogenic noble gases in Flensburg implies a very short CRE age. All measured noble gases can be explained entirely by trapped components within error, meaning that, on the basis of the noble gases, the CRE age could be anywhere between zero and a maximum age of 0.20 Ma. This upper limit CRE age is consistent with CRE ages determined by long-lived radionuclides (see discussion in Section 7.6) and, therefore, there is no evidence for a complex exposure history. The maximum CRE age falls within the main age cluster of around 0.2 Ma found for CMs (Krietsch, 2020), although the more precisely determined exposure ages in Section 7.6 suggest Flensburg was exposed to cosmic rays in space for much less than any asteroidal meteorite that we know of. Only the lunar meteorite Kalahari 008/009 has a shorter CRE age (Sokol et al., 2008).

Helium, Ne, and Ar isotopes show no solar wind (SW) contributions, as demonstrated by the low ^{4}He, ^{20}Ne, and ^{36}Ar concentrations that are comparable to those in CM chondrites unaffected by SW (Krietsch, 2020). This combined with the low CRE ages implies that Flensburg does not stem from a regolith environment.

Flensburg's trapped noble gas signature is similar to that of CMs, with a major difference being a comparatively low concentration of ^{20}Ne$_{tr}$. The low ^{36}Ar, ^{84}Kr, and ^{132}Xe concentrations fit with those found in strongly aqueously altered CRs and CMs of type 1–2, consistent with the classification of Flensburg as a type 1 carbonaceous chondrites. ^{36}Ar/^{132}Xe (80.0 ± 0.1) and ^{84}Kr/^{132}Xe (0.98 ± 0.09) plot close to Q: $(^{36}$Ar/^{132}Xe$)_Q = 76 \pm 7$ and $(^{84}$Kr/^{132}Xe$)_Q = 0.81 \pm 0.05$ (Busemann et al., 2000) with no evidence of an additional Ar-rich component that is observed in many of the least aqueously altered CMs.

The ^{129}Xe/^{132}Xe ratio is in the typical range for CO3 chondrites (Scherer and Schultz, 2000), and slightly higher than typical CM chondrites. The higher normalized ^{129}Xe/^{132}Xe ratio compared to other Xe/^{132}Xe ratios can be explained by ^{129}I-derived ^{129}Xe.
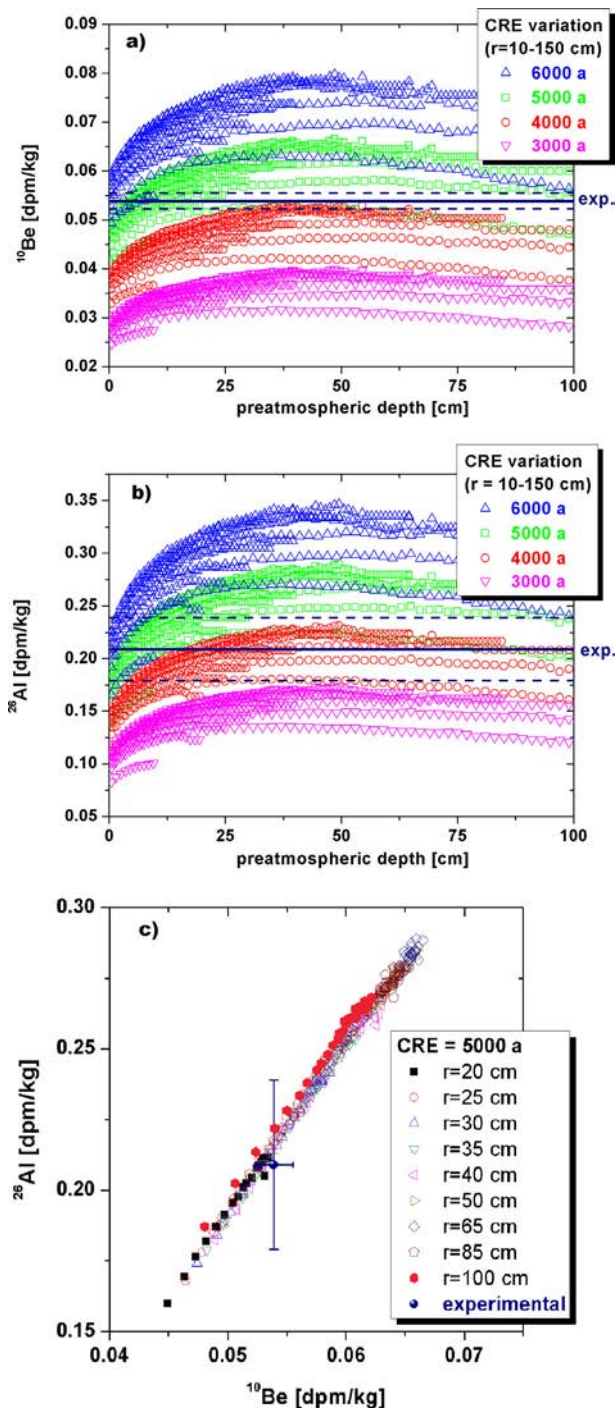
Fig. 26. Comparison of ^{10}Be (a) and ^{26}Al (b) experimental data with theoretical depth- and radius-dependent (r = 10–150 cm) production rates for different cosmic ray exposure (CRE) ages (Leya and Masarik, 2009). Conclusive shielding-conditions for both nuclides are found for a CRE of ~5000 a (c).

7.6. Significance of radionuclide concentrations

The presence of short-lived cosmogenic radionuclides with half-lives as short as 16 days prove the recent exposure to cosmic rays in space of the Flensburg stone (Table 8).

The U, Th, and K concentrations of the Flensburg chondrite are in the same range as those found in gamma-spectrometric studies of recent ordinary chondrite falls like Stubenberg (Bischoff et al., 2017a) or Renchen (Bischoff et al., 2019b).

The short-lived cosmogenic radionuclides are also in the range of values measured for the Braunschweig (Bartoschewitz et al., 2017), Stubenberg (Bischoff et al., 2017a), or Renchen (Bischoff et al., 2019b) meteorites with the exception of ^{60}Co, which is more than two orders of magnitude higher in Flensburg. Such high ^{60}Co activity can only be explained by a rather shielded position of the Flensburg specimen following the arguments of Povinec et al. (2015). Taking density differences between Flensburg and ordinary chondrites into consideration, the ^{60}Co specific activity of 98 dpm kg^{-1} can only be explained if the sample was situated in a minimum depth of 25 cm within a meteoroid – at least for the last 30 years or so.

Results for ^{41}Ca/Ca are based on four counts only, hence, have a high statistical uncertainty. This hinders further interpretation apart from the fact that the low concentrations of both, ^{41}Ca and ^{60}Fe are consistent with the very short exposure of Flensburg in space that can be already deduced from the ^{10}Be and ^{26}Al data alone.

Comparison of ^{10}Be and ^{26}Al data with depth- and radius-dependent (r = 10–150 cm; Fig. 26) production rates based on the work of Leya and Masarik (2009) are presented in Fig. 26. In a first step, ^{10}Be and ^{26}Al theoretical production had been modified for highly-variable exposure, i.e. 500–50,000 a, then followed by exposure for 3000–6000 a only. Both radionuclides point to a short exposure around 5000 a (Fig. 26), if we exclude very small pre-atmospheric radii ≤ 10 cm, which is valid based on the ^{60}Co data. With a very simple density adjustment of the model to Flensburg's density, the meteoroid must have had a minimum size of r > 15 cm.

Using a size of r = 30 cm, consistent with the ^{60}Co data, the ^{14}C result confirms that the exposure age of Flensburg should be ~6000 a, which assumes a density similar to an ordinary chondrite. Some more detailed calculations were undertaken, since Flensburg has a sufficient nitrogen content of 0.027 wt.% to produce ^{14}C from thermal neutron reactions on ^{14}N at a rate of 12.5 atoms/min kg. The production rates from the spallation of O can be determined from scaling ordinary chondrite production rates to be ~40 dpm/kg (r = 15 cm) to 56.5 dpm/kg (r = 30 cm) based on Wieler et al. (1996) and Leya and Masarik (2009). Using these values, we can estimate a ^{14}C exposure age of 5.0 to 7.5 ka. If we further note that the density of Flensburg is ~2.0 g/cm^3 as opposed to the typical value of ~3 g/cm^3 for an ordinary chondrite, then we would obtain values of 7.4–11.6 ka. Hence, we can constrain the ^{14}C exposure age to be ~7 ka (for r = 30 cm), consistent with the ^{10}Be and ^{26}Al estimates of ~5 ka and the ^{60}Co shielding depth estimate, bearing in mind that these age estimates make several assumptions and are unlikely to be more accurate than ± 2 ka. This makes Flensburg besides the desert find Kalahari 008/009 (Sokol et al., 2008) to a sample with one of the shortest known CRE ages; thus, Flensburg is the meteorite fall with the shortest known CRE age. We note that Brown

et al. (1984) gave a similar exposure age estimate for Farmington (an L5 chondrite that fell in 1890) based on ^{14}C and ^{26}Al to be 8.5–11.3 ka. This is the only other meteorite fall, which has been measured, that was not in radioactive saturation for ^{14}C.

7.7. Significance of physical characteristics

Based on the value for the saturation magnetization ($M_S = 3.52$ Am^2/kg) Flensburg contains 3.83 wt.% (1.46 vol.%) of magnetite. For comparison, it contains much more magnetite than typical CM chondrites: the average M_S for CM chondrite falls is 1.01 ± 0.55 Am^2/kg (N = 9, Cournède et al. (2015) and data for Boriskino, Pollen and Santa Cruz), corresponding to 1.10 ± 0.60 wt.% of magnetite. On the other hand, Flensburg contains less magnetite than CI chondrites like Orgueil ($M_S = 9.55$ Am^2/kg), Ivuna ($M_S = 8.85$ Am^2/kg), or the C2-ung Tagish Lake ($M_S = 9.9$ Am^2/kg). These three latter values are averages from previous studies (Brecher and Arrhenius, 1974; Thorpe et al., 2002; Tikoo et al., 2019).

Magnetic susceptibility (log$\chi = 4.35$, where χ is in 10^{-9} m^3/kg; Fig. S12) is in the upper range of CM2s that have an average log$\chi = 3.90 \pm 0.43$ (n = 52; Rochette et al., 2008). The only CM1 measured in Rochette et al. (2008), MET01070, has a much lower susceptibility, log$\chi = 3.63$. Flensburg has similar susceptibility to the C2-ung chondrite like NWA 5958 (log$\chi = 4.12$, measured on a 4.53 g sample). Other C2-ung chondrites like Acfer 094, Adelaide, Bells, and Essebi have much higher susceptibility, with log$\chi = 4.62$, 4.76, 4.82, and 4.85, respectively (Rochette et al., 2008).

Sulfides do not contribute significantly to the magnetic properties, implying that only a very minor fraction can be in the form of monoclinic pyrrhotite, which is confirmed by TEM studies.

The IR-spectroscopic characteristics of a Flensburg thin section were analyzed and compared with the spectra with other carbonaceous chondrites. Salisbury et al. (1991) found in powder reflectance spectra of Orgueil a CF between 8.64 μm and 8.55 μm and in Alais a value of 8.85 μm. The slight shifts between our measurements on Flensburg compared with those of Salisbury et al. (1991) and the shift of the CF between the two different measurements with varying viewing geometry are most likely due to a change in the sampled surfaces. A small change in the viewing geometry results in a change of the analyzed area which probably has a different bulk mineralogical composition. Therefore, the wavelength of the CF around 9.03 μm in the spectra of the Flensburg sample reflects its mineralogical similarities to those of the CI1 samples.

In addition, the strongest RB found at around 10.02 μm in the spectrum of the Flensburg meteorite, is comparable to the spectra of the measured CI1 meteorites. This peak position is a result of the presence of phyllosilicates occurring in the samples (Beck et al., 2010).

The CM, CV, and CH samples show other distinct RBs, which demonstrates the difference between these meteorites and Flensburg. The shoulder in the spectrum of Flensburg at about 11.29 μm is probably due to the presence of calcite

or ankerite (Green and Schodlok, 2016). Olivine has also a strong feature at this wavelength (e.g., Morlok et al., 2020) and, therefore, the feature may indicate the presence of minor amounts of olivine; however, olivine was not positively detected by optical microscopy, SEM, and TEM, but maybe by X-ray techniques (see SM). It is also possible that all observed shoulders are an effect of pentlandite. In this wavelength region, pentlandite also has some weak features (seen in a pentlandite spectrum laag02 taken from RELAB spectral database). In contrast to this assumption, the most intense RB peak of pentlandite is at ~9.5 μm. At this wavelength no clear peak or shoulder could be observed in the spectrum of Flensburg.

In the wavelength region around 3 μm, water absorption bands with varying depths are present in the spectra of Flensburg, Orgueil, Alais, and Cold Bokkeveld (Salisbury et al., 1991). The water bands can be differentiated into OH that is bound within the crystal structures and water either between layers in minerals or that is adsorbed at the surface (Beck et al., 2010). The depths of the band for the adsorbed water in Flensburg are much shallower than in Alais and Cold Bokkeveld indicating that these samples have some terrestrial water adsorbed (Beck et al., 2010). In contrast to the study of Beck et al. (2010), our sample of the Orgueil meteorite does not show a strong band due to adsorbed water indicating that this sample is probably "fresher" and less contaminated than the samples used by Beck et al. (2010).

The strong absorption band at 2.71 μm in the spectra of Flensburg and Alais, (which is slightly shifted in Orgueil and weakly visible in the spectrum of Cold Bokkeveld) is due to OH stretching in phyllosilicates (Beck et al., 2010). The strongest and clearest visible absorption feature in the Cold Bokkeveld sample measured in this study is at about 2.76 μm. Beck et al. (2010) argue that this strong absorption band around 2.7 μm originates from Mg-rich serpentines. The wavelength of this feature is also affected by the total amount (wt.%) of phyllosilicates in the probed sample (Beck et al., 2010). According to visual inspection of the figures presented in Beck et al. (2010), the intensity at a wavelength of 2.71 μm observed in the spectrum of Flensburg meteorite is due to approximately 80 wt.% of phyllosilicates.

The total water content of CM chondrites can be determined by the depth of the 2.7 μm absorption band (Beck et al., 2018). Applying this method to the Flensburg spectrum leads to an assumed water content of around 8.5 wt.% (H = 0.94 wt.%), which is in good agreement with the measured mean value of 9.88 wt.% (H = 1.10 wt.%) (Table 5).

Both analyzed IR spectral regions indicate that the Flensburg meteorite is comparable to CI meteorites because of their overall similar mineralogical compositions; however, the Flensburg spectrum exhibits some characteristics in the wavelength region between 8 μm and 18 μm that are not present in the spectra of the CI chondrites.

The results for Flensburg presented here can also be used to interpret remote observations of asteroids, and can help to determine the surface mineralogy as well as the degree of aqueous alteration on asteroids. Bates et al.

(2020), who also studied highly altered carbonaceous chondrites, suggest after comparing IR spectra of highly altered carbonaceous chondrites with the preliminary results from Hayabusa2 and OSIRIS-REx that aqueously altered chondrites may be suitable analogues to the surface materials of the asteroids Ryugu and Bennu (e.g., Kitazato et al., 2019; Hamilton et al., 2019).

7.8. Mineralogical and textural similarities to other C1 and CI chondrites and related fragments in breccias

Recently, an increasing number of xenoliths within brecciated meteorites have been described and characterized. This also includes a number of aqueously altered clasts in numerous achondrite and chondrite groups such as ureilites, howardites, CR, CH, and ordinary chondrites (e.g. Zolensky et al., 1996; Endress et al., 1994; Gounelle et al., 2005; Patzek et al., 2018a,b). Although the general mineralogies of the clasts are similar to those of CI and CM chondrites, there are differences in the mineral composition (Patzek et al., 2018a). Comparing the mineralogical features of Flensburg to those of CI chondrites and C1 clasts in several brecciated meteorites, the high abundances of sulfide laths are unique to Flensburg and CM1 clasts in the carbonaceous micro breccia Kaidun (Zolensky et al., 1996; Harries and Zolensky, 2016). The abundance of magnetite grains is lower than that of CI chondrites as determined using similar techniques, whereas the abundance of carbonates is clearly higher (Table 1; Alfing et al., 2019). Magnetite and carbonate grains are less abundant or even absent in the CM1 lithologies of Kaidun. The distribution of the different mineral phases within the sample is somewhat heterogenous, but – although some clasts in Flensburg exist (see below) – the obvious and typical brecciation features as observed for CI chondrites, where several lithologies can have highly variable abundances of different minerals (Endress and Bischoff, 1993; Morlok et al., 2006; Alfing et al., 2019), are not observed. There is also a clear difference between Flensburg and CI chondrites and C1 clasts in the abundance of chondrules (or relict chondrules): While the texture of Flensburg is dominated by abundant relict chondrules that are often rimmed by sulfide laths, these features are lacking in the CI chondrites and all observed C1 clasts. Although the CM1 clast in Kaidun is the closest analogue to Flensburg, the clast only shows a limited abundance of relict chondrules with sulfide rims (Harries and Zolensky, 2016). Additionally, the magnetite grains in Flensburg contain considerable concentrations of Si ($\sim$4 wt.% SiO_2), which is much higher than for magnetite in the CM1 clast in Kaidun. Silicon is below detection limits in magnetite in CI chondrites and C1 clasts in brecciated meteorites (compare with Section 3.3.4).

In summary, Flensburg is an outlier among aqueously-altered carbonaceous chondrites with its notably different mineralogy and texture, implying a diversity of parent bodies with slightly different elemental and isotopic composition within the early solar system that ultimately led to slightly different alteration conditions. This is also suggested as a possibility by a recent study considering the O isotopic composition of chondrite meteorites (Greenwood et al., 2019; see below).

7.9. Classification of Flensburg

For an appropriate classification of Flensburg, all characteristics (mineralogical, textural, physical, chemical and isotopic) discussed above will be considered.

Several different mineralogical-textural schemes have been developed to quantify the degree of aqueous alteration seen in CI and CM chondrites and to define distinct lithologies (e.g., McSween, 1979b; Endress and Bischoff, 1993; Browning et al., 1996; Rubin et al., 2007; Morlok et al., 2006; Howard et al., 2009, 2015; Lindgren et al., 2013; Garenne et al., 2014; Alfing et al., 2019; Lentfort et al., 2020). In Flensburg, mafic minerals (olivine, pyroxenes) have been completely transformed into secondary phases. This clearly requires a type 1 classification. A relationship to CI1 chondrites can be ruled out based on several mineralogical parameters (e.g., the occurrence of relict chondrules, the modal abundance of minor phases, Si in magnetites). Flensburg – although having clasts – does not have the typical brecciated texture observed in almost all CI and CM chondrites (e.g., McSween, 1979b; Endress and Bischoff, 1993; Morlok et al., 2006; Lindgren et al., 2013; Alfing et al., 2019; Lentfort et al., 2019, 2020). As shown in Fig. 24, the internal texture of the fine-grained material is completely different to those in typical lithologies from CM chondrite breccias.

Based on the value for the saturation magnetization ($M_S = 3.52$ Am^2/kg), Flensburg contains 3.83 wt.% of magnetite, which is much more magnetite than typical CM chondrites have, but less than in CI chondrites (Table 1).

Although the composition of Flensburg is very similar to the median composition of 14 CM chondrites analyzed by Braukmüller et al. (2018), there are some differences such as the lower concentrations of Zn, Cu, and Pb (about 30%) in Flensburg. Considering the H, C, and N elemental and isotopic compositions as illustrated in Figs. 15–17, clearly, the Flensburg carbonaceous chondrite is unique. Other isotopic studies show that Flensburg has a $\delta^{128/126}$Te value that is different from that of mean CM chondrites.

Since Flensburg contains carbonates that formed very early, it can certainly be postulated that the rock represents a unique parent body not sampled by other carbonaceous chondrite samples. Thus, Flensburg is a very old and unique carbonaceous chondrite breccia.

7.10. Flensburg and the abundance and nomenclature of organic components

FTICR mass spectrometry. The FTICR mass spectra of Flensburg soluble organic matter (SOM) show comparatively smaller numbers of mass peaks than those of Murchison SOM (CM2.5-CM6 breccia; Fig. S14) and offer mass spectra profiles that are very similar to those observed for the CM1 MET01070 (Fig. S14b). Flensburg SOM shows a group of intense mass peaks that are attributed to highly oxidized poly-sulphur compounds (Fig. S14a). Expansions

of nominal mass clusters (e.g. m/z 311; Fig. S14b) also show fewer signals than those of Murchison extracts. Of the ~1400 assigned molecular compositions of the Flensburg extract, CHO compounds are most abundant. This is in clear contrast to Murchison SOM, in which only <20% of the ~9850 assigned molecular compositions accounted for CHO compounds, whereas heteroatom-containing compounds follow the order CHNOS > CHNO > CHOS (Fig. S15). Low abundances of soluble organics in CM1 chondrites have been attributed to aqueous alteration at higher temperatures (e.g., Botta et al., 2007; Aponte et al., 2011; Glavin et al., 2011).

The van Krevelen diagram is a widely used tool to characterize SOM of terrestrial (Meckenstock et al., 2014; Hertkorn et al., 2013, 2016) and extraterrestrial origin (Schmitt-Kopplin et al., 2010; Hertkorn et al., 2015). Commonly, thousands of assigned CHNOS and CHOMg (Ruf et al., 2017) molecular compositions, which each may represent many isomers (Hertkorn et al., 2007), are plotted according to their H/C versus O/C atomic ratios; in addition, the area of the data points indicates the relative proportions of these compounds.

Flensburg, with its large extent of aqueous alteration shows the highest proportions of CHO compounds, whereas the solubilization of heteroatoms N and S appears to require more elevated temperatures. This seems reasonable, given that the synthesis of CHNO compounds probably preceded that of CHO compounds (Schmitt-Kopplin et al., 2010). Primordial CHNO compounds can carry much more numerous and molecularly diverse coordination motifs (Derenne et al., 2012) than CHO compounds (in particular for hydrogen-deficient molecules). Hence, cohesion of intricate mixtures of CHNO compounds in the presence of mineral matrices is larger than that of CHO, while hydrogen-deficiency in general attenuates water solubility in the case of CHO and CHNO compounds (Hertkorn et al., 2015). However, oxygenated CHOS compounds commonly carry O-rich, S-containing functional groups, which facilitate water solubility. Furthermore, these compounds ionize well in negative electrospray ionization (Gonsior et al., 2011). Organomagnesium compounds (CHOMg) that were shown previously as a marker for metamorphism (Ruf et al., 2017) and were abundant in the metamorphosed chondrites Braunschweig, Stubenberg, and Renchen and in the CM6 clast in Murchison (Bartoschewitz et al., 2017; Bischoff et al., 2017a, 2019b; Kerraouch et al., 2019) were entirely absent in the solvent extract of Flensburg (Fig. 22). This absence of CHOMg compounds is consistent with mass spectra obtained for MET01070 (CM1) and Orgueil (CI1) extracts, reflecting the supposedly low temperatures and high degree of aqueous alteration. This also excludes later annealing by impact. Van Krevelen diagrams revealed a relative depletion of certain sections of elemental ratios in the Flensburg extracts in contrast to SOM in Murchison (and other CM2 meteorites), which occupy rather contiguous molecular series for CHO, CHNO, CHOS and CHNOS compounds (Fig. S15). These patterns indicate rather selective processing of SOM in Flensburg, which can be divided into abundant saturated CHO (H/C ratio from 1.7 to 2.0) and considerably less abundant but

clearly visible series of unsaturated CHO compounds (H/C ratio from 0.7 to 1.5). Some of these probably represent mono-, di- and tri-oxygenated polyaromatic hydrocarbons, which remained in solution owing to their functionalization (Fig. S15).

The ^1H NMR spectroscopy. The ^1H NMR spectra of Flensburg C1 methanolic extracts show substantial line broadening compared with those of Murchison (Hertkorn et al., 2015) and other meteorites, most likely arising from the increased proportions of dissolved minerals and metal ions. This is probably related to the increased degree of aqueous alteration, which induces corrosion of metals and transformation into soluble salts (Morlok and Libourel, 2013). Paramagnetic transition metal ions (e.g., $Fe^{2/3+}$, Mn^{2+}, Ni^{2+} and Cr^{3+}) induce considerable line broadening in ^1H NMR spectra (Bertini et al., 2005). Acetic acid (12% of ^1H NMR integral), methanol (not shown) and formic acid (<2% of ^1H NMR integral) are recognizable in Flensburg extracts. While the fundamental aliphatic branching units, which represent an averaging of many similar chemical environments (Hertkorn et al., 2015), were similar for Murchison and Flensburg (Fig. S10), the latter shows higher proportions of background NMR resonances indicative of more elaborate aliphatic branching patterns. This includes substituted alicyclic rings and remote O functionalization (Table 10), in accordance with a higher degree of aqueous alteration. By analogy to the FTICR mass spectra, the proportions of distinct NMR resonances in Flensburg are smaller than those in Murchison, indicative of smaller amounts of specific recognizable species (molecules) in Flensburg. The region of the NMR spectrum populated by aromatic protons is dominated by resonances indicative of fused aromatic compounds with two rings (polyaromatic hydrocarbons, i.e. naphthalene derivatives) and polycarboxylated benzene derivatives confirming the FTICR-MS results; on the other hand, the proportions of single aromatic compounds are smaller than those in Murchison SOM (Fig. S10).

7.11. The genetic relationships of aqueous alteration, hydrothermal activity, and brecciation

The petrogenesis of the final Flensburg chondrite likely started with the accretion of water-rich ices intermixed with mineral dust, chondrules and mineral and lithic clasts including substantial amounts of Fe,Ni metal and Fe,Ni sulfides (Harries and Langenhorst, 2013; Singerling and Brearley, 2018). Subsequent and substantial heating after accretion led to aqueous (low-temperature) and hydrothermal (high-temperature, >100°C) alteration. This caused the progressive and total conversion of the primary ferromagnesian silicates to phyllosilicates and the dissolution of primary metal and Fe-rich sulfides. Only a few primary phases survived this stage, such as chromite grains and, possibly, pentlandite that appears to be more resistant to alteration than low-Ni Fe sulfides (Singerling and Brearley, 2020) and often occurs as clusters of fragmented or aligned grains in Flensburg. At the low-temperature stage, comparable to alteration observed in CM2 chondrites, much of the fine-grained, Fe-rich matrix serpentine may have formed. As
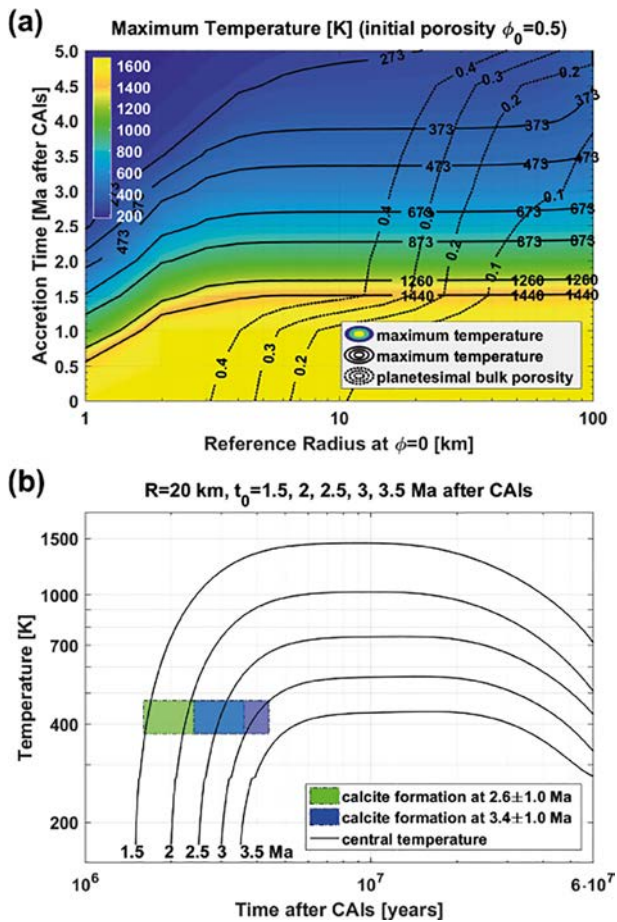
Fig. 27. (a) Maximum temperature and bulk porosity as functions of the accretion time and size of the parent body. A maximum temperature of 400°C is obtained for planetesimals with an accretion time of ~2.7 Ma after CAIs. The thermal evolution of these bodies is consistent with the Mn-Cr data. Bulk porosities of 30%, 20%, and 10% are obtained for radii of ~20 km, ~30 km, and ~60 km, respectively. (b) Thermal evolution of the Flensburg parent body at the center assuming accretion at 1.5, 2, 2.5, 3, and 3.5 Ma after CAIs, and a radius of 20 km. Calcite formation of 2.6 Ma or 3.4 Ma after CAIs can be fitted on prograde temperature evolution paths. High maximum temperatures obtained assuming accretion at 1.5 and 2 Ma after CAIs imply phyllosilicate dehydration or partial melting, contradicting Flensburg mineralogy. Maximum temperatures of 350–400°C (623-673 K) obtained in the Flensburg parent body assuming accretion at ~2.7 Ma after CAIs agree with mineralogical observations, and this accretion time is compatible with both calcite formation ages.

the temperature increased up to ~200°C (perhaps higher, see below) Fe- and S-rich hydrothermal fluids (possibly from the breakdown of tochilinite at ~120°C; Zolensky et al., 1997) led to the crystallization of magnetite and pyrrhotite. Some pyrrhotite crystals were sheathed by Mg-rich serpentine or enclosed by co-precipitating carbonates. The dolomite cores in many carbonate grains (calcites) further suggest elevated temperatures (Lee et al., 2014). The enhanced formation of pyrrhotite at the rims of chondrules and lithic clasts may have been due to high internal Fe concentrations from the alteration of metallic inclusions and

the slow release of Fe to the outside, where it reacted with S-bearing fluids transported through the more permeable meteorite matrix.

The primary heat sources besides enthalpy of hydration might have been internal radiogenic heat production and impact heating. Based on the early carbonate (and implicit pyrrhotite) formation (Fig. 14), radiogenic heating would have played a dominant role. It is assumed here that the impacts responsible for creating the fragments in Fig. 4 did not cause significant heating within the porous planetesimal, since no shock-features like chondrule flattening were observed within the chondritic clast (Fig. 4f and b). As fragment formation predates carbonate and pyrrhotite formation, it likely occurred by brecciation due to low velocity impacts during planetesimal growth.

Radiogenic heating by mainly ^{26}Al could have heated small bodies with a few tens of km radius to temperatures well in the range of >100°C if accretion occurred at about 3.5 Ma relative to CAIs (Fujiya et al., 2012; Bland and Travis, 2017). A more detailed calculation demonstrates that a thermal pulse triggering carbonate formation in a time interval prescribed by Mn-Cr dating (1.6–4.4 Ma after CAIs) requires a formation time at ca. 1.5–3.0 Ma after CAIs (see thermal evolution curves in Fig. 27, and model description in SM). This formation time – assuming a homogeneous ^{26}Al/^{27}Al ratio of 5.23×10^{-6} at the time of CAI formation – would inevitably lead to internal heating by ^{26}Al up to maximum temperatures of ca. 550–1500 K in a 40 km sized planetesimal (r = 20 km), depending on accretion time. As Flensburg did not experience significant thermal metamorphism as described for some CI and CM chondrites, we may consider 400°C as heating limit according to Tonui et al. (2014). This would be sufficient to trigger pyrrhotite and magnetite crystallization, but insufficient to lead to dehydration of serpentine, in agreement with mineralogical observations and pressure estimates. Flensburg started with a relatively low water/rock ratio as indicated by O isotope data, such that at >200°C most liquid water may have been used up by phyllosilicate formation and Fe oxidation. This probably stalled further hydrothermal processing, but preserved serpentine through peak temperatures by remaining high partial pressures of H_2O vapor.

Taking 400°C as the upper limit, Fig. 27 indicates that parent body formation occurred slightly later than 2.5 Ma after CAIs, followed by carbonate formation ca. 3 Ma after CAIs, which is in agreement with Mn-Cr dating, no matter if carbonate formation constraints of 3.4 ± 1.0 Ma after CAIs (with a CAI Pb-Pb age by Bouvier et al. (2011) or 2.6 ± 1.0 Ma after CAIs (using the Connelly et al. (2012) CAI age) are applied. Earlier carbonate formation can be excluded, as parent body temperatures up to 1500 K would be incompatible with the hydrated mineralogy of Flensburg. An exception could be very small bodies with a few km radius: these could escape severe heating; however, they would keep a very high porosity, again incompatible with Flensburg's porosity. There remains another – more speculative – possibility that could reconcile both early formation and lack of too severe heating effects which is a lower than canonical ^{26}Al/^{27}Al ratio in the formation region of the Flensburg parent body. This would imply a heterogeneous

distribution of ^{26}Al (or of the short-lived nuclide ^{53}Mn used here for dating) in the solar nebula.

In summary, the optimum parent body model with 400°C maximum temperature and 10–20% porosity prescribes 20–30 km radius, and a formation time of 2.5 Ma after CAIs, implying carbonate formation ca. 3 Ma after CAIs.

Clearly, shock processing has also played a role in the history of Flensburg; however, the degree of shock metamorphism is uncertain, since typical shock effects in mafic silicates (olivine, pyroxenes) and plagioclase, which are considered to be excellent indicators of shock metamorphism (Stöffler et al., 1991; Scott et al., 1992; Bischoff and Stöffler, 1992; Bischoff et al., 2019a) do not exist anymore within this strongly, aqueously-altered chondrite. Strong arguments for early shock processes are given by the occurrence of lithic clasts (Fig. 4e and f). The shape, mineralogy, and the boundary of the magnetite-rich object in Fig. 4e clearly indicate that it did not form in-situ.

The most convincing argument for an early brecciation comes from one of the largest objects in Flensburg having an internal chondritic texture (Fig. 4f). This object can clearly be considered as an independent clast, since its texture is completely different from the texture of the bulk rock. As shown in Fig. 4f, the fragment has a well-preserved chondritic texture. The phases surrounding this clast and similar objects include abundant sulfide laths (light grey coronas in the CT-cross sections of Fig. 3a and b) and carbonates.

The most considerable explanation for the formation of this clast is that the object (of course without the sulfide-rich zone) formed by soft impact brecciation and that the resulting clast was mixed with (altered) chondrules and matrix components (like phyllosilicates) within the (still fluid-rich) parent body. As documented by the sulfides, the temperature of their formation was high (definitely >100°C). As shown in Figs. 5 and 14, carbonate precipitation must be contemporaneous with hydrothermal pyrrhotite formation within 3.4 Ma after CAIs. If the clasts originated from the same parent body, only very soft impact activity is considered since the fragment did not escape from the parent body. Alternatively, this clast and probably similar ones represent a chondritic lithology from an impacted and (partly) destroyed, independent parent body and can be considered as (a) projectile(s) softly added to the "Flensburg planetesimal".

In any case, the clast shown in Fig. 4f suffered a second episode of aqueous alteration. The collision-induced fragmentation and re-accretion of the components resulted in a loosely-compacted, brecciated parent body with high porosity and significant pore space especially between larger objects. Thus, this pore space enabled the formation of the completely circumferential zone of sulfides (Fig. 4f; often intergrown with carbonates) at elevated fS_2 (from breakdown of tochilinite or primarily H_2S-rich fluids). It is suggested that many other large objects (e.g., chondrules; Fig. 4a–d) received similar sulfide-rich areas at the same time as the chondritic clast (Fig. 4f). This kind of breccia formation is certainly different to processes in the formation history of typical CM breccias as recently discussed (e.g., Metzler et al., 1992; Bischoff et al., 2006, 2017b; Lindgren

et al., 2013; Zolensky et al., 2017; Lentfort et al., 2019, 2020).

7.12. The diversity of (water-bearing) parent bodies and lithologies in the early Solar System

The primordial planetesimal disk likely consisted of thousands to millions of independent primary planetesimals that formed within the first few Ma of the solar system and have been altered and modified by thermal and aqueous processes and impact activities. Many have probably been destroyed by impact, delivered precursor materials for consecutive second generation parent bodies or materials that accreted together with chondrules, forming new parent bodies. In this respect, the CR chondrites that accreted C1-like components, are an excellent example. Since the CR chondrite parent body(ies) formed late (~4 Ma after CAIs; e.g., Budde et al., 2018), sufficient time was available to form the C1-like "dark inclusions" (e.g., Endress et al., 1994; Patzek et al., 2018a) by aqueous alteration processes on water-rich precursor planetesimals possibly at similar heliocentric distances based on similar D enrichments, that were later fragmented (Patzek et al., 2020). Subsequently, clasts were transported, mixed, and accreted with components (chondrules, metals) formed under completely different (reducing) conditions to form the CR planetesimal(s). It is often considered that specific groups of chondrites derive from only one "primordial" asteroid as it existed in the first tens of Ma of solar system history (e.g., "the H chondrite parent body"; "the CM chondrite parent body"; e.g., Trieloff et al., 2003; Blackburn et al., 2017) and that fragmentation and re-assembly occurred later. Since ~1,000,000 asteroids in the main belt with sizes >1 km exist, Burbine et al. (2002) point out that no direct evidence rules out multiple primordial chondritic asteroids of essentially identical material. In detail, for the ordinary chondrites, Vernazza et al. (2014) argued that large groups of compositionally similar asteroids are a natural outcome of planetesimal formation.

On the other hand, the impact-related formation of several generations of planetary bodies is evident and has been discussed earlier mostly for "water-free" rocks (e.g., Urey, 1959, 1967; Zook, 1980; Hutchison et al., 1988; Hutchison, 1996; Sanders, 1996; Bischoff, 1998; Zolensky and Ivanov, 2003 Bischoff and Schultz, 2004; Bischoff et al., 2006, 2010, 2019b; Sokol et al., 2007a,b; Horstmann et al., 2014a; Goodrich et al., 2014; Horstmann and Bischoff, 2014; Weyrauch et al., 2018). To explain certain mineralogical and textural features in CR, CM, CI, and similar chondrites, the necessity of the occurrence of precursor planetesimals has been previously proposed (e.g., Metzler et al., 1992; Weisberg et al., 1993; Bischoff, 1998; Bischoff et al., 2006, 2018a, 2018b; Patzek et al., 2019a,b, 2020; Greenwood et al., 2020).

This should also be the case for CM chondrites and many chondrites having similar mineralogical characteristics (e.g., abundant phyllosilicates). It is completely unclear, whether all the different rocks represent a single parent body. It is even not clear, if the very different clasts in CM chondrites represent different lithologies of a single

parent body or whether the brecciated CM chondrites are formed by re-accretion of fragments that originally formed on primordial or first-generation precursor planetesimals (CM2.0-CM6; e.g., Kerraouch et al., 2019, 2020; Lentfort et al., 2020).

Bischoff et al. (2006) report abundant evidence from meteoritic breccias that early-formed asteroids were rapidly destroyed and resulting fragments were incorporated into the second generation "daughter" bodies as confirmed by several recent studies (e.g., Bonal et al., 2010; Lindgren et al., 2013; Bischoff et al., 2018a, 2018b; Patzek et al., 2018a, 2020; Greenwood et al., 2020). The concept of the existence and evolution of primary vs. secondary parent bodies is also discussed by Greenwood et al. (2020). They suggest that this relationship has important implications for early Solar System evolution, since chondritic parent bodies are known to have accreted between 1 and 4 Ma after CAIs. This difference in time may reflect the fact that their source asteroids, particularly those of the carbonaceous chondrites, are secondary bodies, with the original CAI-bearing primary bodies destroyed during early collisional processing (Greenwood et al., 2020).

As also well summarized by Greenwood et al. (2020), dark inclusions in carbonaceous chondrites preserve evidence of complex evolutionary processes. These clasts preserve information about the aqueous alteration that took place prior to incorporation within the final host parent body (e.g., Bischoff et al., 2006, 2018a; Sokol et al., 2007a,b; Bonal et al., 2010; Patzek et al., 2018a). Bischoff et al. (2006, 2018a) and Patzek et al. (2018a) suggested that the evidence from meteoritic breccias and dark inclusions is consistent with the formation and destruction of multiple generations of precursor asteroids prior to the accretion of the final parent body. Patzek et al. (2018a) suggest that the volatile-rich clasts in CR, CH, and (perhaps) in H chondrites represent components of primary accretion and not pieces of projectiles that impacted the host parent bodies much later. Bonal et al. (2010) come to a very similar conclusion after studying different aqueously altered clasts in Isheyevo: The characteristics of the clasts do not match those of any of these aqueously altered meteorite classes, nor do they match those of similar material in various types of chondritic clasts present in other meteorite groups. The Isheyevo clasts are considered as being fragments of previously unsampled parent bodies (Bonal et al., 2010).

Considering the aqueously-altered matter in carbonaceous chondrites, the formation of these rocks and the evolution of their parent bodies is even more complex. Clear evidence exists that the phyllosilicates in the dust-rims surrounding chondrules and the TCI formation must result from alteration processes prior to accretion onto the chondrules and chondrite accretion (Metzler et al., 1992; Bischoff, 1998). This early episode is illustrated in Fig. 19 of Metzler et al. (1992). After accretion of CM parent bodies, collisions between similar and/or with different planetesimals played a fundamental role in the evolution of the CM parent bodies. By far, most CM chondrites are breccias that consist of lithic clasts with different alteration stages (Metzler et al., 1992; Lindgren et al., 2013; Bischoff et al., 2017b; Kerraouch et al., 2019, 2020; Lentfort et al.,

2020) mixed together in the same breccia. The observation that all lithic clasts still show their original accretionary texture (see also Fig. 24b and c) indicate that a single starting material was affected by liquid water under different alteration conditions, followed by impact brecciation and mixing.

Greenwood et al. (2019) suggested the possibility that "the CM parent body" is more isotopically heterogeneous than previously thought or, alternatively, that CM-related material is present on multiple bodies and formed from similar starting materials and then experienced variable degrees of hydrothermal processing. They also concluded that CMs and COs – except for the O isotopes – show a range of textural and geochemical similarities and, perhaps, a close genetic relationship. The main difference relates to the amount of water that would have been accreted to the parent bodies of the two groups (Chaumard et al., 2018), with COs being essentially dry and CMs having experienced significant aqueous alteration (Clayton and Mayeda, 1999). Greenwood et al. (2019) interestingly noticed that the CO-CM oxygen isotope "gap" is effectively filled by a significant number of CM and C2-like chondrites which show transitional features between CO and CM chondrites (e.g., EET 87522, GRO 95566, LEW 85311, MAC 87300, MAC 88107, NWA 7821, NWA 11556, Y-82054, NWA 5958, NWA 7821 and NWA 11556, Adelaide, and ALH 77307).

Flensburg is presenting another case. Concerning the low number of different meteorite groups and the present-day existence of ~1,000,000 asteroids in the main belt >1 km, which are most likely fragments of once larger planetesimals, it is suggested that many more CM and ungrouped C1 or C2 chondrite parent bodies exist than typically considered. CM-related material should have been present on many different parent bodies, which may have formed from similar starting materials and evolved in a similar environment as indicated by similar, but not identical mineralogy and isotopic characteristics.

7.13. Final aspects

7.13.1. Flensburg as an analogue for asteroidal samples returned by the OSIRIS-REx and Hayabusa 2 missions

In general, the rocks heavily affected by aqueous alteration (e.g., CI and CM chondrites) are highly-brecciated (e.g., Metzler et al., 1992; Morlok et al., 2006; Bischoff et al., 2006, 2017b; Lindgren et al., 2013; Zolensky et al., 2015, 2017; Alfing et al., 2019; Lentfort et al., 2020). All these rocks and breccias provide insight into the formation processes of their parent bodies as well as into the evolution of asteroid surfaces. Considering the current NASA and JAXA missions to the asteroids (101955) Bennu and (162173) Ryugu, respectively, the work on the strongly aqueously-altered Flensburg chondrite may help to decipher distinct features on Bennu and Ryugu that can be studied after the sample return. Both asteroids are regarded as consisting of materials affected by aqueous alteration (e.g., Hamilton et al., 2019; Kitazato et al., 2019). Ryugu is described as having a very low density and an estimated high porosity of >50% in its interior (Watanabe et al., 2019). A very low density of <2 g/cm^3 is also observed

for Flensburg. Considering asteroid Bennu, early spectral data of OSIRIS-REx show evidence for abundant hydrated minerals on the surface as demonstrated by the absorption feature at ~2.7 μm (Hamilton et al., 2019) indicating similarities to aqueously-altered carbonaceous chondrites. In addition, Bennu also has a low density, which is consistent with a high porosity and particle density characteristic of CM chondrites (Lauretta et al., 2019, McCoy et al., 2019) and perhaps the Flensburg carbonaceous chondrite. In summary, the mineralogical, textural, and chemical work on CM and CI breccias will certainly help to evaluate and understand the returned samples from the OSIRIS-REx and Hayabusa 2 missions.

7.13.2. Flensburg and the meteorite fall statistics in Central Europe

Considering the meteorite falls of Braunschweig (L6; Bartoschewitz et al., 2017), Žd'ár nad Sázavou (L3; Spurný, 2016; Spurný et al., 2016), Ejby (H5/6; Spurný et al., 2017; Haack et al., 2019), Stubenberg (LL6; Ebert and Bischoff, 2016; Spurný et al., 2016; Bischoff et al., 2017a), Hradec Králové (LL5; 2016; The Meteoritical Bulletin), Broek in Waterland (L6, 2017; The Meteoritical Bulletin), and Renchen (L5-6; Bischoff et al., 2019b), Flensburg is the eighth recovered meteorite fall since 2013 impacting on Earth in an area less than 500 km in radius. As estimated from meteorite entries within the Database (The Meteoritical Bulletin), on average, less than ten meteorite falls are recovered globally per year. Hence, this number of recorded falls in Central Europe is remarkable. Although the Flensburg meteorite was found accidentally one day after the fireball event, the high concentration of recorded falls partly demonstrates the great success of the European Fireball Network and crowd sourcing initiatives of the IMO and AMS in recording fireball events and calculating possible meteorite strewn fields. This led to ultimately finding the respective/associated meteorites by well-informed amateurs and scientists.

8. CONCLUSIONS

Flensburg is a phyllosilicate-rich rock that does not contain any olivine and pyroxenes and is classified here as a unique type 1 carbonaceous chondrite. The rock consists of relict chondrules, clusters of sulfide and magnetite grains, and carbonates (often intergrown with sulfides) set in a fine-grained matrix.

In particular, based on its bulk H, C, and N elemental abundances and isotopic compositions, Flensburg is clearly unique among previously analyzed chondrites as it has the lightest bulk H and N isotopic compositions of any type 1 or 2 chondrite. The bulk O isotope composition of Flensburg reveals that it plots at the ^{16}O-rich end of the CM chondrite field and in the transition field to the CV-CK-CR chondrites. Normally this is the area, where most of the least altered type 2 chondrites plot.

Mineralogical observations demonstrate that there was brecciation and contemporaneous formation of the pyrrhotite-carbonate intergrowths. The ^{53}Mn-^{53}Cr ages of carbonates in Flensburg indicate that their formation happened no later than 4564.6 ± 1.0 Ma (using D'Orbigny as the Mn-Cr anchor). This corresponds to 2.6 ± 1.0 or 3.4 ± 1.0 Ma after CAIs, depending on the exact CAI age assumed, representing the oldest carbonates measured in any chondrite. This result indicates that aqueous activity occurred very early in the solar system and that the primary parent body must have been very small in order to retain water-bearing phases and escape dehydration based on heating from the decay of ^{26}Al.

In summary, the extraordinary significance of Flensburg is given by the observation that it represents the oldest chondrite sample, in which the contemporaneous episodes of aqueous alteration and brecciation from the time of the growth of the parent body by low velocity collisions are perfectly visible. The Flensburg meteorite is evidence for the existence of small water-rich parent bodies in the early solar system and might be similar to planetesimals that delivered (as building blocks) water to Earth.

Declaration of Competing Interest

The authors declare that they have no known competing financial interests or personal relationships that could have appeared to influence the work reported in this paper.

APPENDIX A. SUPPLEMENTARY MATERIAL

Supplementary data to this article can be found online at https://doi.org/10.1016/j.gca.2020.10.014.

REFERENCES

Alexander C. M. O'D. (2019) Quantitative models for the elemental and isotopic fractionations in chondrites: The carbonaceous chondrites. *Geochim. Cosmochim. Acta* **254**, 277–309.

Alexander C. M. O'D., Fogel M., Yabuta H. and Cody G. D. (2007) The origin and evolution of chondrites recorded in the elemental and isotopic compositions of their macromolecular organic matter. *Geochim. Cosmochim. Acta* **71**, 4380–4403.

Alexander C. M. O'D., Bowden R., Fogel M. L., Howard K. T., Herd C. D. K. and Nittler L. R. (2012) The provenances of asteroids, and their contributions to the volatile inventories of the terrestrial planets. *Science* **337**, 721–723.

Alexander C. M. O'D., Howard K., Bowden R. and Fogel M. L. (2013) The classification of CM and CR chondrites using bulk H, C and N abundances and isotopic compositions. *Geochim. Cosmochim. Acta* **123**, 244–260.

Alexander C. M. O'D., Bowden R., Fogel M. L. and Howard K. T. (2015) Carbonate abundances and isotopic compositions in chondrites. *Meteor. Planet. Sci.* **50**, 810–833.

Alexeev V. (2003) Meteorite ablation evaluated from data on the distribution of cosmogenic neon isotopes. *Sol. Syst. Res.* **37**(3), 207–217.

Alfing J., Patzek M. and Bischoff A. (2019) Modal abundances of coarse-grained (>5 μm) components within CI-chondrites and their individual clasts – mixing of various lithologies on the CI parent body(ies). *Geochemistry – Chem. Erde* **79** 125532.

Amari S., Lewis R. S. and Anders E. (1995) Interstellar grains in meteorites: III. Graphite and its noble gases. *Geochim. Cosmochim. Acta* **59**(7), 1411–1426.

Amelin Y., Kaltenbach A., Iizuka T., Stirling C. H., Ireland T. R., Petaev M. and Jacobsen S. B. (2010) U-Pb chronology of the Solar System's oldest solids with variable ^{238}U/^{235}U. *Earth Planet. Sci. Lett.* **300**, 343–350.

Aponte J. C., Alexandre M. R., Wang Y., Brearley A. J., Alexander C. M. O'D. and Huang Y. (2011) Effects of secondary alteration on the composition of free and IOM-derived monocarboxylic acids in carbonaceous chondrites. *Geochim. Cosmochim. Acta* **75**, 2309–2323.

Barrat J.-A., Zanda B., Moynier F., Bollinger C., Liorzou C. and Bayron G. (2012) Geochemistry of CI chondrites: Major and trace elements, and Cu and Zn isotopes. *Geochim. Cosmochim. Acta* **83**, 79–92.

Barrat J.-A., Rouxel O., Wang K., Moynier F., Yamaguchi A., Bischoff A. and Langlade J. (2015) Early stages of core segregation recorded by Fe isotopes in an asteroidal mantle. *Earth Planet. Sci. Lett.* **419**, 93–100.

Barrat J.-A., Gillet P., Dauphas N., Bollinger C., Etoubleau J., Bischoff A. and Yamaguchi A. (2016) Evidence from Tm anomalies for non-CI refractory lithophile element proportions in terrestrial planets and achondrites. *Geochim. Cosmochim. Acta* **176**, 1–17.

Bates H. C., King A. J., Donaldson Hanna K. L., Bowles N. E. and Russell S. S. (2020) Linking mineralogy and spectroscopy of highly aqueously altered CM and CI carbonaceous chondrites in preparation for primitive asteroid sample return. *Meteorit. Planet. Sci.* **55**, 77–101.

Bartoschewitz R., Appel P., Barrat J.-A., Bischoff A., Caffee M. W., Franchi I. A., Gabelica Z., Greenwood R. C., Harir M., Harries D., Hochleitner R., Hopp J., Laubenstein M., Mader B., Marques R., Morlok A., Nolze G., Prudêncio M. I., Rochette P., Ruf A., Schmitt-Kopplin Ph., Seemann E., Szurgot M., Tagle R., Wach R. A., Welten K. C., Weyrauch M. and Wimmer K. (2017) The Braunschweig meteorite – a recent L6 chondrite fall in Germany. *Chemie der Erde – Geochemistry* **77**, 207–224.

Beck P., Quirico E., Montes-Hernandez G., Bonal L., Bollard J., Orthous-Daunay F.-R., Howard K. T., Schmitt B., Brissaud O., Deschamps F., Wunder B. and Guillot S. (2010) Hydrous mineralogy of CM and CI chondrites from infrared spectroscopy and their relationship with low albedo asteroids. *Geochim. Cosmochim. Acta* **74**, 4881–4892.

Beck P., Maturilli A., Garenne A., Vernazza P., Helbert J., Quirico E. and Schmitt B. (2018) What is controlling the reflectance spectra (0.35–150 μm) of hydrated (and dehydrated) carbonaceous chondrites? *Icarus* **313**, 124–138.

Bertini I., Luchinat C., Parigi G. and Pierattelli R. (2005) NMR Spectroscopy of Parmagentic metalloproteins. *ChemBioChem* **6**, 1536–1549.

Bischoff A. (1998) Aqueous alteration of carbonaceous chondrites: Evidence for preaccretionary alteration – a review. *Meteorit. Planet. Sci.* **33**, 1113–1122.

Bischoff A. and Schultz L. (2004) Abundance and meaning of regolith breccias among meteorites. *Meteorit. Planet. Sci.* **39**, A15.

Bischoff A. and Stöffler D. (1992) Shock metamorphism as a fundamental process in the evolution of planetary bodies: Information from meteorites. *Eur. J. Mineral.* **4**, 707–755.

Bischoff A., Scott E. R. D., Metzler K. and Goodrich C. A. (2006) Nature and Origins of meteoritic breccias. In *Meteorites and the Early Solar System II* (eds. D. S. Lauretta and H. Y. McSween). Univ. of Arizona, Tucson, pp. 679–712.

Bischoff A., Horstmann M., Pack A., Laubenstein M. and Haberer S. (2010) Asteroid 2008 TC$_3$ - Almahata Sitta: a spectacular breccia containing many different ureilitic and chondritic lithologies. *Meteorit. Planet. Sci.* **45**, 1638–1656.

Bischoff A., Barrat J.-A., Bauer K., Burkhardt C., Busemann H., Ebert S., Gonsior M., Hakenmüller J., Haloda J., Harries D., Heinlein D., Hiesinger H., Hochleitner R., Hoffmann V., Kaliwoda M., Laubenstein M., Maden C., Meier M. M. M., Morlok A., Pack A., Ruf A., Schmitt-Kopplin P., Schönbächler M., Steele R. C. J., Spurny P. and Wimmer K. (2017a) The Stubenberg meteorite - an LL6 chondrite fragmental breccia recovered soon after precise prediction of the strewn field. *Meteorit. Planet. Sci.* **52**, 1683–1703.

Bischoff A., Ebert S., Metzler K. and Lentfort S. (2017b) Breccia classification of CM chondrites. *Meteorit. Planet. Sci.* **52** (Special Issue). A26, #6089.

Bischoff A., Patzek M., Ebert S., Pack A., Kerraouch I. and Zolensky M. E. (2018a) A large, light fragment in the Murchison (CM) breccia – a unique, highly-metamorphosed

chondrite as a xenolith in a CM chondrite (abstract #6217). *Meteorit. Planet. Sci.* **53**, 6217.

Bischoff A., Schleiting M., Wieler R. and Patzek M. (2018b) Brecciation among 2280 ordinary chondrites – constraints on the evolution of their parent bodies. *Geochim. Cosmochim. Acta* **238**, 516–541.

Bischoff A., Schleiting M. and Patzek M. (2019a) Shock stage distribution of 2280 ordinary chondrites – Can bulk chondrites with a shock stage S6 exist as individual rocks? *Meteorit. Planet. Sci.* **54**, 2189–2202.

Bischoff A., Barrat J.-A., Berndt J., Borovicka J., Burkhardt C., Busemann H., Hakenmüller J., Heinlein D., Hertzog J., Kaiser J., Maden C., Meier M. M. M., Morino P., Pack A., Patzek M., Reitze M. P., Rüfenacht M., Schmitt-Kopplin P., Schönbächler M., Spurny P., Weber I., Wimmer K. and Zikmund T. (2019b) The Renchen L5–6 chondrite breccia – the first confirmed meteorite fall from Baden-Württemberg (Germany). *Geochemistry – Chem. Erde* **79** 125525.

Bjärnborg K. and Schmitz B. (2013) Large spinel grains in a CM chondrite (Acfer 331): implications for reconstructions of ancient meteorite fluxes. *Meteorit. Planet. Sci.* **48**, 180–194.

Blackburn T., Alexander C. M. O'D., Carlson R. and Elkins-Tanton L. T. (2017) The accretion and impact history of the ordinary chondrite parent bodies. *Geochim. Cosmochim. Acta* **200**, 201–217.

Bland P. A. and Travis B. J. (2017) Giant convecting mud balls of the early solar system. *Sci. Adv.* **3** e1602514.

Bonal L., Huss G. R., Krot A. N. and Nagashima K. (2010) Chondritic lithic clasts in the CB/CH-like meteorite Isheyevo: fragments of previously unsampled parent bodies. *Geochim. Cosmochim. Acta* **74**, 2500–2522.

Botta O., Martins Z. and Ehrenfreund P. (2007) Amino acids in Antarctic CM1 meteorites and their relationship to other carbonaceous chondrites. *Meteorit. Planet. Sci.* **42**, 81–92.

Bouvier A., Brennecka G. A., and Wadhwa A. (2011) Absolute chronology of the first solids in the solar system. Workshop on the formation of the first solids in the solar system, Kauai, #9054 (abstr.).

Braukmüller N., Wombacher F., Hezel D. C., Escoube R. and Münker C. (2018) The chemical composition of carbonaceous chondrites: Implications for volatile element depletion, complementarity and alteration. *Geochim. Cosmochim. Acta* **239**, 17–48.

Brearley A. J. (2006) The action of water. In *Meteorites and the Early Solar System II* (eds. D. S. Lauretta and H. Y. McSween). The University of Arizona Press, Tucson, Arizona, pp. 587–624.

Brecher A. and Arrhenius G. (1974) The paleomagnetic record in carbonaceous chondrites: natural remanence and magnetic properties. *J. Geophys. Res.* **79**, 2081–2106.

Brennecka G. A. and Wadhwa M. (2012) U isotope compositions of the basaltic angrite meteorites and the chronological implications for the early Solar System. *Proc. Natl. Acad. Sci.* **109**, 9299–9303.

Brown R. M., Andrews H. R., Ball G. C., Burn N., Imahori Y., Milton J. C. D. and Fireman E. L. (1984) ^{14}C content of ten meteorites measured by tandem accelerator mass spectrometry. *Earth Planet. Sci. Lett.* **67**, 1–8.

Browning L. B., McSween, Jr., H. Y. and Zolensky M. E. (1996) Correlated alteration effects in CM carbonaceous chondrites. *Geochim. Cosmochim. Acta* **60**, 2621–2633.

Bryson J. F. J., Weiss B. P., Lima E. A., Gattacceca J. and Cassata W. (2020) Evidence for planetary migrations and distal solar system solids from meteorite paleomagnetism. *Astrophys. J.* **892** (2), 126.

Budde G., Kruijer T. S. and Kleine T. (2018) Hf-W chronology of CR chondrites: Implications for the timescales of chondrule formation and the distribution of [26]Al in the solar nebula. *Geochim. Cosmochim. Acta* **222**, 284–304.

Burbine T. H., McCoy T. J., Meibom A., Gladman B. and Keil K. (2002) Meteoritic parent bodies: their number and identification. In *Asteroids III* (eds. W. Bottke, A. Cellino, P. Paolicchoi and R. P. Binzel). University of Arizona Press, Tucson, pp. 653–667.

Burkhardt C., Dauphas N., Tang H., Fischer-Gödde M., Qin L., Chen J. H., Rout S. S., Pack A., Heck P. R. and Papanastassiou D. A. (2017) In search of the Earth-forming reservoir: mineralogical, chemical, and isotopic characterizations of the ungrouped achondrite NWA 5363/NWA 5400 and selected chondrites. *Meteorit. Planet. Sci.* **52**, 807–826.

Burkhardt C., Dauphas N., Hans U., Bourdon B. and Kleine T. (2019) Elemental and isotopic variability in solar system materials by mixing and processing of primordial disk reservoirs. *Geochim. Cosmochim. Acta* **261**, 145–170.

Busemann H., Baur H. and Wieler R. (2000) Primordial noble gases in "phase Q" in carbonaceous and ordinary chondrites studied by closed-system stepped etching. *Meteorit. Planet. Sci.* **35**, 949–973.

Calvin W. M. (1999) "ICES" throughout the solar system: aatour of condensable species. *Planet. Report* **19**(2), 8–13.

Chaumard N., Defouilloy C. and Kita N. T. (2018) Oxygen isotope systematics of chondrules in the Murchison CM2 chondrite and implications for the CO-CM relationship. *Geochim. Cosmochim. Acta* **228**, 220–242.

Clayton R. N. (2002) Self-shielding in the solar nebula. *Nature* **54**, 349–392.

Clayton R. N. (2008) Oxygen isotopes in the early Solar System – a historical perspective. In *Oxygen in the Solar System*, vol. 68 (ed. MacPherson). American Mineralogical Society, Washington, pp. 5–14.

Clayton R. N. and Mayeda T. K. (1984) The oxygen isotope record in Murchison and other carbonaceous chondrites. *Earth Planet. Sci. Lett.* **67**, 151–161.

Clayton R. N. and Mayeda T. K. (1999) Oxygen isotope studies of carbonaceous chondrites. *Geochim. Cosmochim. Acta* **63**(13–14), 2089–2104.

Clayton R. N., Onuma N. and Mayeda T. K. (1976) A classification of meteorites based on oxygen isotopes. *Earth Planet. Sci. Lett.* **30**, 10–18.

Connelly J. N., Bizzarro M., Krot A. N., Nordlund A., Wielandt D. and Ivanova M. A. (2012) The absolute chronology and thermal processing of solids in the solar protoplanetary disc. *Science* **338**, 651–655.

Cournède C., Gattacceca J., Gounelle M., Rochette P., Weiss B. P. and Zanda B. (2015) An early solar system magnetic field recorded in CM chondrites. *Earth Planet. Sci. Lett.* **410**, 62–74.

Derenne S., Coelho C., Anquetil C., Szopa C., Rahman A. S., McMillan P. F., Corà F., Pickard C. J., Quirinico E. and Bonhomme C. (2012) New insights into the structure and chemistry of Titan´s tholins via ^{13}C and ^{15}N solid state magnetic resonance spectroscopy. *Icarus* **221**, 844–853.

DDEP (Decay Data Evaluation Project) website (2020) http://www.nucleide.org/Laraweb/index.php.

Donohue P. H., Huss G. R., and Nagashima K. (2019) New Synthetic Carbonates for Investigation of Manganese-Chromium Chronology by Secondary Ion Mass Spectrometry. Lunar and Planetary Science Conference 50, #1959.

Eiler J. M. and Kitchen N. (2004) Hydrogen isotope evidence for the origin and evolution of the carbonaceous chondrites. *Geochim. Cosmochim. Acta* **68**, 1395–1411.

Endress M. and Bischoff A. (1993) Mineralogy, degree of brecciation, and aqueous alteration of CI chondrites Orgueil, Ivuna, and Alais (abstract). *Meteoritics* **28**, 345–346.

Endress M., Keil K., Bischoff A., Spettel B., Clayton R. N. and Mayeda T. K. (1994) Origin of dark clasts in the Acfer 059/El Djouf 001 CR2 chondrite. *Meteoritics* **29**, 26–40.

Findlay R., Greenwood R. C., King A.J., Anand M., and Franchi I. A. (2020) Two recent CM falls: New evidence for a lithologically and isotopically heterogeneous CM parent body. Lunar and Planetary Science Conference 51, Abstract #2880.

Folco L., Rochette P., Gattacceca J. and Perchiazzi N. (2006) In situ identification, pairing and classification of meteorites from Antarctica through magnetic susceptibility measurements. *Meteorit. Planet. Sci.* **41**, 343–353.

Fredriksson K. and Kerridge J. F. (1988) Carbonates and sulfates in CI chondrites: Formation by aqueous activity on the parent body. *Meteoritics* **23**, 35–44.

Fuchs L. H., Olsen E. and Jensen K. J. (1973) Mineralogy, mineral-chemistry, and composition of the Murchison (C2) meteorite. *Smithsonian Contributions to the Earth Science* **10**, 1–39.

Fujiya W., Sugiura N., Hotta H., Ichimura K. and Sano Y. (2012) Evidence for the late formation of hydrous asteroids from young meteoritic carbonates. *Nature Commun.* **3**, 627.

Fujiya W., Sugiura N., Sano Y. and Hiyagon H. (2013) Mn–Cr ages of dolomites in CI chondrites and the Tagish Lake ungrouped carbonaceous chondrite. *Earth Planet. Sci. Lett.* **362**, 130–142.

Garenne A., Beck P., Montes-Hernandez G., Chiriac R., Toche F., Quirico E., Bonal L. and Schmitt B. (2014) The abundance and stability of "water" in type 1 and 2 carbonaceous chondrites (CI, CM and CR). *Geochim. Cosmochim. Acta* **137**, 93–112.

Garvie L. A. J., Zega T. J., Rez P. and Buseck P. R. (2004) Nanometer-scale measurements of Fe3+/ΣFe by electron energy-loss spectroscopy: a cautionary note. *Am. Mineral.* **89**, 1610–1616.

Gattacceca J. and Rochette P. (2004) Toward a robust normalized magnetic paleointensity method applied to meteorites. *Earth Planet. Sci. Lett.* **227**, 377–393.

Gerber S., Burkhardt C., Budde G., Metzler K. and Kleine T. (2017) Mixing and transport of dust in the early solar nebula as inferred from titanium isotope variations among chondrules. *Astrophys. J.* **841**, L17.

Glavin D. P., Callahan M. P., Dworkin J. P. and Elsila J. E. (2011) The effects of parent body processes on amino acids in carbonaceous chondrites. *Meteorit. Planet. Sci.* **45**, 1948–1972.

Göpel C. and Birck J. L. (2010) Mn/Cr systematics: A tool to discriminate the origin of primitive meteorites. In Goldschmidt Conference abstracts, 348.

Göpel C., Birck J.-L., Galy A., Barrat J.-A. and Zanda B. (2015) Mn–Cr systematics in primitive meteorites: Insights from mineral separation and partial dissolution. *Geochim. Cosmochim. Acta* **156**, 1–24.

Gonsior M., Zwartjes M., Cooper W. J., Song W., Ishida K. P., Tseng L. Y., Jeung M. K., Rosso D., Hertkorn N. and Schmitt-Kopplin P. (2011) Molecular characterization of effluent organic matter identified by ultrahigh resolution mass spectrometry. *Water Res.* **45**, 2943–2953.

Goodrich C. A., Bischoff A. and O'Brien D. P. (2014) Asteroid 2008 TC$_3$ and the fall of Almahata Sitta, a unique meteorite breccia. *Elements* **10**, 31–37.

Goodrich C. A., Kita N. T., Yin Q.-Z., Sanborn M. E., Williams C. D., Nakashima D., Lane M. D. and Boyle S. (2017) Petrogenesis and provenance of ungrouped achondrite Northwest Africa 7325 from petrology, trace elements, oxygen, chromium and titanium isotopes, and mid-IR spectroscopy. *Geochim. Cosmochim. Acta* **203**, 381–403.

Gounelle M., Engrand C., Alard O., Bland P. A., Zolensky M. E., Russell S. S. and Duprat J. (2005) Hydrogen isotopic composition of water from fossil micrometeorites in howardites. *Geochim. Cosmochim. Acta* **69**, 3431–3443.

Grady M. M., Verchovsky A. B., Franchi I. A., Wright I. P. and Pillinger C. T. (2002) Light element geochemistry of the Tagish Lake CI2 chondrite: Comparison with CI1 and CM2 meteorites. *Meteor. Planet. Sci.* **37**, 713–735.

Grady M. M., Wright I. P., Swart P. K. and Pillinger C. T. (1988) The carbon and oxygen isotopic composition of meteoritic carbonates. *Geochim. Cosmochim. Acta* **52**, 2855–2866.

Green D. and Schodlok M. (2016) Characterisation of carbonate minerals from hyperspectral TIR scanning using features at 14 000 and 11 300 nm. *Aust. J. Earth Sci.* **63**, 951–957.

Greenwood R. C., Howard K. T., King A. J., Lee M. R., Burbine T. H., Franchi I. A., Anand M., Findlay R., and Gibson J. M. (2019) Oxygen isotope evidence for multiple CM parent bodies: What will we learn from the Hayabusa 2 and OSIRIS-REx sample return missions? Lunar and Planetary Science Conference 50, (abstract #3191).

Greenwood R. C., Burbine T. H. and Franchi I. A. (2020) Linking asteroids and meteorites to the primordial planetesimal population. *Geochim. Cosmochim. Acta* **277**, 377–406.

Grimm R. E. and McSween, Jr., H. Y. (1989) Water and the thermal evolution of carbonaceous chondrite parent bodies. *Icarus* **82**, 244–280.

Guo W. and Eiler J. M. (2007) Temperatures of aqueous alteration and evidence for methane generation on the parent bodies of the CM chondrites. *Geochim. Cosmochim. Acta* **71**, 5565–5575.

Haack H., Sørensen A. N., Bischoff A., Patzek M., Barrat J.-A., Midtskoge S., Stempel E., Laubenstein M., Greenwood R., Schmitt-Kopplin P., Busemann H., Maden C., Bauer K., Schönbächler M. and Dahl-Jensen T. (2019) Ejby - a new H5/6 ordinary chondrite fall in Copenhagen, Denmark. *Meteorit. Planet. Sci.* **54**, 1853–1869.

Hamilton V. E., Simon A. A., Christensen P. R., Reuter D. C., Clark B. E., Barucci M. A., Bowles N. E., Boynton W. V., Brucato J. R., Cloutis E. A., Connolly H. C., Donaldson Hanna K. L., Emery J. P., Enos H. L., Fornasier S., Haberle C. W., Hanna R. D., Howell E. S., Kaplan H. H., Keller L. P., Lantz C., Li J.-Y., Lim L. F., McCoy T. J., Merlin F., Nolan M. C., Praet A., Rozitis B., Sandford S. A., Schrader D. L., Thomas C. A., Zou X.-D., Lauretta D. S. and Osiris-Rex Team (2019) Evidence for widespread hydrated minerals on asteroid (101955) Bennu. *Nature Astron.* **3**, 332–340.

Harries D., Pollok K. and Langenhorst F. (2011) Translation interface modulation in NC-pyrrhotites: direct imaging by TEM and a model toward understanding partially disordered structural states. *Am. Mineral.* **96**, 716–731.

Harries D. and Langenhorst F. (2013) The nanoscale mineralogy of Fe, Ni sulfides in pristine and metamorphosed CM and CM/CI-like chondrites: tapping a petrogenetic record. *Meteorit. Planet. Sci.* **48**, 879–903.

Harries D. and Zolensky M. E. (2016) Mineralogy of iron sulfides in CM1 and CI1 lithologies of the Kaidun breccia: records of extreme to intense hydrothermal alteration. *Meteorit. Planet. Sci.* **51**, 1096–1109.

Hellmann J. L., Hopp T., Burkhardt C. and Kleine T. (2020) Origin of volatile element depletion among carbonaceous chondrites. *Earth Planet. Sci. Lett.* **549** 116508.

Hertkorn N., Ruecker C., Meringer M., Gugisch R., Frommberger M., Perdue E. M., Witt M. and Schmitt-Kopplin P. (2007) High-precision frequency measurements: indispensable tools at the core of the molecular-level analysis of complex systems. *Anal. Bioanal. Chem.* **389**, 1311–1327.

Hertkorn N., Harir M., Koch B. P., Michalke B. and Schmitt-Kopplin P. (2013) High-field NMR spectroscopy and FTICR mass spectrometry: powerful discovery tools for the molecular level characterization of marine dissolved organic matter. *Biogeosciences* **10**, 1583–1624.

Hertkorn N., Harir M. and Schmitt-Kopplin P. (2015) Non-target analysis of Murchison soluble organic matter by high-field NMR spectroscopy and FTICR mass spectrometry. *Magn. Reson. Chem.* **53**(9), 754–768.

Hertkorn N., Cawley K., Harir M., Schmitt-Kopplin P. and Jaffe R. (2016) Molecular characterization of dissolved organic matter from subtropical wetlands: a comparative study through the analysis of optical properties, NMR and FTICR/MS. *Biogeosciences* **13**, 2257–2277.

Hewins R. H., Bourot-Denise M., Zanda B., Leroux H., Barrat J.-A., Humayun M., Göpel C., Greenwood R. C., Franchi I. A., Pont S., Lorand J.-P., Cournede C., Gattacceca J., Rochette P., Kuga M., Marrocchi Y. and Marty B. (2014) The Paris meteorite, the least altered CM chondrite so far. *Geochim. Cosmochim. Acta* **124**, 190–222.

Holm A. (2020) *Mineralogical characteristics as indicators of the aqueous alteration in Flensburg* Bachelor Thesis. Institut für Planetologie, University of Münster, pp. 1–68.

Horstmann M. and Bischoff A. (2014) The Almahata Sitta polymict breccia and the late accretion of Asteroid 2008 TC$_3$ - Invited Review. *Chem. Erde* **74**, 149–184.

Horstmann M., Humayun M. and Bischoff A. (2014a) Clues to the origin of metal in Almahata Sitta EL and EH chondrites and implications for primitive E chondrite thermal histories. *Geochim. Cosmochim. Acta* **140**, 720–744.

Horstmann M., Vollmer C., Barth M. I. F., Chaussidon M., Gurenko A., and Bischoff A. (2014b) Tracking aqueous alteration of CM chondrites – insights from in situ oxygen isotope measurements of calcite. In Lunar and Planetary Science Conference 45, Abstract #1761.

Howard K. T., Benedix G. K., Bland P. A. and Cressey G. (2009) Modal mineralogy of CM2 chondrites by X-ray diffraction (PSD-XRD). Part 1: Total phyllosilicate abundance and the degree of aqueous alteration. *Geochim. Cosmochim. Acta* **73**, 4576–4589.

Howard K. T., Alexander C. M. O., Schrader D. L. and Dyl K. A. (2015) Classification of hydrous meteorites (CR, CM and C2 ungrouped) by phyllosilicate fraction: PSD-XRD modal mineralogy and planetesimal environments. *Geochim. Cosmochim. Acta* **149**, 206–222.

Huss G. R. and Lewis R. S. (1994) Noble gases in presolar diamonds I: Three distinct components and their implications for diamond origins. *Meteoritics* **29**(6), 791–810.

Hutchison R. (1996) Chondrules and their associates in ordinary chondrites: a planetary connection. In *Chondrules and the Protoplanetary Disk* (eds. R. H. Hewins, R. H. Jones and E. R. D. Scott). Cambridge Univ. Press, pp. 311–318.

Hutchison R., Williams C. T., Din V. K., Clayton R. N., Kirschbaum C., Paul R. L. and Lipschutz M. E. (1988) A planetary, H-group pebble in the Barwell, L6, unshocked chondritic meteorite. *Earth Planet. Sci. Lett.* **90**, 105–118.

Jilly-Rehak C. E., Huss G. R. and Nagashim K. (2017) ^{53}Mn–^{53}Cr radiometric dating of secondary carbonates in CR chondrites: Timescales for parent body aqueous alteration. *Geochim. Cosmochim. Acta* **201**, 224–244.

Johnson C. A. and Prinz M. (1991) Chromite and olivine in type II chondrules in carbonaceous and ordinary chondrites: implications for thermal histories and group differences. *Geochim. Cosmochim. Acta* **55**, 893–904.

Johnson C. A. and Prinz M. (1993) Carbonate compositions in CM and CI chondrites and implications for aqueous alteration. *Geochim. Cosmochim. Acta* **57**, 2843–2852.

Jull A. J. T., Cloudt S. and Cielaszyk E. (1998) 14C terrestrial ages of meteorites from Victoria Land, Antarctica and the infall rate of meteorites. In Meteorites: Flux with time and impact effects (eds. M. M. Grady, et al.). Geological Society London, Special Publication 140, 75–91.

Jull A. J. T., Burr G. S., Beck J. W., Hodgins G. W. L., Biddulph D. L., McHargue L. R., and Lange, T. E. (2008) Accelerator mass spectrometry of long-lived light radionuclides. In Analysis of Environmental radionuclides (ed. P. Povinec). Radioactivity in the Environment, vol. 11, Elsevier, Amsterdam, pp. 241–262.

Kallemeyn G. W. and Wasson J. T. (1981) The compositional classification of chondrites- I. The carbonaceous chondrite groups. *Geochim. Cosmochim. Acta* **45**, 1217–1230.

Kerraouch I., Ebert S., Patzek M., Bischoff A., Zolensky M. E., Pack A., Schmitt-Kopplin P., Belhai D., Bendaoud A. and Le L. (2019) A light, chondritic xenolith in the Murchison (CM) chondrite – formation by fluid-assisted percolation during metasomatism? *Geochemistry - Chemie der Erde* **79** 125518.

Kerraouch I., Bischoff A., Zolensky M.E., Pack A., Patzek M., Wölfer E., Burkhardt C., and Fries M. (2020) Characteristics of a new carbonaceous, metal-rich lithology found in the carbonaceous chondrite breccia Aguas Zarcas. Lunar and Planetary Science Conference 51, abstract #2011.

Kerridge J. F. (1985) Carbon, hydrogen, and nitrogen in carbonaceous chondrites: abundances and isotopic compositions in bulk samples. *Geochim. Cosmochim. Acta* **49**, 1707–1714.

King A. J., Schofield P. F., Howard K. T. and Russell S. S. (2015) Modal mineralogy of CI and CI-like chondrites by Xray diffraction. *Geochim. Cosmochim. Acta* **165**, 148–160.

King A. J., Schofield P. F. and Russell S. S. (2017) Type 1 aqueous alteration in CM carbonaceous chondrites: Implications for the evolution of water-rich asteroids. *Meteorit. Planet. Sci.* **52**, 1197–1215.

Kitazato K., Milliken R. E., Iwata T., Abe M., Ohtake M., Matsuura S., Arai T., Nakauchi Y., Nakamura T., Matsuoka M., Senshu H., Hirata N., Hiroi T., Pilorget C., Brunetto R., Poulet F., Riu L., Bibring J.-P., Takir D., Domingue D. L., Vilas F., Barucci M. A., Perna D., Palomba E., Galiano A., Tsumura K., Osawa T., Komatsu M., Nakato A., Arai T., Takato N., Matsunaga T., Takagi Y., Matsumoto K., Kouyama T., Yokota Y., Tatsumi E., Sakatani N., Yamamoto Y., Okada T., Sugita S., Honda R., Morota T., Kameda S., Sawada H., Honda C., Yamada M., Suzuki H., Yoshioka K., Hayakawa M., Ogawa K., Cho Y., Shirai K., Shimaki Y., Hirata N., Yamaguchi A., Ogawa N., Terui F., Yamaguchi T., Takei Y., Saiki T., Nakazawa S., Tanaka S., Yoshikawa M., Watanabe S. and Tsuda Y. (2019) The surface composition of asteroid 162173 Ryugu from Hayabusa2 near-infrared spectroscopy. *Science* **364**, 272–275.

Klein F. and Bach W. (2009) Fe–Ni–Co–O–S phase relations in peridotite-seawater interactions. *J. Petrology* **50**, 37–59.

Knie K., Merchel S., Korschinek G., Faestermann T., Herpers U., Gloris M. and Michel R. (1999) Accelerator mass spectrometry measurements and model calculations of iron-60 production rates in meteorites. *Meteorit. Planet. Sci.* **34**, 729–734.

Köôp L., Davis A. M., Nakashima D., Park C., Krot A. N., Nagashima K., Tenner T. J., Heck P. R. and Kita N. T. (2016) A link between oxygen, calcium and titanium isotopes in ^{26}Al-poor hibonite-rich CAIs from Murchison and implications for the heterogeneity of dust reservoirs in the solar nebula. *Geochim. Cosmochim. Acta* **189**, 70–95.

Krietsch D. (2020) Alteration on asteroids, diversity of primordial volatiles and their carriers in carbonaceous chondrites, and

martian Shergottite sampling sites – studied by meteoritic noble gases, PhD thesis, No. 26964, ETH Zurich Switzerland, 1–213. https://doi.org/10.3929/ethz-b-000445813.

Krot A. N., Nagashima K., Alexander C. M. O'D., Ciesla F. J., Fujiya W. and Bonal L. (2015) Sources of water and aqueous activity on the chondrite parent asteroids. In *Asteroids IV* (ed. P. Michel). Univ. of Arizona, Tucson, pp. 635–660.

Larsen K. K., Trinquier A., Paton C., Schiller M., Wielandt D., Ivanova M. A., Connelly J. N., Nordlund A., Krot A. N. and Bizzarro M. (2011) Evidence for magnesium isotope hetero-geneity in the solar protoplanetary disk. *Astrophys. J. Lett.* **735** (2), L37.

Lauretta D. S., Dellagiustina D. N., Bennett C. A., Golish D. R., Becker K. J., Balram-Knutson S. S., Barnouin O. S., Becker T. L., Bottke W. F., Boynton W. V., Campins H., Clark B. E., Connolly H. C., Drouet D'Aubigny C. Y., Dworkin J. P., Emery J. P., Enos H. L., Hamilton V. E., Hergenrother C. W., Howell E. S., Izawa M. R. M., Kaplan H. H., Nolan M. C., Rizk B., Roper H. L., Scheeres D. J., Smith P. H., Walsh K. J., Wolner C. W. V. and Osiris-Rex Team (2019) The unexpected surface of asteroid (101955) Bennu. *Nature* **568**, 55–60.

Lee M. R., Sofe M. R., Lindgren P., Starkey N. A. and Franchi I. A. (2013) The oxygen isotope evolution of parent body aqueous solutions as recorded by multiple carbonate generations in the Lonewolf Nunataks 94101 CM2 carbonaceous chondrite. *Geochim. Cosmochim. Acta* **121**, 452–466.

Lee M. R., Lindgren P. and Sofe M. R. (2014) Aragonite, breunnerite, calcite and dolomite in the CM carbonaceous chondrites: High fidelity recorders of progressive parent body aqueous alteration. *Geochim. Cosmochim. Acta* **144**, 126–156.

Lentfort S., Bischoff A. and Ebert S. (2019) Classification of 13 CM chondrite breccias and CM clasts in two achondrites. *Meteorit. Planet. Sci.* **54**, #6029.

Lentfort S., Bischoff A., Ebert S. and Patzek M. (2020) Classifi-cation of CM chondrite breccias – implications for the evaluation of samples from the OSIRIS-REx and Hayabusa 2 missions. *Meteorit. Planet. Sci.*. https://doi.org/10.1111/MAPS.13486.

Leya I. and Masarik J. (2009) Cosmogenic nuclides in stony meteorites revisited. *Meteorit. Planet. Sci.* **44**, 1061–1086.

Lindgren P., Lee M. R., Sofe M. R. and Zolensky M. E. (2013) Clasts in the CM2 carbonaceous chondrite Lonewolf Nunataks 94101: evidence for aqueous alteration prior to complex mixing. *Meteorit. Planet. Sci.* **48**, 1074–1090.

Mackinnon I. D. and Zolensky M. E. (1984) Proposed structures for poorly characterized phases in C2M carbonaceous chon-drite meteorites. *Nature* **309**, 240–242.

Mayeda T. K., Clayton R. N. and Yanai K. (1987) Oxygen isotopic compositions of several antarctic meteorites. *Mem. Natl Inst. Polar Res Spec.* **46**, 144–150.

McCoy T. J., Connolly, Jr., H. C., Corrigan C. M., Jawin E. R., Sandford S., Molaro J., DellaGiustina D. N., Rizk B., Nolan M. C., Lauretta D. S. and the OSIRIS-REx Team (2019) Brecciated boulders: evidence for impact mixing on Bennu's parent body (abstract #6428). *Meteorit. Planet. Sci.* **54**, #6428.

McKibbin S. J., Ireland T. R., Amelin Y. and Holden P. (2015) Mn–Cr dating of Fe- and Ca-rich olivine from 'quenched' and 'plutonic' angrite meteorites using Secondary Ion Mass Spec-trometry. *Geochim. Cosmochim. Acta* **157**, 13–27.

McSween, Jr., H. Y. (1979a) Are carbonaceous chondrites prim-itive or processed? A review. *Rev. Geophys.* **17**, 1059–1078.

McSween, Jr., H. Y. (1979b) Alteration in CM carbonaceous chondrites inferred from modal and chemical variations in matrix. *Geochim. Cosmochim. Acta* **43**, 1761–1770.

Meckenstock R. U., von Netzer F., Stumpp C., Lueders T., Himmelberg A. M., Hertkorn N., Schmitt-Kopplin Ph., Harir M., Hosein R., Haque S. and Schulze-Makuch D. (2014) Water droplets in oil are microhabitats for microbial life. *Science* **345** (6197), 673–676.

Meteoritical Bulletin Database (https://www.lpi.usra.edu/meteor).

Metzler K. and Bischoff A. (1996) Constraints on chondrite agglomeration from fine-grained chondrule rims. In *Chondrules and the Protoplanetary Disk* (eds. R. H. Hewins, R. H. Jones and E. R. D. Scott). Cambridge University Press, pp. 153–162.

Metzler K., Bischoff A. and Stöffler D. (1992) Accretionary dust mantles in CM-chondrites: evidence for nebula processes. *Geochim. Cosmochim. Acta* **56**, 2873–2897.

Morlok A. and Libourel G. (2013) Aqueous alteration in CR chondrites: meteorite parent body processes as analogue for long-term corrosion processes relevant for nuclear waste disposal. *Geochim. Cosmochim. Acta* **103**(X), 76–103.

Morlok A., Bischoff A., Stephan T., Floss C., Zinner E. K. and Jessberger E. K. (2006) Brecciation and chemical hetero-geneities of CI chondrites. *Geochim. Cosmochim. Acta* **70**, 5371–5394.

Morlok A., Schiller B., Weber I., Daswani M., Stojic A. N., Reitze M. P., Gramse T., Wolters S. D., Hiesinger H., Grady M. M. and Helbert J. (2020) Mid-infrared reflectance spectroscopy of carbonaceous chondrites and Calcium–Aluminum-rich inclu-sions. *Planet. Space Sci.* **193** 105078.

Mougel B., Moynier F. and Göpel C. (2018) Chromium isotopic homogeneity between the Moon, the Earth, and enstatite chondrites. *Earth Planet. Sci. Lett.* **481**, 1–8.

Neumann W. and Kruse A. (2019) Differentiation of Enceladus and retention of a porous core. *Astrophys. J.* **882**, 47.

Neumann W., Grott M., Trieloff M., Jaumann R., Biele J., Hamm M. and Kührt E. (2020) Microporosity and parent body of the rubble-pile NEA (162173) Ryugu. *Icarus*. https://doi.org/10.1016/j.icarus.2020.114166.

Niederer F. R., Papanastassiou D. A. and Wasserburg G. J. (1981) The isotopic composition of titanium in the Allende and Leoville meteorites. *Geochim. Cosmochim. Acta* **45**, 1017–1031.

Niese S., Köhler M. and Gleisberg B. (1998) Low-level counting techniques in the underground laboratory "Felsenkeller" in Dresden. *J. Radioanal. Nucl. Chem.* **233**, 167–172.

Norris T. L., Gancarz A. J., Rokop D. J., and Thomas K. W. (1983) Half-life of 26Al. In Proc. of the 14th Lunar and Planetary Science Conference, Journal of Geophysical Research Suppl. 8, B331–B333.

Pack A. and Herwartz D. (2014) The triple oxygen isotope composition of the Earth mantle and understanding $\Delta^{17}O$ variations in terrestrial rocks and minerals. *Earth Planet. Sci. Lett.* **390**, 138–145.

Pack A., Tanaka R., Hering M., Sengupta S., Peters S. and Nakamura E. (2016) The oxygen isotope composition of San Carlos olivine on VSMOW2-SLAP2 scale. *Rapid Commun. Mass Spectrom.* **30**, 1495–1504.

Patzek M., Bischoff A., Visser R. and John T. (2018a) Mineralogy of volatile-rich clasts in brecciated meteorites. *Meteorit. Planet. Sci.* **53**, 2519–2540.

Patzek M., Pack A., Bischoff A., Visser R. and John T. (2018b) O-isotope composition of CI- and CM-like clasts in ureilites, HEDs, and CR chondrites (abstract #6254). *Meteorit. Planet. Sci.* **53**, 6254.

Patzek M., Bischoff A., Hoppe P., Pack A., Visser R., and John T. (2019a) Oxygen and hydrogen isotopic evidence for the existence of several C1 parent bodies in the early solar system. Lunar and Planetary Science Conference 50, #1779.

Patzek M., Kadlag Y., Bischoff A., Visser R., Becker H. and John T. (2019b) Chromium isotopes and trace element concentration of xenolithic C1 clasts in brecciated chondrites and achondrites (abstract #6027). *Meteorit. Planet. Sci.* **54**, #6027.

Patzek M., Hoppe P., Bischoff A., Visser R. and John T. (2020) Hydrogen isotopic composition of CI- and CM-like clasts from meteorite breccias – sampling unknown sources of carbonaceous chondrite material. *Geochim. Cosmochim. Acta* **272**, 177–197.

Peters S. T., Alibabaie N., Pack A., McKibbin S. J., Raeisi D., Nayebi N., Torab F., Ireland T. and Lehmann B. (2020) Triple oxygen isotope variations in magnetite from iron-oxide deposits, central Iran, record magmatic fluid interaction with evaporite and carbonate host rocks. *Geology* **48**, 211–215.

Petitat M., Birck J.-L., Luu T. H. and Gounelle M. (2011) The chromium isotopic composition of the ungrouped carbonaceous chondrite Tagish Lake. *Astrophys. J.* **736**, 23.

Pieters C. M. and Englert P. A. J. (eds.) (1993) Topics in Remote Sensing 4. Remote Geochemical Analysis: Elemental and Mineralogical Composition. Cambridge University Press.

Popova O. P., Jenniskens P., Emel'yanenko V., Kartashova A., Biryukov E., Khaibrakhmanov S., Shuvalov V., Rybnov Y., Dudorov A., Grokhovsky V. I., Badyukov D. D., Yin Q.-Z., Gural P. S., Albers J., Granvik M., Evers L. G., Kuiper J., Kharlamov V., Solovyov A., Rusakov Y. S., Korotkiy S., Serdyuk I., Korochantsev A. V., Larionov M. Y., Glazachev D., Mayer A. E., Gisler G., Gladkovsky S. V., Wimpenny J., Sanborn M. E., Yamakawa A., Verosub K., Rowland D. J., Roeske S., Botto N. W., Friedrich J. M., Zolensky M., Le L., Ross D., Ziegler K., Nakamura T., Ahn I., Lee J. I., Zhou Q., Li X.-H., Li Q.-L., Liu Y., Tang G.-Q., Hiroi T., Sears D., Weinstein I. A., Vokhmintsev A. S., Ishchenko A. V., Schmitt-Kopplin P., Hertkorn N., Nagao K., Haba M. K., Komatsu M., Mikouchi T. and The Chelyabinsk Airburst Consortium (2013) Chelyabinsk airburst, damage assessment, meteorite recovery, and characterization. *Science* **342**, 1069–1073.

Povinec P. P., Masarik J., Sýkora I., Kováčik A., Beňo J., Meier M. M. M., Wieler R., Laubenstein M. and Porubčan V. (2015) Cosmogenic nuclids in the Košice meteorite: experimental investigations and Monte Carlo simulations. *Meteorit. Planet. Sci.* **50**, 880–892.

Qin L., Alexander C. M. O., Carlson R. W., Horan M. F. and Yokoyama T. (2010) Contributors to chromium isotope variation of meteorites. *Geochim. Cosmochim. Acta* **74**, 1122–1145.

ReVelle D. O. (1979) A quasi-simple ablation model for large meteorite entry: theory vs observations. *J. Atmos. Terr. Phys.* **41**(5), 453–473.

Riebe M. E. I., Welten K. C., Meier M. M. M., Wieler R., Barth M. I. F., Ward D., Laubenstein M., Bischoff A., Caffee M. W., Nishiizumi K. and Busemann H. (2017) Cosmic-ray exposure ages of six chondritic Almahata Sitta fragments. *Meteorit. Planet. Sci.* **52**, 2353–2374.

Robert F. and Epstein S. (1982) The concentration and isotopic composition of hydrogen, carbon and nitrogen in carbonaceous meteorites. *Geochim. Cosmochim. Acta* **46**, 81–95.

Rochette P., Gattacceca J., Bonal L., Bourot-Denise M., Chevrier V., Clerc J.-P., Consolmagno G., Folco L., Gounelle M., Kohout T., Pesonen L., Quirico E., Sagnotti L. and Skripnik A. (2008) Magnetic classification of stony meteorites: 2. Non-ordinary chondrites. *Meteorit. Planet. Sci.* **43**, 959–980.

Rowe M. W., Clayton R. N. and Mayeda T. K. (1994) Oxygen isotopes in separated components of CI and CM meteorites. *Geochim. Comochim. Acta* **58**, 5341–5347.

Rubin A. E. and Wasson J. T. (1986) Chondrules in the Murray CM2 meteorite and compositional differences between CM-CO and ordinary chondrite chondrules. *Geochim. Cosmochim. Acta* **50**, 307–315.

Rubin A. E., Trigo-Rodríguez J. M., Huber H. and Wasson J. T. (2007) Progressive aqueous alteration of CM carbonaceous chondrites. *Geochim. Cosmochim. Acta* **71**, 2361–2382.

Ruf A., Kanawati B., Hertkorn N., Yin Q. Z., Moritz F., Harir M., Lucio M., Michalke B., Wimpenny J., Shilobreeva S., Bronsky B., Saraykin V., Gabelica Z., Gougeon R., Quirico E., Ralew S., Jakubowski T., Haack H., Jenniskens P., Hinman N. W. and Schmitt-Kopplin Ph. (2017) Previously unknown class of metalorganic compounds revealed in meteorites. *Proc. Natl. Acad. Sci.* **114**, 2819–2824.

Rugel G., Pavetich S., Akhmadaliev S., Enamorado Baez S. M., Scharf A., Ziegenrücker R. and Merchel S. (2016) The first four years of the AMS-facility DREAMS: status and developments for more accurate radionuclide data. *Nucl. Instr. Meth. Phys. Res. B* **370**, 94–100.

Salisbury J. W., D'Aria D. M. and Jarosewich E. (1991) Midinfrared (2.5-13.5 μm) reflectance spectra of powdered stony meteorites. *Icarus* **92**, 280–297.

Sanders I. S. (1996) A chondrule-forming scenario involving molten planetesimals. In *Chondrules and the Protoplanetary Disk* (eds. R. H. Hewins, R. H. Jones and E. R. D. Scott). Cambridge Univ. Press, UK, pp. 327–334.

Sanborn M. E., Yin Q. Z., Irving A. J., and Bunch T. E. (2015) Differentiated planetesimals with chondritic crusts: New delta17O-ε54Cr evidence in unique, ungrouped achondrites for partial melting of the CV/CK and CO parent bodies. In Lunar and Planetary Science Conference 46, #2259.

Sanborn M. E., Wimpenny J., Williams C. D., Yamakawa A., Amelin Y., Irving A. J. and Yin Q.-Z. (2019) Carbonaceous achondrites Northwest Africa 6704/6693: milestones for early Solar System chronology and genealogy. *Geochim. Cosmochim. Acta* **245**, 577–596.

Scherer P. and Schultz L. (2000) Noble gas record, collisional history, and pairing of CV, CO, CK, and other carbonaceous chondrites. *Meteorit. Planet. Sci.* **35**(1), 145–153.

Schiller M., Van Kooten E., Holst J. C., Olsen M. B. and Bizzarro M. (2014) Precise measurement of chromium isotopes by MC-ICPMS. *J. Anal. Spectrom.* **29**, 1406–1416.

Schmidt C. (2020) 13C- und 18O-Isotope als Indikatoren für die Bildungsbedingungen der Karbonate im kohligen Chondriten Flensburg. Bachelor Thesis, Institut für Geowissenschaften, Universität Heidelberg.

Schmitt-Kopplin Ph., Gabelica Z., Gougeon R. D., Fekete A., Kanawati B., Harir M., Gebefuegi I., Eckel G. and Hertkorn N. (2010) High molecular diversity of extraterrestrial organic matter in Murchison meteorite revealed 40 years after its fall. *Proc. Natl. Acad. Sci.* **107**(7), 2763–2768.

Schmitt-Kopplin Ph., Harir M., Kanawati B., Tziotis D., Hertkorn N. and Gabelica Z. (2012) Chemical footprint of the solvent soluble extraterrestrial organic matter occluded in Sołtmany ordinary chondrite. *Meteorite J.* **1–2**(Special issue, Soltmany), 79–92.

Scott E. R. D., Keil K. and Stöffler D. (1992) Shock metamorphism of carbonaceous chondrites. *Geochim. Cosmochim. Acta* **56**, 4281–4293.

Shukolyukov A. and Lugmair G. W. (2006) Manganese–chromium isotope systematics of carbonaceous chondrites. *Earth Planet. Sci. Lett.* **250**(1–2), 200–213.

Singerling S. A. and Brearley A. J. (2018) Primary iron sulfides in CM and CR carbonaceous chondrites: insights into nebular processes. *Meteorit. Planet. Sci.* **53**, 2078–2106.

Singerling S. A. and Brearley A. J. (2020) Altered primary iron sulfides in CM2 and CR2 carbonaceous chondrites: insights into parent body processes. *Meteorit. Planet. Sci.* **55**, 496–523.

Sokol A. K., Bischoff A., Marhas K. K., Mezger K. and Zinner E. (2007a) Late accretion and lithification of chondritic parent bodies: Mg isotope studies on fragments from primitive chondrites and chondritic breccias. *Meteorit. Planet. Sci.* **42**, 1291–1308.

Sokol A. K., Mezger K., Chaussidon M. and Bischoff A. (2007b) Simultaneous accretion of differentiated or metamorphosed asteroidal clasts and chondrules. *Meteorit. Planet. Sci.* **42**, A143.

Sokol A. K., Fernandez V. A., Schulz T., Bischoff A., Burgess R., Clayton R. N., Münker C., Nishiizumi K., Palme H., Schultz L., Weckwerth G., Mezger K. and Horstmann M. (2008) Geochemistry, petrology and ages of the lunar meteorites Kalahari 008 and 009: new constraints on early lunar evolution. *Geochim. Cosmochim. Acta* **72**, 4845–4873.

Spurný P. (2016) Instrumentally documented meteorite falls: two recent cases and statistics from all falls. In Asteroids: New Observations, New Models. Proceedings IAU Symposium (eds. S. Chesley, A. Morbidelli, R. Jedicke & D. Farnocchia). 318, 69–79.

Spurný P., Borovicka J., Haloda J., Shrbeny L. and Heinlein D. (2016) Two very precisely instrumentally documented meteorite falls: Žd'ár nad Sázavou and Stubenberg – prediction and reality. *Meteorit. Planet. Sci.* **51**(Special Issue), #6221.

Spurný P., Borovička J., Baumgarten G., Haack H., Heinlein D. and Sørensen A. N. (2017) Atmospheric trajectory and heliocentric orbit of the Ejby meteorite fall in Denmark on February 6, 2016. *Planet. Space Sci.* **143**, 192–198.

Steele R. C. J., Heber V. S. and McKeegan K. D. (2017) Matrix effects on the relative sensitivity factors for manganese and chromium during ion microprobe analysis of carbonate: implications for early Solar System chronology. *Geochim. Cosmochim. Acta* **201**, 245–259.

Stöffler D., Keil D. and Scott E. R. D. (1991) Shock metamorphism of ordinary chondrites. *Geochim. Cosmochim. Acta* **55**, 3845–3867.

Telus M., Alexander C. M. O'D., Hauri E. H. and Wang J. (2019) Calcite and dolomite formation in the CM parent body: insight from in situ C and O isotope analyses. *Geochim. Cosmochim. Acta* **260**, 275–291.

Thorpe A. N., Senftle F. E. and Grant J. R. (2002) Magnetic study of magnetite in the Tagish Lake meteorite. *Meteorit. Planet. Sci.* **37**, 736–771.

Tikoo S.M., Monteith C., and Agostinelli V. (2019) Paleomagnetism of the Orgueil and Ivuna meteorites and implications for the evolution of the CI chondrite parent body. AGU Fall Meeting abstract #GP43B-0799.

Tomeoka K. and Buseck P. (1988) Matrix mineralogy of the Orgueil CI carbonaceous chondrite. *Geochim. Cosmochim. Acta* **52**, 1627–1640.

Tonui E., Zolensky M., Hiroi T., Nakamura T., Lipschutz M., Wang M.-S. and Okudaira K. (2014) Petrographic, chemical and spectroscopic evidence for thermal metamorphism in carbonaceous chondrites I: CI and CM chondrites. *Geochim. Cosmochim. Acta* **126**, 284–306.

Trieloff M., Jessberger E. K., Herrwerth I., Hopp J., Fiéni C., Ghélis M., Bourot-Denise M. and Pellas P. (2003) Structure and thermal history of the H-chondrite parent asteroid revealed by thermochronometry. *Nature* **422**, 502–506.

Trinquier A., Birck J. and Allegre C. J. (2007) Widespread [54]Cr heterogeneity in the inner Solar System. *Astrophys. J.* **655**, 1179–1185.

Trinquier A., Birck J. L., Allègre C. J., Göpel C. and Ulfbeck D. (2008a) [53]Mn–[53]Cr systematics of the early Solar System revisited. *Geochim. Cosmochim. Acta* **72**, 5146–5163.

Trinquier A., Birck J.-L. and Allègre C. J. (2008b) High-precision analysis of chromium isotopes in terrestrial and meteorite samples by thermal ionization mass spectrometry. *J. Anal. At. Spectrom.* **23**, 1565–1574.

Trinquier A., Elliott T., Ulfbeck D., Coath C., Krot A. N. and Bizzarro M. (2009) Origin of nucleosynthetic isotope hetero-

geneity in the solar protoplanetary disk. *Science* **324**, 374–376.

Tyra M. A., Farquhar J., Guan Y. and Leshin L. A. (2012) An oxygen isotope dichotomy in CM2 chondritic carbonates: a SIMS approach. *Geochim. Cosmochim. Acta* **77**, 383–395.

Tyra M., Brearley A. and Guan Y. (2016) Episodic carbonate precipitation in the CM chondrite ALH 84049: an ion microprobe analysis of O and C isotopes. *Geochim. Cosmochim. Acta* **175**, 195–207.

Urey H. C. (1959) Primary and secondary objects. *J. Geophys. Res.* **64**, 1721–1737.

Urey H. C. (1967) Parent bodies of the meteorites and origin of chondrules. *Icarus* **7**, 350–359.

Verdier-Paoletti M. J., Marrocchi Y., Avice G., Roskosz M., Gurenko A. and Gounelle M. (2017) Oxygen isotope constraints on the alteration temperatures of CM chondrites. *Earth Planet. Sci. Lett.* **458**, 273–281.

Vernazza P., Zanda B., Binzel R. P., Hiroi T., DeMeo F. E., Birlan M., Hewins R., Ricci L., Barge P. and Lockhart M. (2014) Multiple and fast: the accretion of ordinary chondrite parent bodies. *Astrophys. J.* **791**, 120.

Visser R., John T., Menneken M., Patzek M. and Bischoff A. (2018) Temperature constraints by Raman spectroscopy of organic matter in volatile-rich clasts and carbonaceous chondrites. *Geochim. Cosmochim. Acta* **241**, 38–55.

Wadhwa M., Bouvier A. and Janney P. E. (2013) Al-Mg systematics in a CAI from the NWA 6991 CV3 chondrite (abstr.). *Meteorit. Planet. Sci.* **48**, suppl. #5253.

Wallner A., Bichler M., Buczak K., Dressler R., Fifield L. K., Schumann D., Sterba J. H., Tims S. G., Wallner G. and Kutschera W. (2015) Settling the half-life of [60]Fe: fundamental for a versatile astrophysical chronometer. *Phys. Rev. Lett.* **114** 041101.

Watanabe S., Hirabayashi M., Hirata N., Noguchi R., Shimaki Y., Ikeda H., Tatsumi E., Yoshikawa M., Kikuchi S., Yabuta H., Nakamura T., Tachibana S., Ishihara Y., Morota T., Kitazato K., Sakatani N., Matsumoto K., Wada K., Senshu H., Honda C., Michikami T., Takeuchi H., Kouyama T., Honda R., Kameda S., Fuse T., Miyamoto H., Komatsu G., Sugita S., Okada T., Namiki N., Arakawa M., Ishiguro M., Abe M., Gaskell R., Palmer E., Barnouin O. S., Michel P., French A. S., McMahon J. W., Scheeres D. J., Abell P. A., Yamamoto Y., Tanaka S., Shirai K., Matsuoka M., Yamada M., Yokota Y., Suzuki H., Yoshioka K., Cho Y., Nishikawa N., Sugiyama T., Kikuchi H., Hemmi R., Yamaguchi Tomohir, Naoko Ogawa G., Ono Yuya Mimas, Yoshikawa K., Takahashi T., Takei Yo, Atsushi Fujii C., Hirose Takahiro Iwat, Hayakawa Masahik, Hosoda Satosh, Mori Osam, Sawada Hirotak, Shimada Takanob, Soldini Stefani, Yano Hajim, Tsukizaki Ryud, Ozaki Masanob, Yuichi Iijima K., Ogawa Masaki Fujimot, Ho T.-M., Moussi A., Jaumann R., Bibring J.-P., Krause C., Terui Fuyut, Saiki Takana, Nakazawa Sator and Tsuda Yuich (2019) Hayabusa 2 arrives at the carbonaceous asteroid 162173 Ryugu—a spinning top–shaped rubble pile. *Science* **364**, 268–272.

Weisberg M. K. and Huber H. (2007) The GRO 95577 CR1 chondrite and hydration of the CR parent body. *Meteorit. Planet. Sci.* **42**, 1495–1503.

Weisberg M. K., Prinz M., Clayton R. N. and Mayeda T. K. (1993) The CR (Renazzo-type) carbonaceous chondrite group and its implications. *Geochim. Cosmochim. Acta* **57**(7), 1567–1586.

Weisberg M. K., McCoy T. J. and Krot A. N. (2006) Systematics and evaluation of meteorite classification. In *Meteorites and the Early Solar System II* (eds. D. S. Lauretta and H. Y. McSween). Univ. of Arizona, Tucson, pp. 19–52.

Weyrauch M., Horstmann M. and Bischoff A. (2018) Chemical variations of sulfides and metal in enstatite chondrites –

Introduction of a new classification scheme. *Meteorit. Planet. Sci.* **53**, 394–415.

Wieler R. (2002) Cosmic-ray-produced noble gases in meteorites. *Rev. Mineral. Geochem.* **47**, 125–170.

Wieler R., Graf T., Signer P., Vogt S., Herzog G. F., Tuniz C., Fink D., Fifield L. K., Klein J., Middleton R., Jull A. J. T., Pellas P., Masarik J. and Dreibus G. (1996) Exposure history of the Torino meteorite. *Meteorit. Planet. Sci.* **31**, 265–272.

Williams N. H. (2015) *The origin of titanium isotopic anomalies within solar system material* PhD thesis. University of Manchester.

Wilson L., Keil K., Browning L. B., Krot A. N. and Bourcier W. (1999) Early aqueous alteration, explosive disruption, and reprocessing of asteroids. *Meteorit. Planet. Sci.* **34**, 541–557.

Wlotzka F. (2005) Cr spinel and chromite as petrogenetic indicators in ordinary chondrites: equilibration temperatures of petrologic types 3.7 to 6. *Meteorit. Planet. Sci.* **40**, 1673–1702.

Xu H., Shen Z. and Konishi H. (2014) Si-magnetite nano-precipitates in silician magnetite from banded iron formation: Z-contrast imaging and ab initio study. *Am. Mineral.* **99**, 2196–2202.

Yamakawa A., Yamashita K., Makishima A. and Nakamura E. (2010) Chromium isotope systematics of achondrites: chronology and isotopic heterogeneity of the inner solar system bodies. *Astrophys. J.* **720**, 150–154.

Yamanaka T. and Okita M. (2001) Magnetic properties of the Fe_2SiO_4-Fe_3O_4 spinel solid solutions. *Phys. Chem. Minerals* **28**, 102–109.

Yamashita K., Maruyama S., Yamakawa A. and Nakamura E. (2010) ^{53}Mn-^{53}Cr chronometry of CB chondrite: evidence for uniform distribution of ^{53}Mn in the early solar system. *Astrophys. J.* **723**, 20–24.

Yang J. and Epstein S. (1983) Interstellar organic matter in meteorites. *Geochim. Cosmochim. Acta* **47**, 2199–2216.

Yang J. and Epstein S. (1984) Relic interstellar grains in Murchison meteorite. *Nature* **311**, 544–547.

Zhang J., Dauphas N., Davis A. M. and Pourmand A. (2011) A new method for MC-ICPMS measurement of Ti isotopic composition: identification of correlated isotope anomalies in meteorites. *J. Anal. At. Spectrom.* **26**, 2197–2205.

Zhang J., Dauphas N., Davis A. M., Leya I. and Fedkin A. (2012) The proto-Earth as a significant source of lunar material. *Nat. Geosci.* **5**, 251–255.

Zhu K., Liu J., Moynier F., Qin L., Alexander C. M. O. and He Y. (2019) Chromium isotopic evidence for an early formation of chondrules from the Ornans CO chondrite. *Astrophys. J.* **873**, 82.

Zolensky M. E. and Ivanov A. (2003) The Kaidun microbreccia meteorite: a harvest from the inner and outer asteroid belt. *Chem. Erde* **63**, 185–246.

Zolensky M. E. and McSween, Jr., H. Y. (1988) Aqueous alteration. In *Meteorites and the Early Solar System* (eds. J. F. Kerridge and M. S. Matthews). University of Arizona Press, Tucson, Arizona, pp. 114–143.

Zolensky M. E., Bourcier W. L. and Gooding J. L. (1989a) Aqueous alteration on the hydrated asteroids: results of EQ3/6 computer simulations. *Icarus* **78**, 411–425.

Zolensky M. E., Barrett R. A. and Prinz M. (1989b) Petrography, mineralogy and matrix compositions of Yamato-82162, a new CI2 chondrite. *Proc. Lunar Planet. Sci. Conf.* **20**, 1253–1254.

Zolensky M. E., Ivanov A. V., Yang S. V., Mittlefehldt D. W. and Ohsumi K. (1996) The Kaidun meteorite: mineralogy of an unusual CM1 lithology. *Meteorit. Planet. Sci.* **31**, 484–493.

Zolensky M. E., Mittlefehldt D. W., Lipschutz M. E., Wang M., Clayton R. N., Mayeda T. K., Grady M. M., Pillinger C. and David B. (1997) CM chondrites exhibit the complete petrologic range from type 2 to 1. *Geochim. Cosmochim. Acta* **61**, 5099–5115.

Zolensky M. E., Nakamura K., Gounelle M., Mikouchi T., Kasama T., Tachikawa O. and Tonui E. (2002) Mineralogy of Tagish Lake: an ungrouped type 2 carbonaceous chondrite. *Meteorit. Planet. Sci.* **37**, 737–761.

Zolensky M.E., Gregory T., Takenouchi A., Nishiizumi K., Trieman A., Berger E., Le L., Fagan A., Velbel M., Imae N., Yamaguchi A., and Caffee M. (2015) CM carbonaceous chondrite lithologies and their space exposure ages (abstract 00226-01). In NIPR Symp. Antarctic Meteorites.

Zolensky M., Takenouchi A., Gregory T., Nishiizumi K., Caffee M., Velbel M., Ross K., Zolensky A., Le L. and Imae N. (2017) The relationship between cosmic-ray exposure ages and mixing of CM chondrite lithologies. Lunar and Planetary Science Conference 48, #2094.

Zook H. A. (1980) A new impact model for the generation of ordinary chondrites. *Meteoritics* **15**, 390–391.

Associate editor: Pierre Beck

The old, unique C1 chondrite Flensburg – Insight into the first processes of aqueous alteration, brecciation, and the diversity of water-bearing parent bodies and lithologies

Electronic Annex - Supplemental Materials

More details on the fall observations, recovery and further search

After the fireball observation (Fig. S1) the Maritime Rescue Coordination Centre Bremen of the German Maritime Search and Rescue Service (DGzRS) received several reports from ships in the North Sea and initially considered the bolide to be an emergency signal between the East Frisian Islands of Langeoog und Spiekeroog. They sent two inshore lifeboats into the area.

One day after the fireball event at around 11 am local time (CEST), Mr. Due-Hansen found the peculiar stone on top of the grass and he instantly remembered the news about the meteor over the North Sea the day before. He considered it to be unusual for a stone, to lie on top of the lawn and, therefore, suspected it had fallen from the sky. At the weekend he took the stone to his father in Denmark and showed it to some friends as well. Accordingly, the meteorite was touched by several people. The finder declared that he had used a strong magnet for testing the stone's ferromagnetic reaction, which was positive. It should also be mentioned that between the time the fireball was observed and the discovery, several millimeters of rain as well as elevated relative humidity were reported in Flensburg.

After reporting the meteorite find to the International Meteor Organization (IMO) website, Mr. Due-Hansen sent four pictures of the stone to the American Meteor Society operations manager Mike Hankey. In order to consult local experts in Germany, Mr. Hankey contacted the Arbeitskreis Meteore (AKM) and got in touch with meteorite specialist Dieter Heinlein, coordinator of the German Fireball Network of the DLR (Deutsches Zentrum für Luft- und Raumfahrt) for a scientific examination of the stone.

Two AKM members Laura Kranich and Carsten Jonas, who are based in Kiel, visited Erik Due-Hansen and his wife on September 27. They precisely measured and documented the finding site (54°45.6873' N, 9°22.7353' E = 54.761455° N, 9.378922° E) and interviewed the couple concerning the circumstances of the discovery. Finally, the finder handed over the golf ball-sized rock to Laura and Carsten, who immediately sent the small meteorite by priority mail to Augsburg for a detailed inspection by Dieter Heinlein. The Flensburg meteorite is a complete

individual weighing 24.5 grams and showing a very fresh black fusion crust with many contraction cracks. On a few patches, where the primary crust had been broken off, a thin layer of brownish (ochre-colored) secondary fusion crust is visible. A small physical scratch implies that the meteorite must have scraped a hard surface before it smoothly landed on the lawn of Mr. Due-Hansen's property.

On November 11 the 24.5 g Flensburg stone was delivered to the Institut für Planetologie in Münster for analysis and cutting into two major pieces of 17.03 g and 6.54 g.

Soon after the first meteorite find was confirmed and released, various searching activities in the Flensburg area were undertaken by AKM members and other parties, but, unfortunately, no further genuine meteorite piece was found. Several groups (Mike Hankey of the American Meteor Society, Laura Kranich and Carsten Jonas of AKM, as well as Jim Goodall from Michigan, USA) tried to calculate the bolide's luminous trajectory and the potential strewn field with different results.

This turned out to be a challenging problem, which only could be solved by sophisticated calibrations of some video records of the daylight fireball with night time images through Felix Bettonvil and Gerd Baumgarten. This fundamental spadework enabled Czech experts Jiří Borovička and Pavel Spurný, Ondřejov Observatory to determine the atmospheric path (Fig. S1) and the strewnfield of the multiple meteorite fall properly. Detailed results of these investigations will be published elsewhere in a separate paper.

Samples and Analytical procedures

Optical and electron microscopy

Several thin and thick sections of Flensburg (PL19171 (~71 mm^2), PL19172 (~132 mm^2) (PL19173 (~ 13 mm^2), PL19174 (~16 mm^2); Institut für Planetologie, Münster) were studied by optical and electron optical microscopy. A ZEISS polarizing microscope (Axiophot) was used for optical microscopy in transmitted and reflected light. To study the fine-grained textures and to identify the different mineral phases, a JEOL 6610-LV electron microscope (SEM) at the Interdisciplinary Center for Electron Microscopy and Microanalysis (ICEM) at the Westfälische Wilhelms-Universität Münster was used.

In an area of 15 mm², the size and abundance of relict chondrules have been measured 7 times by 4 different persons on a BSE map. The average sizes of relict chondrules range from ~126 (including all rounded objects as possible relict chondrules) to ~194 μm (only including the absolutely safe objects) with minimum and maximum sizes of ~25 μm and ~685 μm, respectively, in each run. On average, 134 relict chondrules have been measured with a size of 168 μm.

Chemical analyses using microprobe and SEM-EDS

Quantitative mineral and bulk analyses were obtained using a JEOL JXA 8530F electron microprobe (EPMA) at the Institut für Mineralogie in Münster, which was operated at 15 kV and a probe current of 15 nA. Natural and synthetic standards were used for wavelength dispersive spectrometry. Jadeite (Na), kyanite (Al), sanidine (K), chromium oxide (Cr), San Carlos olivine (Mg), hypersthene (Si), diopside (Ca), rhodonite (Mn), rutile (Ti), fayalite (Fe), apatite (P), celestine (S), and nickel oxide (Ni) were used as standards for mineral analyses.

To avoid the effects of porosity during microprobe analyses, the Si and S concentrations were calculated from the bulk composition obtained by microprobe (average of 135 defocused beam analyses; Meteoritical Bulletin Database, 2020) correlated with the ICP-AES data for Mg, Al, and Ca.

For the analyses of carbonates the following standards were used: Dolomite (Mg), jadeite (Na), calcite (Ca), strontianite (Sr), Cr_2O_3 (Cr), siderite (Fe) rhodonite (Mn), and witherite (Ba).

For quantitative (EDS) analysis using the Münster-SEM, both, samples and appropriate mineral standards were measured at an excitation voltage of 20 kV, and the beam current constancy was controlled by a Faraday cup. Standard (Astimex) olivine (Mg, Fe, Si), jadeite (Na), plagioclase (Al), sanidine (K), diopside (Ca), rutile (Ti), chromium-oxide (Cr), rhodonite (Mn), and pentlandite (Ni) were used as natural and synthetic standards. The INCA analytical program provided by Oxford Instruments was used for these EDS analyses.

FIB- and TEM-studies

FIB work was done at FSU Jena using a FEI Quanta 3D FEG FIB-SEM workstation and followed the FIB sample preparation outlined by Harries and Zolensky (2016). The TEM study of the extracted FIB sections was done at FSU Jena using a FEI Tecnai G2 FEG operated at

200 kV and equipped with an Oxford X-Max 80T SDD EDS detector and a Gatan Quantum GIF energy filter for electron energy loss spectroscopy (EELS).

FIB sampling sites were primarily selected to target sulfide crystals and adjacent phyllosilicates and locations were optimized to include other minerals of interest. A total of three FIB sections (F01-03) were extracted from thin section PL19173 of Flensburg. For comparison, two FIB sections of the Kaidun CM1 lithology in thin section 56.01 studied by Harries and Zolensky (2016) were revisited.

Computed tomography (CT)

The CT was performed at the Helmholtz-Institute Freiberg for Resource Technology. The meteorite was scanned in a CoreTom CT scanner from Tescan at 130 keV using one 0.4 mm thick steel filter mounted at the source. The current was 11 W, which is optimized so that the resolution is limited by geometrical factors and not by the spot size of the beam. The voxel size was 11.7 µm. Reconstruction was done using the XRE recon v1.0.0.111. A ring filter and a beam hardening correction of 0.45 were used to homogenize the grey-scale throughout the sample. Image processing and visualization was done in Avizo 9.3.0. A 3D non-local-means filter (window = 15, neighbour = 3, similarity = 0.4) was used to remove noise with minimum impact on object boundaries.

Modal analysis by X-ray techniques

The mineralogy of Flensburg was initially characterized using a PANalytical X'Pert Pro scanning X-ray diffractometer (XRD) at the Natural History Museum (NHM), London. For this ~1 mg of powdered sample was mixed with several drops of acetone and deposited as a thin smear on a zero-background substrate. XRD patterns were collected using Co Kα radiation from $5 - 70°$ (2θ) with a step size of 0.02° and time/step of 25 seconds, giving a total measurement time of ~24 hours. Mineral phases in the samples were identified using the International Centre for Diffraction Data (ICDD) database (PDF-2).

Modal mineral abundances were determined using an Enraf-Nonius PDS120 XRD equipped with an INEL curved 120° position-sensitive-detector (PSD) in a static geometry relative to the primary X-ray beam and sample. Approximately 50 mg of powdered Flensburg was loaded into an aluminium sample well using the sharp edge of a spatula to minimise preferred crystal alignments. The X-ray beam (Cu Kα$_1$ radiation) was restricted to 0.24×2.00 mm and set at an incident angle of 3.4° to the flat top of the sample which was rotated throughout the

measurement. The XRD pattern for Flensburg was collected for 4 hours, and patterns of mineral standards were acquired under exactly the same experimental conditions for 15 minutes. Mineral abundances were calculated using a profile-stripping method, whereby the XRD pattern of a mineral standard was scaled to the same measurement time as the Flensburg analysis (i.e. ×16) and then reduced in intensity by a factor to match its intensity in the XRD pattern of Flensburg. The standard pattern was subtracted to leave a residual pattern. This process was repeated for all phases identified in Flensburg until there were zero counts left in the residual and the sum of the fit factors was one. The fit factors for the mineral standards were then corrected for relative differences in X-ray absorption to give their final volume fractions in Flensburg, with detection limits on the order of $0.5 - 1$ vol% (for details see King et al., 2015) and uncertainties in the abundances of $0.5 - 4.4$ vol%. A pattern of Flensburg is given in Fig. S16.

Bulk chemical analyses (including water and C-analyses)

The bulk sample of about 1 g from Flensburg was crushed and homogenized and about 250 mg were used for analyses at the Institut Universitaire Européen de la Mer, Université de Bretagne Occidentale in Plouzané, France. The chemical compositions of the bulk samples were obtained from a 104 mg subsample using ICP-AES (for Al, Fe, Mn, Mg, Na, Cr, Co, and Ni) and ICP-SFMS. Details are given by Barrat et al. (2012, 2015, 2016). The concentration reproducibility is generally much better than 5% at the chondritic level.

Water analyses of three samples of the Flensburg-meteorite were performed at the Institute for Geology, Mineralogy and Geophysics, Ruhr-University Bochum using a Mitsubishi CA 200 moisturemeter. For a single analysis, about 3-5 mg of the crushed sample was heated in an HF-oven to 1000°C; the gaseous components were then conducted into the titration cell, where the water content was measured by the Karl-Fischer-method. The instrument was tested with an internal laboratory standard (5 wt.% H_2O) prior to and after the measurements. The precision of this method is 5 % relatively. Effects of terrestrial water adsorption do not play a significant role. In this study, one sample was stored at room conditions for some days prior to analysis and was not annealed to 110°C prior to analysis. The result of 9.89 wt.% water demonstrates that the samples do not react with the humidity of the air and that all obtained values are identical according to the precision of the machine.

The determination of the CO_2 content was done using the C/S 500 instrument of ELTRA with an IR-detector. A sample of 13 mg was heated in an oxygen atmosphere up to 1100 °C. All carbon present reacts to form CO_2 which is transported in an oxygen flow towards the detector (C_{total}).

Oxygen isotopes

The oxygen isotope composition of bulk material of the Flensburg meteorite was analyzed by means of laser fluorination in combination with gas source mass spectrometry (for analytical details, see Pack et al., 2016 and Peters et al., 2020). Three individual chips were analyzed in two consecutive sessions. The $\delta^{17}O$ and $\delta^{18}O$ are reported on VSMOW scale, and the $\Delta'^{17}O$ is defined as

$$\Delta'^{17}O = 1000 \, ln\left(\frac{\delta^{17}O}{1000} + 1\right) - 0.528 * 1000 \, ln\left(\frac{\delta^{18}O}{1000} + 1\right) \qquad \text{(Equation 1)}$$

A $\Delta'^{17}O$ value of San Carlos olivine of –0.052‰ (average value of Pack et al., 2016; Sharp et al., 2016, and Wostbrock et al., 2020) was used to anchor $\delta^{17}O$ on VSMOW scale.

Titanium and Cr isotope analyses

Titanium and Cr isotope analyses on 20-50 mg samples of Flensburg were performed in Münster and Zürich. Analyses performed at the ETH Zürich were carried out on a single 26 mg aliquot of the powdered Flensburg meteorite. The analytical procedure is described in Bischoff et al. (2019).

Considering the Ti isotope analysis in Münster, an aliquot of ~30 mg sample powder (equivalent to ~20 μg Ti) was digested in HF-HNO_3-$HClO_4$ (2:1:0.05) on a hotplate at 180–200 °C for five days and in aqua regia (HCl-HNO_3) at 130–150 °C for another two days. Thereafter, the sample was dissolved in 12 M HNO_3, and ~65 mg H_3BO_3 were added. Ti was separated from the sample matrix via a two-stage anion exchange chromatography adapted from the previously established procedure from Zhang et al. (2011). In a first step, the sample solution was loaded onto a column prepacked with 2 ml TOGDA® anion exchange resin, where Ti was eluted in 20 ml 12 M HNO_3–1 wt.% H_2O_2. Afterwards, the Ti cut was dissolved in 2.5 ml 4 M HF and loaded onto a clean-up column filled with 0.8 ml Bio-Rad® AG1-X8 anion exchange resin, where Ti was eluted in 6 ml 9 M HCl–0.01 M HF.

Titanium isotope measurements were made in two lines using a ThermoScientific Neptune Plus MC-ICPMS (Multicollector Inductively Coupled Plasma Mass Spectrometry) in medium resolving power mode (Zhang et al., 2011). Solutions containing about 200 ppb Ti in 0.3 M HNO_3 – 0.0014 M HF were introduced through a Cetac Aridus II desolvating system, resulting in a ~3.5×10^{-10} A ion beam on ^{48}Ti. Mass bias was corrected using the exponential law and $^{49}Ti/^{47}Ti$ = 0.749766. The Ti isotope anomalies are reported as parts per ten thousand deviation (ε-notation) from the terrestrial OL-Ti (Millet and Dauphas, 2014) bracketing standard. The sample uncertainty is reported as the Student-t 95% confidence interval based on repeated analyses (n=13) of the sample solution on five different days. In the case of the Cr isotope analysis in Münster, Cr was collected during the first step of the two-stage anion exchange chromatography used for the separation of Ti, where Cr is eluted in 25 ml 12 M HNO_3 (+ trace H_3BO_3) together with most other matrix elements. An aliquot (equivalent to ~30 µg Cr) was taken from this solution, dried down, and redissolved in 1 ml 6 M HCl.

Afterward, Cr was separated from the sample matrix using a single-stage anion exchange chemistry for the removal of Fe (Bio-Rad® AG1-X8 anion exchange resin), followed by a two-stage cation exchange chromatography (Bio-Rad® AG50W-X8 cation exchange resin) as described by Yamakawa et al. (2009), including a four-day conversion of $Cr[III]Cl_3/Cr[II]Cl_2$ to Cr^{3+}.

Chromium isotope measurements were performed using a ThermoScientific Triton Plus Thermal Ionization Mass Spectrometer in static mode. The sample solution (~500 ppm Cr in 6 M HCl) was loaded on 4 filaments and each filament was measured multiple times, with total ion beam intensities of ~1.4×10^{-10} A on ^{52}Cr. Instrumental mass fractionation was corrected assuming a constant $^{50}Cr/^{52}Cr$ = 0.051859 and using the exponential law. The data is reported as $\varepsilon^{54}Cr$ value as the parts per ten thousand deviation from the terrestrial NIST SRM3112a Cr standard. The sample uncertainty is reported as the Student-t 95% confidence interval based on repeated analyses (n=12).

Tellurium isotope analysis

The sample powder of Flensburg (~70 mg) was spiked with a ^{123}Te-^{125}Te double spike, digested in HF–HNO_3, and Te was purified using a three-stage column chemistry modified after Fehr et al. (2004) and Brennecka et al. (2017). The Te isotope measurements were performed using a Neptune *Plus* MC-ICPMS at Münster combined with a Cetac Aridus II. Results are reported in $\delta^{128/126}Te$ as the per mil deviation from the NIST SRM 3156 Te standard.

Oxygen, carbon, and Mn-Cr isotope studies by SIMS

Oxygen 3 isotope, simultaneous carbon and oxygen, as well as Mn-Cr isotope compositions in calcite and dolomite were determined using the Cameca IMS1280-HR ion microprobe at Heidelberg University (HIP).

For oxygen 3 isotope measurements (Fig. 12) we used a $\sim$ 1.3 nA, 20 keV Cs^+ primary ion beam with a raster size of 6 µm (8 µm during pre-sputtering). Negative secondary ions were accelerated to 10 keV. The secondary ion image was limited to 15 µm, the dynamic transfer optical system (DTOS) was activated and sample charging was compensated with the electron gun (NEG). ^{16}O, ^{17}O and ^{18}O were detected simultaneously in three Faraday cup (FC) detectors. The nominal mass resolving power for ^{16}O and ^{18}O was 2500 and 7000 for ^{17}O. The contribution of $^{16}OH^-$ on the ^{17}O peak was negligible at < 0.1‰. Secondary intensities for ^{16}O and ^{17}O were $\sim 1.5 \times 10^9$ cps and $\sim 6 \times 10^5$ cps, respectively. Prior to each analysis, the secondary beam was centered automatically in the field aperture (X and Y) and the entrance slit (X only). Including the time for beam centering, the analyses started after a total pre-sputtering time of 90 s and each analysis had 25 cycles with 8 s integration time per cycle. The internal precision reported is the standard deviation of the mean value of the isotope ratios. The baseline of the Faraday cup amplifiers was determined separately with an integration time of 200 s several times per session.

NBS19 limestone (NIST RM 8544, $\delta^{18}O_{VSMOW}$ = +28.65 ‰, Brand et al. 2014) was used as reference material for the calibration of the oxygen isotope analyses. For $\delta^{17}O_{VSMOW}$ we assumed a value of +14.85 ‰ which was calculated using the mean $\Delta^{17}O$ value from Passey et al. (2014) and Barkan et al. (2015). The reference material was on a separate sample holder and was analyzed prior to and during the analytical session. The repeatability (1sd) for $\delta^{17}O$, $\delta^{18}O$ and $\Delta^{17}O$ of the calibration was 0.25 ‰, 0.16 ‰ and 0.26 ‰, respectively.

The dolomite O isotope analyses were corrected for the differences in instrumental mass fractionation (bias) between NBS19 (calcite) and dolomite–ankerite. A constant calcite–dolomite bias of –4.4 ‰ for $\delta^{18}O$ was assumed (Tyra et al., 2016). The dolomites have a mean Fe# of 0.10 ± 0.02 which causes an additional bias of $\sim$ +5.8 ‰ for $\delta^{18}O$. This bias was calculated individually for each dolomite grain using the fit curve equation in Fig. 2 of Śliwiński et al. (2016a) and the Fe# calculated from the EPMA analysis of the same grain. Both bias

corrections (which almost cancel each other out) were applied and the bias correction for $\delta^{17}O$ was calculated by applying a factor of 0.528 to the $\delta^{18}O$ bias correction.

For single-spot simultaneous carbon and oxygen isotope analyses, a modified setup was used: the 20 keV Cs^+ primary ion beam was reduced to 0.5 nA beam current and a raster size of 5 µm (7 µm during pre-sputtering). ^{12}C and ^{13}C (and $^{12}CH_2$ for monitoring purposes) were detected simultaneously in a FC detector (L'2) and two electron multiplier (EM) detectors (axial EM and H2), with mass resolving powers of 2500, 4000 and 2500, respectively, and typical secondary ion intensities of $\sim 4 \times 10^6$ cps and $\sim 4 \times 10^4$ cps, respectively. ^{16}O and ^{18}O were detected simultaneously in two FC detectors (C and H'2) with typical secondary ion intensities of $\sim 7 \times 10^8$ cps and $\sim 1.4 \times 10^6$ cps. This method of alternating carbon and oxygen multicollection enabled combined (and therefore correlated) carbon and oxygen isotope analyses on relatively small carbonate grains. Pre-sputtering time was 120 s and each analysis comprised 20 cycles with 15 s integration time per cycle for carbon and 8s for oxygen. Only measurements with $^{12}CH_2/^{12}C < 10^{-4}$ were used, to ensure that possible contributions from epoxy and/or organic carbon were avoided. For the oxygen isotope analyses the same standard and bias correction procedures as above were applied. For carbon isotopes measurements, again NBS19 limestone (NIST RM 8544, $\delta^{13}C_{VPDB} = +1.95$ ‰; Brand et al., 2014) was used as reference material for calibration. A constant calcite–dolomite bias of –9.2 ‰ for $\delta^{18}O$ was assumed (Tyra et al., 2016). The dolomites analyzed in this session had a mean Fe# of 0.10 ± 0.02 which caused an additional mean bias of $\sim$ –2.6 ‰ for $\delta^{13}C$. Again, this bias was calculated individually for each dolomite grain using the fit curve equation in Fig. 2 of Śliwiński et al. (2016b) and the Fe# calculated from the EPMA analysis of the same grain. The reference material was on a separate sample holder and was analyzed prior to and during the analytical session, and the repeatability (1sd) of the calibration was 0.5 ‰ for both $\delta^{13}C$ and $\delta^{18}O$. The inevitable drift of the measured $^{13}C/^{12}C$ ratio caused by aging of the EM was corrected for by linear regression.

For Mn-Cr we used a $\sim$ 4 nA, 23 keV O^- primary ion beam with a diameter of $\sim$ 10 µm. Positive secondary ions were accelerated to 10 keV and the secondary ion image was limited to 15 µm. All isotopes were detected simultaneously in multi-collection mode. The nominal mass resolving power was 7000 for ^{55}Mn and 8000 for ^{52}Cr and ^{53}Cr. ^{52}Cr and ^{53}Cr were detected by electron multipliers in pulse counting mode, while ^{55}Mn was detected by the axial Faraday cup

detector (10^{11} Ω amplifier) for dolomite or by the axial electron multiplier for calcite. Prior to each analysis, the secondary beam was centered automatically in the field aperture (X and Y) and the entrance slit (X only). Including the time for beam centering, the analyses started after a total pre-sputtering time of 120 s and each analysis typically consisted of 100 cycles with 4 s integration time per cycle. The ^{53}Cr/^{52}Cr and the ^{55}Mn/^{52}Cr ratios were calculated using the cumulated count rates of the isotopes. Errors of the ratios and Pearson's correlation coefficient ρ were calculated from the standard error of the mean count rates. IsoplotR (Vermeesch, 2018) was used for the linear regression (model: maximum likelihood) of the Mn-Cr isochrone.

The instrumental mass fractionation of -8 ± 1 ‰ for ^{53}Cr/^{52}Cr was determined using San Carlos olivine and assuming its ^{53}Cr/^{52}Cr ratio to be 0.11339 (Meija et al., 2013). The ion yield of Mn relative to Cr for calcite (*RIY*, defined as SIMS ratio / real ratio) was determined on the synthetic calcite MnCr–22 (Donohue et al., 2019) using concentrations next to the SIMS spots determined by EPMA. $RIY_{Mn/Cr,cal}$ from 9 analyses was 0.693 ± 0.056 (1sd). Based on our $RIY_{Mn/Cr, cal}$, we calculated our $RIY_{Mn/Cr,dol} = 1.087$ using the relative sensitivity factors (which are the inverse of our *RIY*) for calcite and dolomite from Steele et al. (2017).

Analyses of bulk H, C and N elemental and isotopic compositions

The determination of the bulk H, C and N elemental and isotopic compositions of Flensburg followed the protocols used by Alexander et al. (2012, 2013). Briefly, two aliquots (~2 mg) of the crushed Flensburg sample were weighed into Ag capsules for H analysis, and two aliquots (~8 mg) were weighed into Sn capsules for C and N analysis. The samples were stored in a desiccator for several days and reweighed to remove adsorbed atmospheric water. Prior to H analysis, the samples were placed in an autosampler and flushed with zero-grade, dry He for two hours to remove water that was adsorbed from the atmosphere during the transfer from the desiccator to the autosampler.

The elemental and isotopic analyses were made with: 1) a Thermo Scientific DeltaV^{plus} mass spectrometer connected to a Carlo Erba (NA 2500) elemental analyzer (CE/EA) via a Conflo III interface for C and N analyses, and 2) a Thermo Finnigan Delta^{plus}XL mass spectrometer connected to a Thermo Finnigan Thermal Conversion elemental analyzer (TC/EA) via a Conflo III interface for H analyses. The Conflo III interface facilitates the introduction of the N_2 and CO_2 reference gases for the N and C isotope analyses. in contrast a dual inlet system facilitates the introduction of the H_2 reference gas for the H isotope analyses. A H_3^+ correction was

determined and applied to the H measurements (Sessions et al., 2001). We used in-house standards to normalize and correct the data at regular intervals to monitor the accuracy and precision of the measured isotopic ratios and elemental compositions throughout the runs. These in-house standards, which included both gases and solid materials, have been calibrated against international (SMOW, NBS-22, PDB, and air) and other certified standards from Isoanalytical, USGS, NBS and Oztech. Standards were analyzed at regular intervals to monitor the internal precision of the measured isotopic ratios and elemental compositions throughout the run. The reported uncertainties for the elemental and isotopic analyses correspond to the highest 1σ deviations attained from either the replicate analyses of distinct subsamples (n > 2) or the internal standards.

For the H analyses, the two samples were analyzed sequentially to check for both sample heterogeneity and small memory effects that are known to occur. Blanks were also run before and after them, again to reduce any memory effects. There was little evidence for significant heterogeneity or memory effects. There is no memory effect for C and N analyses.

Radionuclides

Radionuclide analysis by non-destructive low-level gamma-spectrometry was performed in the underground laboratory "Felsenkeller" in Dresden, Germany (Niese et al., 1998). The laboratory is situated under a rock overburden of 138 m w.e. (water equivalent), resulting in a suppression of the total muon intensity by a factor of 30-40 (Ludwig et al., 2019). A gamma-spectrometry system dedicated to the analysis of very low activity levels was utilized. The spectrometer is based on a coaxial p-type high-purity germanium (HPGe) detector of 92% relative efficiency with enhanced front-side sensitivity for low-energy gamma-rays. All construction elements were selected for low radioactivity contents. The passive shielding is graded and consists of 5 cm of electrolytic copper, 5 cm of low-activity lead (2.7 Bq kg^{-1} ^{210}Pb) and an outer layer of 10 cm lead with 33 Bq kg^{-1} ^{210}Pb. Detailed information about the gamma-spectrometry system can be found in Köhler et al. (2009).

The non-destructive gamma-spectrometric measurement of the whole specimen (24.5 g) started on 11th October 2019 (less than one month after the bolide event) and was continued until 28th October with some short breaks (<1 h) due to device maintenances, resulting in a total measurement time of 17 days. To allow for a more precise radionuclide determination, the

energy-dependent detection efficiency of the detector was determined from the measurement of a meteorite dummy made of material with known naturally-occurring radionuclide contents.

For the destructive determination of long-lived radionuclides via accelerator mass spectrometry (AMS), a 35.60 mg aliquot of the homogenized bulk powder (~1 g) was radiochemically treated (Merchel and Herpers, 1999). It yielded in the production of suitable chemical compounds BeO, Al_2O_3, AgCl, CaF_2, NiO, MnO_2, and Fe_2O_3. Basic steps were: (a) addition of stable isotope carriers (^{9}Be, ^{27}Al, ^{nat}Cl, ^{nat}Ca, ^{55}Mn) in the form of solutions; (b) pressurized digestion in HF/HNO_3; (c) liquid aliquot for ICP-MS measurements for determination of natural occurring Al, Ca, Fe, Mg, Mn, and Ni; (d) anion and cation exchange; (e) precipitations; (f) drying and partial oxidation for oxide compounds and (g) mixing with metal powder, i.e., BeO with Nb, all other oxides and CaF_2 with Ag. To date these target materials have been analyzed for cosmogenic radionuclides ^{10}Be, ^{26}Al, ^{41}Ca, and ^{60}Fe by AMS. Measurements of the remaining other nuclides are foreseen in the future (^{36}Cl, ^{53}Mn, ^{59}Ni). The Flensburg sample was chemically treated together with six other ordinary chondrites and a corresponding processing blank. The latter sample combines all sources from the background, i.e. from chemical processing and AMS measurements (Table S9), and is of utmost importance for samples with radionuclide contents near the detection limit. A separate sample (25 mg) was extracted at the University of Arizona, and the ^{14}C measurement was made at the Arizona AMS Laboratory, using procedures described in Jull et al. (1998).

The heavier nuclides (^{41}Ca and ^{60}Fe) were determined at the Heavy Ion Accelerator Facility (HIAF) at the Australian National University (ANU) in Canberra (Wallner et al., 2015, 2016), whereas the lighter nuclides were measured at the 6 MV AMS-facility DREAMS in Dresden (Akhmadaliev et al., 2013; Rugel et al., 2016). In-house AMS-standards and calibration materials used are SMD-Be-12 with ^{10}Be/^{9}Be = $(1.704 \pm 0.030) \times 10^{-12}$, SMD-Al-11 with ^{26}Al/^{27}Al = $(9.66 \pm 0.14) \times 10^{-12}$, SMD-Ca-11 with ^{41}Ca/^{40}Ca = $(9.944 \pm 0.092) \times 10^{-12}$, and in-house ^{60}Fe/Fe material (known to ~10%), which is based on material provided by the TU Munich and on material from recent meteorite studies (Leya et al., 2020). They had been previously cross-calibrated against material from PSI with a well-known ^{60}Fe/Fe ratio of $(1.234 \pm 0.007) \times 10^{-12}$ (Schumann et al., 2019). All calibration materials are half-life independent. However, for the conversion of isotope ratios into specific radionuclide activities, we have used the following half-life values: (1.387 ± 0.012) Ma for ^{10}Be (Korschinek et al., 2010), (0.705 ± 0.024) Ma for ^{26}Al (Norris et al., 1983), and (0.104 ± 0.005) Ma for ^{41}Ca (Paul et al., 1991) to compare with production rates (see below).

Specific activities are compared to time-, depth-, and radius-depending production rates from theoretical Monte Carlo calculations (Leya and Masarik, 2009). These are based on input parameters for target elements from ICP-SFMS measurements (Table 4) for Ca, Ti, Mn, Rb, Sr, Y, Zr, Ba; from ICP-MS measurements from the liquid aliquot of the AMS sample for Fe, Mg, Ni; and from Table 5 for C and N. Data for important target elements producing lighter radionuclides, i.e. Na, Al, Si, and S, have been taken from microprobe analysis. The water content has been taken into account by filling–up all measured element concentrations to 99% with oxygen, i.e., leaving 1% for hydrogen (from H_2O), which is producing no relevant radionuclides. In the current version of the calculation tool kindly provided by Ingo Leya (U Bern) no adjustment for different densities are easily possible, which influences the precision of shielding depths and radii.

IR Spectroscopy

For the mid-infrared reflectance spectroscopy, a Bruker Vertex 70v spectrometer in the IRIS lab at the Institut für Planetologie of the University of Münster was used. Polished thin sections of Flensburg (PL19171) and of other meteorites were analyzed (Table S8). Possible organic contamination at the surface of the thin sections was removed with ethanol. We used different observation geometries for the measurements with the incident and emergent angle between 20° and 40°, using a Bruker A513 bidirectional reflectance stage. The used detector was a liquid nitrogen cooled MCT-detector. The mean of 512 interferogram scans per geometry was calculated in the measured wavelength range from 2 to 18 μm. All measurements took place at room temperature of ~23°C and at pressures of ~2 hPa. For the background calibration, we use a polished gold mirror. The spectral data will be available in the upcoming IRIS database for space science missions (Weber et al., 2018).

Organics

Twelve T Fourier transform ion cyclotron mass spectrometry (FTICR/MS) and 800 MHz ^{1}H nuclear magnetic resonance spectroscopy (NMR) based characterization used methanolic extracts obtained from the solid specimen with a weight of a very few mg as developed for characterization of Murchison and other extraterrestrial soluble organic matter (SOM) (Schmitt-Kopplin et al., 2010; Popova et al., 2013; Hertkorn et al., 2015). A single fragment of Flensburg (20.6 mg) was divided into several aliquots; two pieces (~5 mg each) were washed

with LC/MS grade methanol (Fluka) to remove surface contamination; this washing fluid was discarded. Both fragments were consecutively crushed and ground in an agate mortar with an agate pestle for ~20 sec under LCMS grade methanol. The solutions were transferred to two separate Eppendorf tubes and centrifuged at 16000 rpm for 3 minutes. The first solution was directly used for FTICR mass spectrometry (Schmitt-Kopplin et al., 2010). For NMR spectroscopy, the centrifugate was transferred to a glass flask and evacuated in a vacuum (with loss of unspecified volatiles). Then, 750 µL CD_3OD (99.95% ^2H, Merck) were added, followed by vacuum evaporation. This procedure was repeated two times to fully exchange CH_3OH with CD_3OD. Prior to all operations, all vessels and handling devices were extensively washed with LCMS grade methanol to attenuate terrestrial contamination as far as possible. A ^1H NMR spectrum, with solvent suppression (*noesypr1d*) was acquired with a Bruker AV III 800 spectrometer operating at $B_0 = 18.7$ T, as described in Hertkorn et al. (2015), from 45 µL extract in 1.7 mm Bruker NMR Match tubes, with number of scans = 22194 and processed with an exponential line broadening of 4 Hz. ^1H NMR spectra of CD_3OD alone (~450 µL; ns = 1392) were acquired under identical conditions, and did not show NMR resonances obtained from Flensburg SOM at any relevant S/N ratio (data not shown in Figures of this work).

Magnetic Properties

The magnetic properties of the rock were studied in Aix-en-Provence and Nördlingen. Most magnetic measurements were performed at CEREGE (Aix-en-Provence, France) on a 267 mg bulk sample with no fusion crust. Hysteresis measurements were performed with a Princeton Micromag Vibrating Sample Magnetometer (VSM) with a maximum applied field of 1 T and a sensitivity of ~5×10^{-9} Am^2. The analysis of hysteresis loops provided the ratio of saturation remanent magnetization (M_{RS}) to saturation magnetization (M_S) and the coercive force (B_C). High field susceptibility (χ_{HF}) was determined by a linear fit for applied fields > 0.9 T of the hysteresis loops. Remanent coercive force (B_{CR}) was determined by back field experiments performed with the VSM. The low field specific susceptibility (χ in m^3/kg) and its evolution at low temperature were measured using Agico MFK1 apparatus with sensitivity of 5×10^{-13} m^3, operating at 200 A/m and a frequency of 976 Hz, equipped with a CSL cryostat. The coercivity spectrum was estimated through stepwise acquisition and measurement of isothermal remanent magnetization (IRM) using the VSM. We determined the S_{-300} ratio, defined as the IRM obtained after applying a 3 T field and then a back field of 0.3 T normalized to the IRM acquired in 3 T. For this experiment, IRM was imparted using a pulse magnetizer from Magnetic

Measurement. Remanence measurements were performed with a 2G SQUID magnetometer model 755R) equipped with an automatic 3-axis alternating field (AF) demagnetization system. In Nördlingen, the M̲agnetic S̲usceptibility (MS) was measured with the handheld device SM-30 from ZH Instruments (www.zhinstruments.cz).

Density

The density of Flensburg was measured by two different methods: In a first approach, the bulk density of the rough piece was determined in Augsburg with the method described by Consolmagno et al. (1998) using 40 μm diameter glass beads. In a later measurement the volume of the 17.03 g piece obtained by CT was used for density calculations. Consistent results were obtained by both methods.

Parent body modeling

The thermal evolution of the Flensburg parent body was calculated using a 1D thermal evolution code (Neumann and Kruse, 2019; Neumann et al., 2020) that was adapted to a carbonaceous chondritic composition specific to the Flensburg meteorite. The code uses a finite-differences grid and solves conservation equation for energy as well as equations for the evolution of porosity that result in a global contraction of the body considered. The model accounts for heating by short- and long-lived radionuclides (Table S10) and for the consumption of the latent heat of water ice melting. The pre-hydration initial composition included a water mass fraction of 10%, producing a post-hydration phyllosilicate mass fraction of 84%. The model incorporates an initial microporosity of 0.5. Compaction of the porous material was calculated (Neumann et al., 2014, 2015, 2020) using experimentally determined creep laws, i.e., a power law for phyllosilicates (Hilairet et al., 2007; Amiguet et al., 2012) and a diffusion creep equation for the remaining fraction of the material (Schwenn and Goetze, 1978). An initial and ambient temperature of 170 K was adopted as appropriate for water-rich objects that were accreted outside of the snow line (Hayashi, 1981). For the choice of temperature- and porosity-dependent material properties according to a phyllosilicate-rich composition and for a detailed model description, we refer to Neumann et al. (2020).

Table S1: Representative analyses of calcite (Calc), dolomite (Dol), and the Na-rich carbonate (Na-carb.); All data are in wt.%. n.d. = not detected.

	Calc	Calc	Calc	Calc	Dol	Dol	Dol	Dol	Na-carb
MgO	0.06	0.19	<0.02	0.05	16.4	16.3	16.2	15.6	0.05
Na$_2$O	n.d.	<0-03	n.d.	<0.03	0.06	0.04	0.08	n.d.	12.3
CaO	56.7	56.7	56.6	56.0	30.1	29.0	29.4	30.4	44.0
SrO	0.14	0.08	n.d.	n.d.	0.06	<0.02	<0.02	n.d.	0.06
Cr$_2$O$_3$	<0.02	n.d.	0.07	n.d.	0.06	0.09	<0.03	n.d.	n.d.
FeO	0.43	0.82	0.91	0.75	3.6	4.0	3.6	3.6	0.51
MnO	0.65	0.21	0.10	0.06	3.5	3.7	3.9	3.8	n.d.
BaO	0.06	<0.03	0.08	n.d.	<0.03	0.05	n.d.	n.d.	n.d.

Table S2: Representative analyses of sulfides in Flensburg. Pentlandite = Pent; pyrrhotite = Po; all data are in wt.%; n.d. = not detected.

	S	Fe	Co	Ni	Total
Pent	33.4	33.2	1.61	30.9	99.2
Pent	33.9	37.7	1.34	27.0	100.0
Pent	33.1	33.5	1.49	31.6	99.6
Pent	32.3	39.8	1.23	24.9	98.2
Pent	33.9	42.4	1.10	21.0	98.4
Pent	33.4	34.6	1.38	31.6	100.9
Po	38.5	61.2	n.d.	0.57	100.3
Po	38.5	61.4	n.d.	0.18	100.0
Po	38.5	61.3	n.d.	0.38	100.2
Po	38.1	61.6	n.d.	0.23	99.9
Po	38.8	61.0	n.d.	0.56	100.3
Po	37.8	61.5	n.d.	0.18	99.6

Table S3: Representative analyses of oxides in Flensburg. Mag = magnetite; Chr = chromite. All data in wt.%. n.d. = not detected; oxygen of magnetite analyzed and not calculated. Oxygen of chromite calculated assuming all Fe being Fe^{2+} (TEM-EDX, totals normalized to 100 wt.%).

	O	Mg	Si	Fe	Ti	Cr	Mn	Ni	Total
Mag	27.1	0.17	2.12	67.9	0.37	0.06	0.13	<0.04	97.9
Mag	26.8	0.06	2.06	68.3	0.09	0.07	0.07	0.05	97.6
Mag	27.9	0.06	2.09	67.9	0.58	0.05	0.13	<0.04	98.8
Mag	27.9	0.06	1.67	69.0	0.08	0.09	0.10	<0.02	99.0
Mag	27.1	0.14	1.87	68.1	0.20	0.06	0.15	n.d.	97.8
Mag	26.8	0.06	2.10	68.2	0.07	0.05	0.14	<0.04	97.5
Mag	27.0	0.07	1.59	69.6	n.d.	n.d.	0.13	0.10	98.6
Mag	26.6	n.d.	0.04	71.7	n.d.	n.d.	<0.03	0.06	98.5
Mag	27.3	0.04	2.02	68.7	0.17	0.08	0.04	n.d.	98.4
	O	Mg	Al	Fe	Ti	Cr	Mn	Ni	Total
Chr	33.3	4.8	10.5	22.4	4.2	24.7	<0.10	n.d.	100
Chr	33.9	5.1	12.4	21.0	3.1	24.6	<0.10	n.d.	100

Table S4: Simultaneous single-spot carbon and oxygen isotope data of Flensburg calcites and dolomites. Uncertainties are 1 sigma (1s), dolomite errors do not contain uncertainties of systematic correction for calcite–dolomite bias (Tyra et al., 2016) and uncertainties of correction for Fe content (Śliwiński et al. 2016a,b) for $\delta^{13}C$ and $\delta^{18}O$.

Calcite					Calcite continued				
analyses	$\delta^{13}C$	1s	$\delta^{18}O$	1s	analyses	$\delta^{13}C$	1s	$\delta^{18}O$	1s
CO@0	+34.0	0.6	+17.3	0.3	CO@109	+48.3	0.4	+13.6	0.2
CO@1	+41.4	0.3	+23.4	0.3	CO@110	+45.1	0.3	+14.7	0.3
CO@2	+46.5	0.5	+18.0	0.3	CO@112	+45.6	0.4	+19.5	0.4
CO@6	+40.4	0.3	+19.2	0.3	CO@113	+36.4	0.8	+14.3	0.3
CO@9	+47.0	0.3	+24.2	0.2	CO@114	+39.5	0.5	+18.1	0.6
CO@10	+45.5	0.5	+16.7	0.3	CO@120	+43.5	0.4	+16.3	0.3
CO@11	+60.4	0.4	+16.0	0.4	CO@121	+49.7	0.5	+15.2	0.4
CO@15	+24.0	0.3	+16.6	0.3	CO@122	+18.5	0.5	+16.0	0.3
CO@16	+37.1	0.2	+16.1	0.3	CO@124	+51.8	0.5	+15.6	0.4
CO@17	+63.5	0.4	+16.1	0.4	CO@130	+28.3	1.1	+15.7	0.3
CO@20	+23.7	0.6	+15.2	0.3	CO@131	+32.4	1.6	+21.2	0.5
CO@22	+33.1	0.6	+16.4	0.5	CO@134	+46.4	0.3	+16.7	0.3
CO@24	+41.7	0.4	+16.5	0.3	CO@135	+20.7	0.9	+22.0	0.2
CO@25	+53.2	0.4	+16.8	0.3					
CO@26	+47.3	0.3	+17.4	0.2					
CO@30	+24.9	1.3	+19.2	0.6	Dolomite				
CO@34	+37.2	0.5	+21.0	0.5	analyses	$\delta^{13}C$	1s	$\delta^{18}O$	1s
CO@39	+51.3	0.4	+15.1	0.2	CO@7	+55.2	0.3	+14.9	0.3
CO@43	+45.9	0.5	+15.0	0.3	CO@8	+57.7	0.3	+13.0	0.4
CO@46	+45.0	0.2	+14.9	0.2	CO@12	+58.8	0.4	+14.8	0.3
CO@47	+43.8	1.9	+17.1	0.2	CO@13	+55.3	0.4	+14.8	0.3
CO@48	+28.4	1.1	+20.5	0.2	CO@21	+48.7	0.5	+12.7	0.4
CO@49	+51.1	0.5	+31.0	0.3	CO@23	+48.6	0.6	+13.0	0.5
CO@50	+50.0	0.5	+18.3	0.3	CO@24	+52.9	0.4	+16.7	0.3
CO@54	+25.5	0.9	+17.5	0.3	CO@27	+57.4	0.4	+15.2	0.3
CO@57	+44.4	0.4	+14.8	0.4	CO@29	+49.1	0.3	+13.4	0.2
CO@58	+45.0	0.3	+15.0	0.3	CO@33	+54.7	0.3	+13.8	0.3
CO@62	+44.9	0.4	+14.6	0.4	CO@37	+57.2	0.9	+15.3	0.3
CO@63	+46.2	0.4	+15.1	0.4	CO@53	+58.7	0.3	+15.1	0.3
CO@64	+44.1	0.3	+16.5	0.7	CO@56	+55.5	0.4	+15.5	0.3
CO@67	+43.3	0.3	+24.9	0.4	CO@59	+59.8	0.5	+15.3	0.4
CO@71	+45.4	0.3	+14.9	0.3	CO@60	+53.8	2.3	+15.6	0.3
CO@74	+46.1	0.4	+19.0	0.3	CO@61	+49.1	0.3	+13.4	0.3
CO@75	+59.6	0.5	+14.8	0.3	CO@65	+59.4	0.3	+16.4	0.4
CO@76	+28.1	0.3	+17.5	0.2	CO@69	+59.5	0.3	+14.7	0.3
CO@78	+42.3	0.5	+26.7	0.2	CO@72	+59.2	0.3	+15.7	0.2
CO@79	+39.6	0.5	+17.4	0.2	CO@73	+56.7	0.3	+14.3	0.3
CO@86	+47.9	0.3	+16.7	0.2	CO@77	+55.5	0.5	+14.9	0.3
CO@90	+41.0	0.3	+21.8	0.3	CO@87	+50.8	0.6	+14.1	0.3
CO@92	+41.6	1.1	+25.4	0.3	CO@88	+58.7	0.4	+15.2	0.3
CO@94	+16.3	0.4	+16.8	0.4	CO@89	+58.0	0.3	+15.6	0.2
CO@96	+35.2	0.4	+15.9	0.2	CO@95	+58.1	0.3	+16.4	0.2
CO@97	+26.0	1.0	+17.0	0.2	CO@101	+54.8	0.9	+16.5	0.2
CO@99	+45.2	0.4	+15.4	0.3	CO@105	+59.0	0.4	+15.2	0.3
CO@100	+16.8	0.4	+14.9	0.4	CO@111	+57.4	0.3	+14.4	0.4
CO@102	+43.8	0.4	+25.3	0.4	CO@116	+58.7	0.3	+16.3	0.2
CO@106	+41.9	0.5	+23.5	0.3	CO@118	+57.6	0.3	+15.7	0.3
CO@107	+43.9	0.4	+25.2	0.4	CO@123	+58.5	0.4	+16.0	0.2
CO@108	+45.2	0.5	+14.5	0.3	CO@133	+49.1	0.3	+14.8	0.3

Table S5a: Results of analyzed EMPA and SIMS spots. The location of the spots (denoted with @) can be found in Fig. S17). RIY= Relative Ion Yield; SE = Standard Error

EPMA No.	Cr (wt%)	Mn (wt%)	^{55}Mn/^{52}Cr	SIMS-Nr. @	^{55}Mn/^{52}Cr	1SE (%)	RIY
6	0.330	0.996	3.411				
25	0.333	0.793	2.688				
26	0.315	0.915	3.283				
	0.326	0.901	3.124	**HIGP@0**	2.383	0.862	0.763
13	0.318	1.258	4.465				
21	0.355	1.223	3.890				
23	0.313	0.864	3.119				
26	0.315	0.915	3.283				
	0.325	1.065	3.698	**HIGP@1**	2.354	0.259	0.636
9	0.285	0.713	2.828				
10	0.323	0.761	2.663				
12	0.349	0.897	2.903				
18	0.278	0.913	3.704				
19	0.162	0.768	5.352				
	0.279	0.810	3.276	**HIGP@2**	2.090	0.563	0.638
16	0.151	0.495	3.697				
17	0.273	0.819	3.390				
33	0.276	0.909	3.715				
34	0.175	0.525	3.386				
	0.219	0.687	3.545	**HIGP@3**	2.313	0.524	0.653
12	0.349	0.897	2.903				
13	0.318	1.258	4.465				
18	0.278	0.913	3.704				
22	0.272	1.061	4.412				
	0.304	1.032	3.831	**HIGP@4**	2.729	0.539	0.712
1	0.304	0.822	3.058				
4	0.318	0.925	3.283				
11	0.341	0.798	2.639				
	0.321	0.848	2.984	**HIGP@5**	2.365	0.652	0.793
2	0.291	0.637	2.476				
3	0.325	0.693	2.409				
8	0.290	0.661	2.572				
	0.302	0.664	2.483	**HIGP@6**	1.768	0.453	0.712
35	0.318	1.294	4.595				
36	0.304	0.868	3.228				
37	0.285	0.795	3.146				
38	0.298	0.980	3.721				
	0.301	0.984	3.691	**HIGP@7**	2.477	0.327	0.671
27	0.332	0.960	3.269				
30	0.323	0.917	3.207				
	0.327	0.939	3.239	**HIGP@8**	2.140	0.407	0.661

| | | | | | | mean RIY: | **0.693** |
| | | | | | | 1sd: | **0.056** |

Table S5b: ^{55}Mn/^{52}Cr and ^{53}Cr/^{52}Cr values for calcites and dolomites within the unique Flensburg carbonaceous chondrite; SE = Standard Error; rho = correlation coefficient ρ

Calcite

^{55}Mn/^{52}Cr	1SE	^{53}Cr/^{52}Cr	1SE	rho
0.6	0.0	0.11285	0.00023	0.27
77e.5	4.9	0.11259	0.00952	0.63
3.7	0.1	0.11303	0.00311	0.59
81773.4	4008.9	0.44256	0.04037	0.53
475977.9	62142.1	2.01613	0.30784	0.85
385629.2	45422.3	1.87962	0.26333	0.83
10735.1	981.5	0.16362	0.01987	0.73
1764.1	49.1	0.12078	0.00478	0.69
22371.1	1463.3	0.21880	0.03285	0.43
12240.3	898.4	0.19548	0.03244	0.43
697.4	17.1	0.10730	0.00445	0.51
1239.5	91.0	0.11934	0.01100	0.44
2.9	0.2	0.11316	0.01254	0.68
22.0	0.6	0.11207	0.00342	0.56
112768.2	7540.5	0.57808	0.06387	0.60
263002.2	26135.2	1.64956	0.20663	0.78
2.9	0.1	0.11288	0.00507	0.68
31.7	1.5	0.11260	0.00772	0.69
6564.0	1175.9	0.14706	0.03462	0.75
223220.7	27505.5	1.17892	0.19233	0.74
95.1	1.7	0.11336	0.00272	0.66
2.8	0.0	0.11294	0.00108	0.47
3.0	0.0	0.11278	0.00159	0.55
1172.8	15.2	0.11911	0.00288	0.49
30.3	0.8	0.11197	0.00341	0.60
8.3	0.4	0.11286	0.00584	0.56
40.3	0.7	0.11311	0.00269	0.70

Table S5b
continued

Dolomite

^{55}Mn/^{52}Cr	1SE	^{53}Cr/^{52}Cr	1SE	rho
2261.0	116.1	0.12028	0.00830	0.73
1010.3	70.8	0.11622	0.01126	0.72
842.2	108.8	0.11582	0.02076	0.71
139844.3	3746.9	0.76061	0.03342	0.59
560894.7	32598.4	2.83122	0.18740	0.87
2097.9	161.4	0.11994	0.01257	0.73
129.8	7.3	0.11321	0.00890	0.71
5417.2	596.2	0.13471	0.01941	0.76
1024.5	10.9	0.11691	0.00183	0.56
415790.0	18865.9	2.03796	0.10974	0.83
2904.1	105.8	0.12659	0.00621	0.72
37534.1	2128.4	0.25751	0.01726	0.84
686397.0	51568.0	3.15657	0.25311	0.93
11392.0	764.0	0.15398	0.01292	0.79
732501.0	43705.5	3.81986	0.25636	0.88
27278.0	710.8	0.24055	0.00861	0.71
59425.8	3876.4	0.36707	0.02693	0.88
519781.6	31107.1	2.78918	0.19056	0.87
1850871.8	165943.6	8.56855	0.81712	0.93
376.5	6.4	0.11441	0.00263	0.69
793568.2	59502.5	3.79338	0.31196	0.90
506955.1	26619.2	2.56623	0.15556	0.86
782467.6	41007.2	3.64626	0.22111	0.85
2971.9	163.4	0.12373	0.00916	0.73
655883.1	36649.8	3.11253	0.19758	0.87
111920.2	6335.3	0.63070	0.03988	0.89
7879.8	401.3	0.14567	0.01012	0.72
1048.8	64.8	0.11615	0.00986	0.72
1478.8	42.7	0.11862	0.00478	0.70
5.8	0.1	0.11289	0.00093	0.45
1031334.2	74678.0	4.93189	0.38447	0.92
184440.4	5517.1	0.89266	0.03892	0.67
419413.6	18920.6	1.90747	0.10126	0.84
15358.9	378.2	0.16736	0.00594	0.67
346.4	6.7	0.11482	0.00309	0.70
624794.7	33451.2	2.89495	0.17537	0.87
452181.2	20582.8	2.14644	0.11778	0.82
682229.5	33766.3	3.11895	0.17450	0.87
292984.1	11313.0	1.30304	0.06241	0.79
243083.2	9155.5	1.21331	0.05793	0.77
372088.9	15207.4	1.83029	0.09195	0.80
2516.0	194.2	0.12043	0.01245	0.74
825291.9	40436.2	3.51696	0.19645	0.87
120605.0	2747.4	0.66094	0.02348	0.62

Table S6: Range of possible production rates P_x, determined for radii <200 cm and allowed shielding depths based on a $^{22}Ne/^{21}Ne$ ratio of 1.11 and bulk chemistry given in Table 4 using the model of Leya and Masarik (2009) for noble gases ^{38}Ar, ^{21}Ne, and ^3He.

cm³/(g×Ma)	P_{38}	P_{21}	P_3
All allowed shielding depths	0.030-0.047	0.130-0.304	1.166-1.899
Restricted shielding depths*	0.030-0.047	0.145-0.304	1.177-1.898

*production rates restricted to most probable shielding depths, assuming 85% mass loss during atmospheric entry, excluding 22% of the inner radius excluding thereby 1 % of the mass (see text for details).

Table S7: Maximum cosmic ray exposure ages T_x in Ma based on restricted production rates of noble gases ^{38}Ar, ^{21}Ne, and ^3He.

	T_{38}	T_{21}	T_3	CRE age range
S	0.39±0.13	0.17±0.10	0.25±0.09	0-0.20±0.05
L	0.20±0.06	0.14±0.08	0.20±0.07	

Table S8: Overview of the meteorites used for infrared spectroscopy, the PL-number of the used thin section, ID to the IRIS (Infrared and Raman for Interplanetary Spectroscopy) data base, aperture, and viewing geometry of the measurements.

Meteorite	Class, type, group	PL-number	ID	Aperture in mm	Viewing geometry in °	Wavelength region in µm
Flensburg	C1 ung	PL19171	198	1.5	i25;e15	8 to 18
Flensburg	C1 ung	PL19171	198	0.5	i20;e15	2 to 4
Alais	CI1	PL92322	201	0.5	i20;e30	8 to 18, 2 to 4
Orgueil	CI1	PL92321	210	0.5	i20;e15	8 to 18
Orgueil	CI1	PL92321	210	1.5	i40;e30	2 to 4
Murchison	CM2	PL89464	204	0.5	i20;e15	8 to 18
Cold Bokkeveld	CM2	PL17148	211	0.5	i20;e30	8 to 18, 2 to 4
Allende	CV3	PL04256	203	0.5	i20;e15	8 to 18
Acfer 182	CH3	PL01267	202	0.5	i20;e15	8 to 18

Table S9: AMS data for Flensburg and corresponding processing blank. ^{10}Be and ^{26}Al have been measured at Dresden, and ^{41}Ca and ^{60}Fe at Canberra. Specific activities for ^{10}Be, ^{26}Al, and ^{41}Ca for Flensburg are calculated from the AMS ratios, ICP-MS results (^{27}Al and ^{nat}Ca) or carrier addition (^{9}Be), sample weight and half-lives. The specific activity values are blank-corrected and their given uncertainties (1-sigma) include those associated to blank-corrections.

	Flensburg	Blank
^{10}Be [counts]	2108	42
^{10}Be/^{9}Be [E-15]	97.3±2.9	1.92±0.30
^{10}Be [dpm/kg]	0.0539±0.0016	
^{26}Al [counts]	151	1
^{26}Al/^{27}Al [E-15]	149±15	$1.8^{+3.2}_{-1.1}$
^{26}Al [dpm/kg]	0.209±0.030	
^{41}Ca [counts]	5	1
^{41}Ca/^{40}Ca [E-15]	23^{+16}_{-13}	$4.3^{+7.6}_{-2.8}$
^{41}Ca [dpm/kg]	$0.37^{+0.32}_{-0.26}$	
^{60}Fe [counts]	1	1
^{60}Fe/Fe [E-17]	6^{+11}_{-4}	$4.0^{+7.0}_{-2.6}$
^{60}Fe [dpm/kg]	comparable to blank	

Table S10: Parameters used for calculation in the models. The data for the calculation of the radiogenic energy production are from Barrat et al. (2012), Kita et al. (2013), Tang and Dauphas (2012), Finocchi and Gail (1997), and Van Schmus (1995). The element mass fractions refer to stable isotopes, the initial ratios are between unstable and stable isotopes of an element, and the decay energies are per particle.

Isotope	^{26}Al	^{60}Fe	^{40}K	^{232}Th	^{235}U	^{238}U
Element mass fraction	$1.16 \cdot 10^{-2}$	$2.12 \cdot 10^{-1}$	$3.42 \cdot 10^{-4}$	$3.98 \cdot 10^{-8}$	$1.12 \cdot 10^{-8}$	$1.12 \cdot 10^{-8}$
Half-life (years)	$7.17 \cdot 10^{5}$	$2.62 \cdot 10^{6}$	$1.25 \cdot 10^{9}$	$1.41 \cdot 10^{10}$	$7.04 \cdot 10^{8}$	$4.47 \cdot 10^{9}$
Initial ratio	$5.25 \cdot 10^{-5}$	$1.15 \cdot 10^{-8}$	$1.5 \cdot 10^{-3}$	1.0	0.24	0.76
Decay energy (J)	$4.99 \cdot 10^{-13}$	$4.34 \cdot 10^{-13}$	$1.11 \cdot 10^{-13}$	$6.47 \cdot 10^{-12}$	$7.11 \cdot 10^{-12}$	$7.61 \cdot 10^{-12}$

Figures:

Fig. S1: Map showing the daylight fireball of September 12, 2019 (yellow arrow) and the finding site of the 24.5 g Flensburg meteorite in northern Germany. The yellow points indicate the video cameras which recorded the bolide. DC: Dorian Cieloch (Wremen), CH: Christian Hirsch (Hannover-Laatzen), JS: Jörg Strunk (Herford), HS: Holger Scheele (Rügen), MM: Mertrade shipyard (Marknesse), LP: Leon Pepping (Almere Buiten), GK: Gerard Kemna (Nijmegen), WS: NV Westerscheldetunnel (Marchal van Lare). Using the calibrated video recordings of the locations JS, GK and HS, the trajectory of the fireball was calculated by Jiří Borovička and Pavel Spurný, Ondřejov. Map: Google Earth.

Fig. S2: The Flensburg stony meteorite weighing 24.5 grams in pristine finding condition. The chondrite shows black primary fusion crust, which is typical for a fresh fall, and unusual ochre-colored secondary fusion crust on some broken faces (windows) of the meteorite fragment. Photos: Erik Due-Hansen.
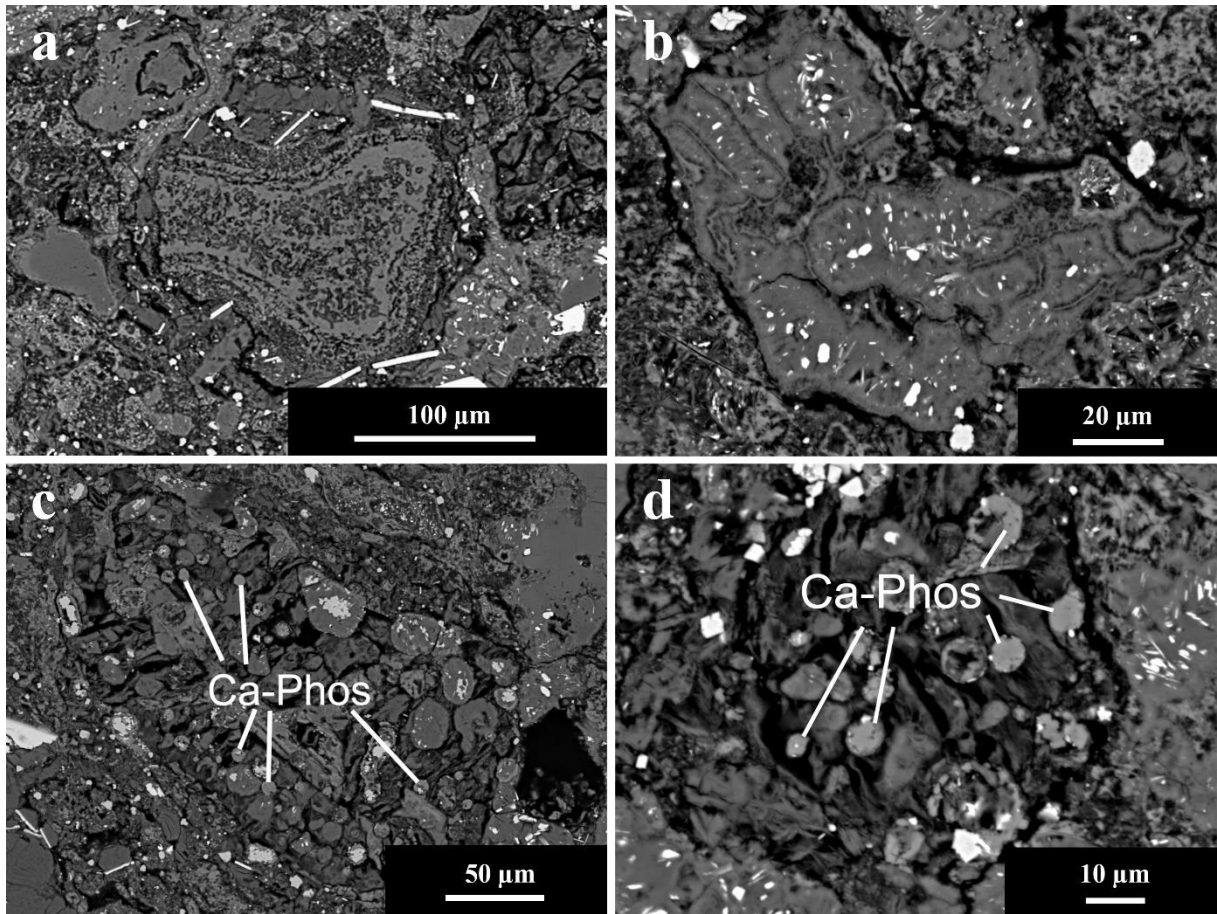
Fig. S3: (a) Irregularly-shaped object in Flensburg resembling a fragment of a CAI or AOA; (b) another irregularly-shaped, phyllosilicate-rich object embedding small sulfide grains; (c) and (d) Ca-phosphate-bearing components in Flensburg. BSE-images.
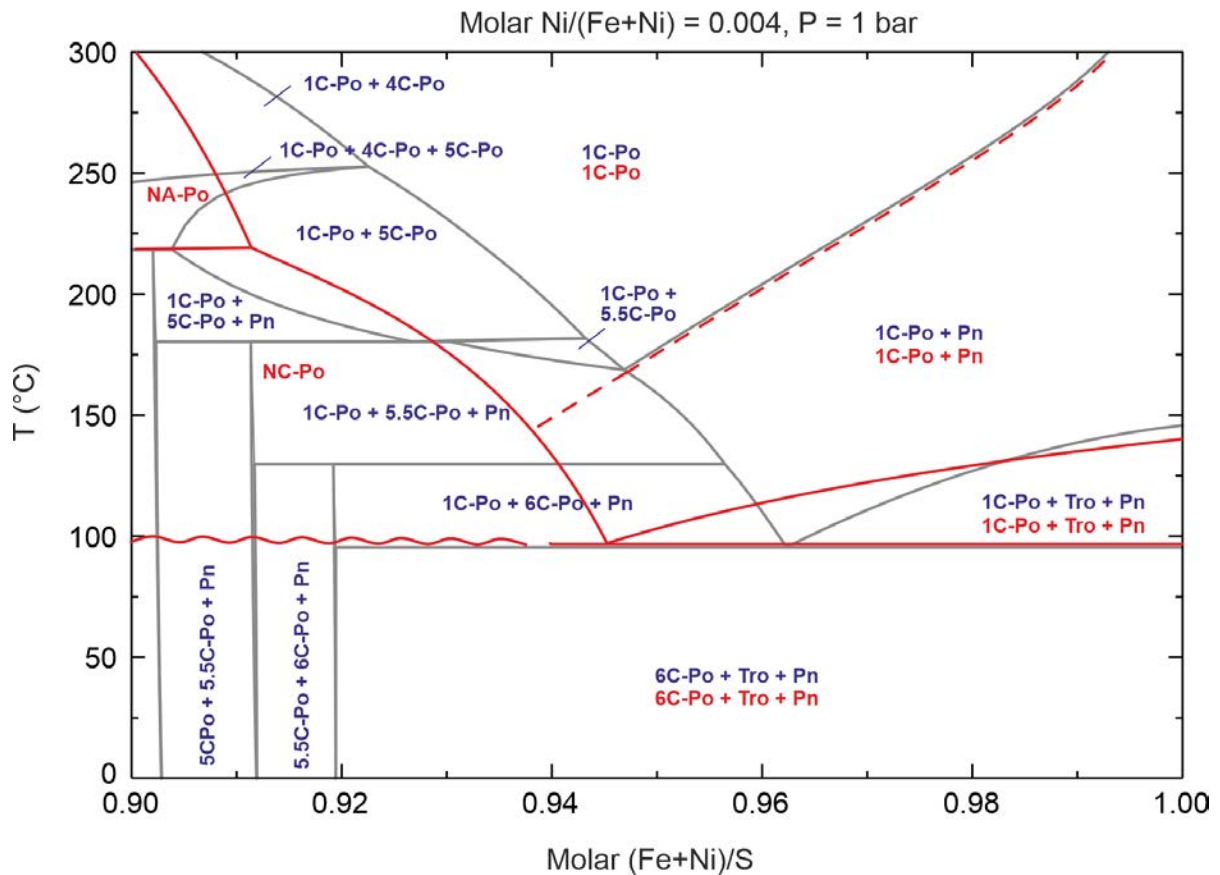
Fig. S4: TX section of the ternary Fe-Ni-S system calculated with the FactSage equilibrium solver incorporating the thermodynamic data of Waldner and Pelton (2004) and the observed mean Ni/(Fe+Ni) ratio of low-Ni iron sulfide in the Flensburg samples. Po: pyrrhotite, Pn: pentlandite, Tro: troilite. The red lines show the tentative Ni-free phase diagram of Nakazawa and Morimoto (1970) based on experimental results. It is distinct as it contains the non-integral NC- and NA-pyrrhotites, for which there are no thermodynamical data available. The use of the 5C and 5.5C (11C) variants of pyrrhotite diminish the stability field of disordered monosulfide solid solution (1C-pyrrhotite) – it is not clear whether these phases are stable or metastable against NC-pyrrhotite. Any monosulfide solid solution formed in equilibrium with pentlandite should have obtained a molar (Fe+Ni)/S ratio on the line separating the 1C-Po and 1C-Po + Pn fields (dashed line). A conservative (low) estimate of the formation temperatures of such a phase would be roughly 150 to 200 °C for intermediate metal/sulfur ratios around 0.95 – temperatures would be larger for larger metal/sulfur ratios. These would produce large amounts of exsolved troilite (>50 vol.%), which is in most cases not observed in the Flensburg low-Ni iron sulfides.
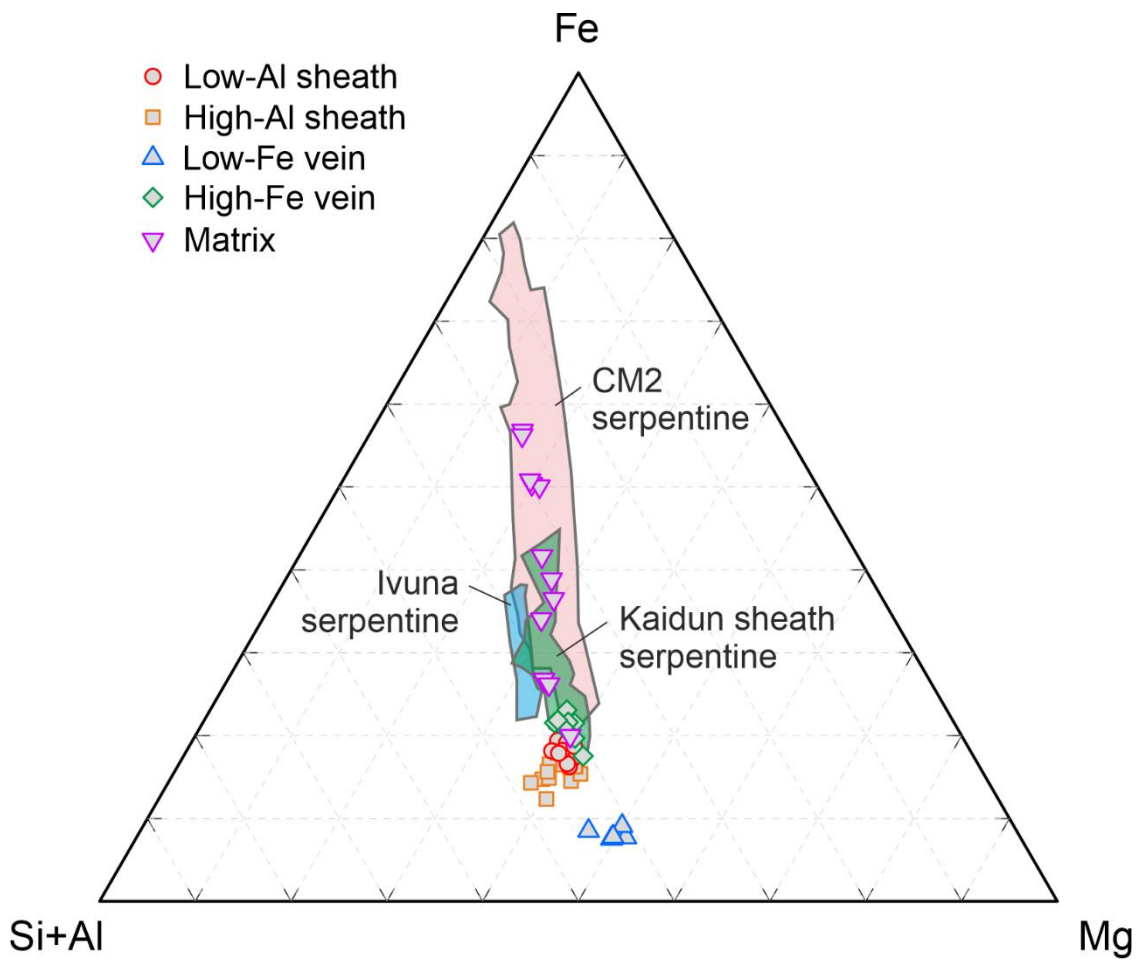
Fig. S5: TEM-EDS compositions (relative mass fractions) of serpentine in Flensburg, subdivided into sheath serpentine (covering euhedral pyrrhotite crystals), vein serpentine (occurring as short veinlets) and matrix serpentine; compare Table 2. For comparison, the fields of phyllosilicates in CM2 chondrites, Kaidun CM1 lithologies, and the Ivuna CI1 chondrite are shown (from Zolensky et al., 1996).
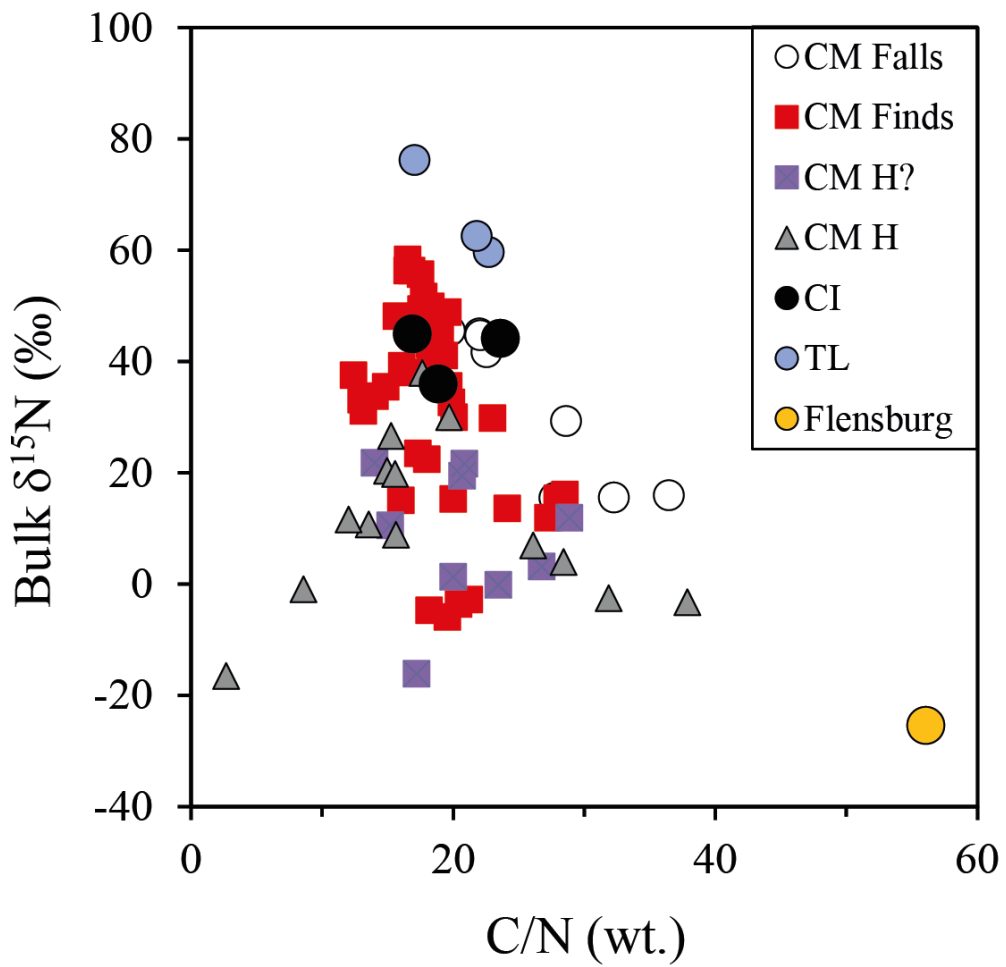
Fig. S6: Bulk δ^{15}N versus C/N-ratio of Flensburg and other type 1-2 carbonaceous chondrites (Alexander et al., 2012, 2013). Flensburg occupies a unique position in this diagram. CM H = heated CM chondrite; CM H? = possibly heated CM; TL = Tagish Lake.
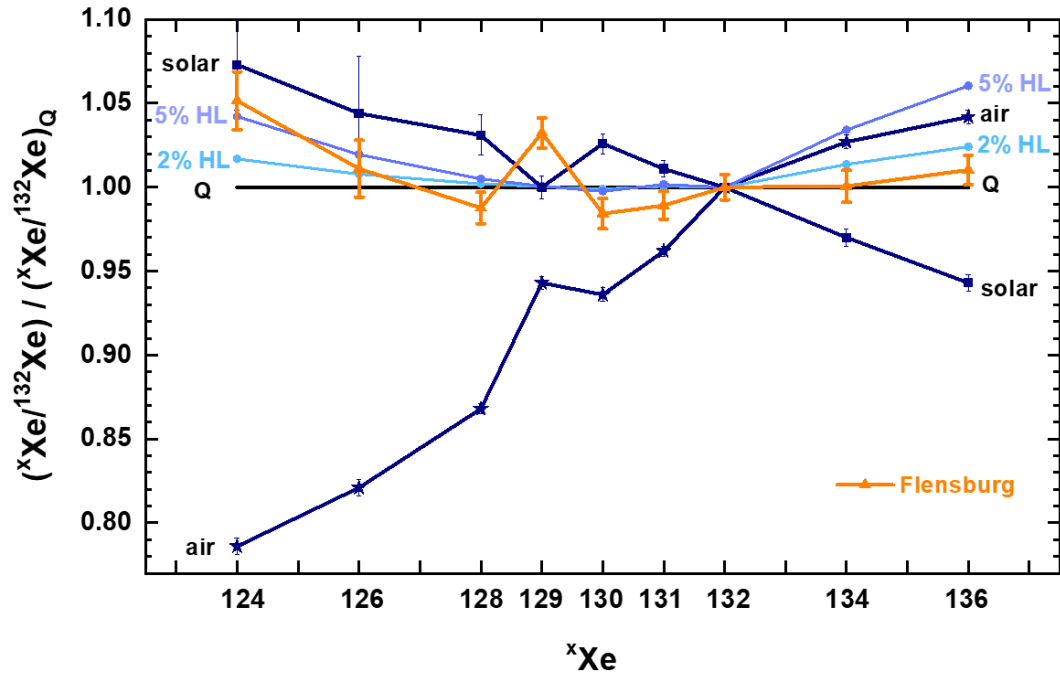
Fig. S7: $^xXe/^{132}Xe$ normalized to Q for all relevant Xe isotopes compared to typical air and solar wind signatures. Additionally, HL-Q mixtures with 5% HL and 2% HL (based on ^{132}Xe) are plotted, showing a possible HL contribution to the signature.
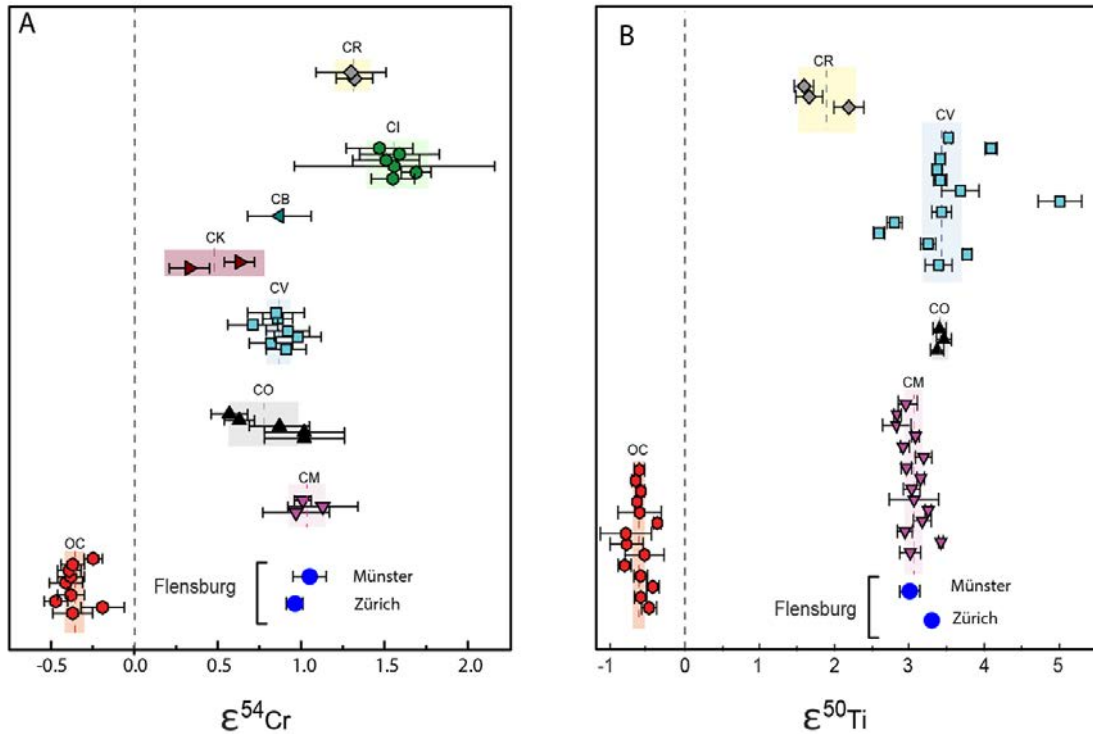
Fig. S8: (a) Chromium isotope compositions of different chondrite groups. Data are from this study, Shukolyukov and Lugmair (2006), Trinquier et al. (2008a,b), and Qin et al. (2010). (b) Titanium isotope compositions of several chondrite groups. Data from this study, Williams (2015), Trinquier et al. (2009), Zhang et al. (2011, 2012), Bischoff et al. (2017), and Burkhardt et al. (2017). Error bars and envelope in both diagrams are 2 SE.
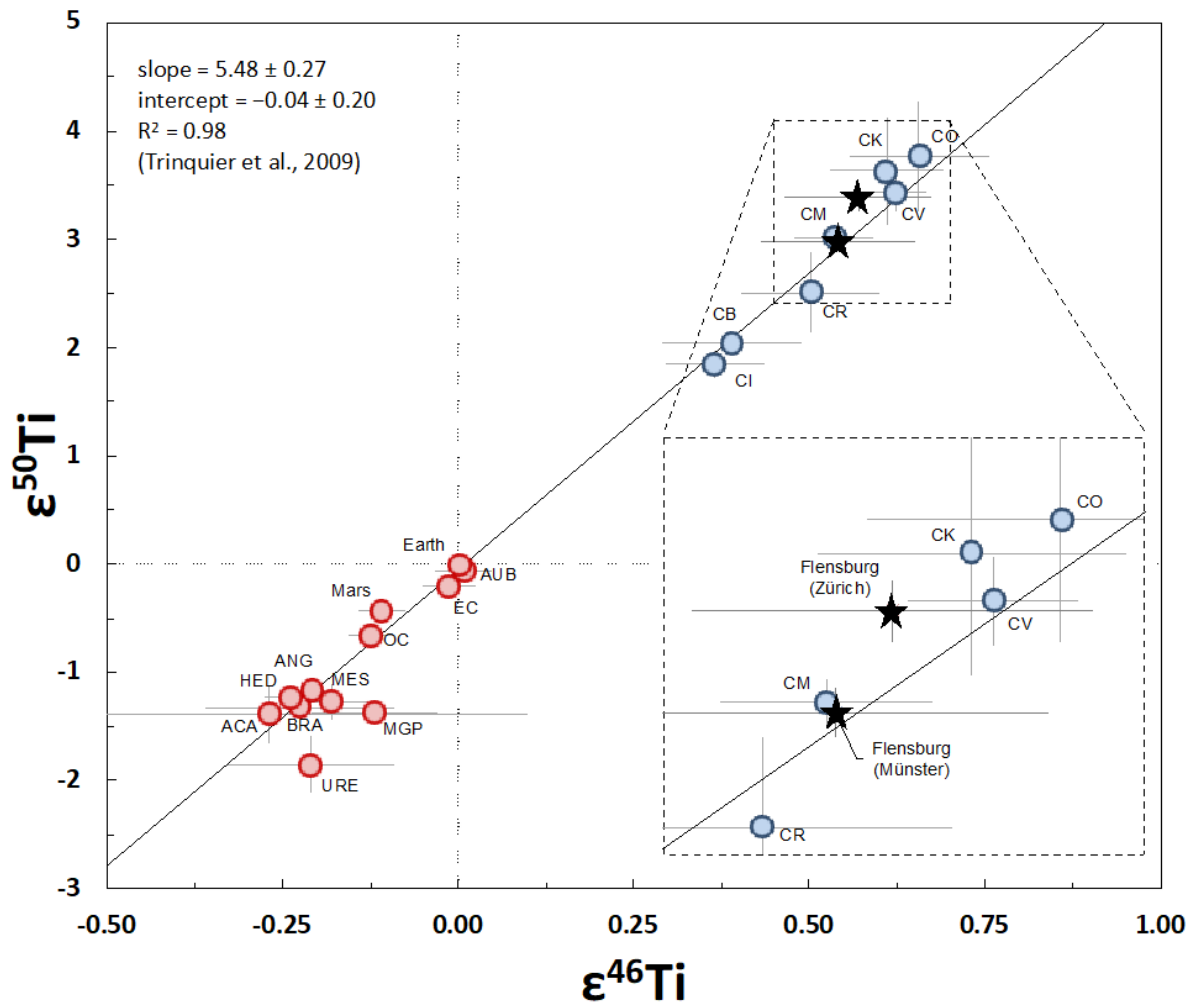
Fig. S9: $\varepsilon^{46}Ti$ vs. $\varepsilon^{50}Ti$ isotope diagram showing the nucleosynthetic Ti isotope composition of Flensburg (black stars) compared to literature data of various meteorite groups (red and blue circles). Uncertainties are Student-t 95% confidence interval (95% CI). The solid black line represents a best-fit regression for bulk meteorite samples, taken from Trinquier et al. (2009). EC: enstatite chondrites, OC: ordinary chondrites, AUB: aubrites, ANG: angrites, ACA: acapulcoites, BRA: brachinites, HED: howardite-eucrite-diogenite group, MGP: main group pallasites, MES: mesosiderites, URE: ureilites. Ti isotope literature data from: Trinquier et al., 2009; Zhang et al., 2011; Zhang et al., 2012; Burkhardt et al., 2017; Gerber et al., 2017; Sanborn et al., 2019; Goodrich et al., 2017.
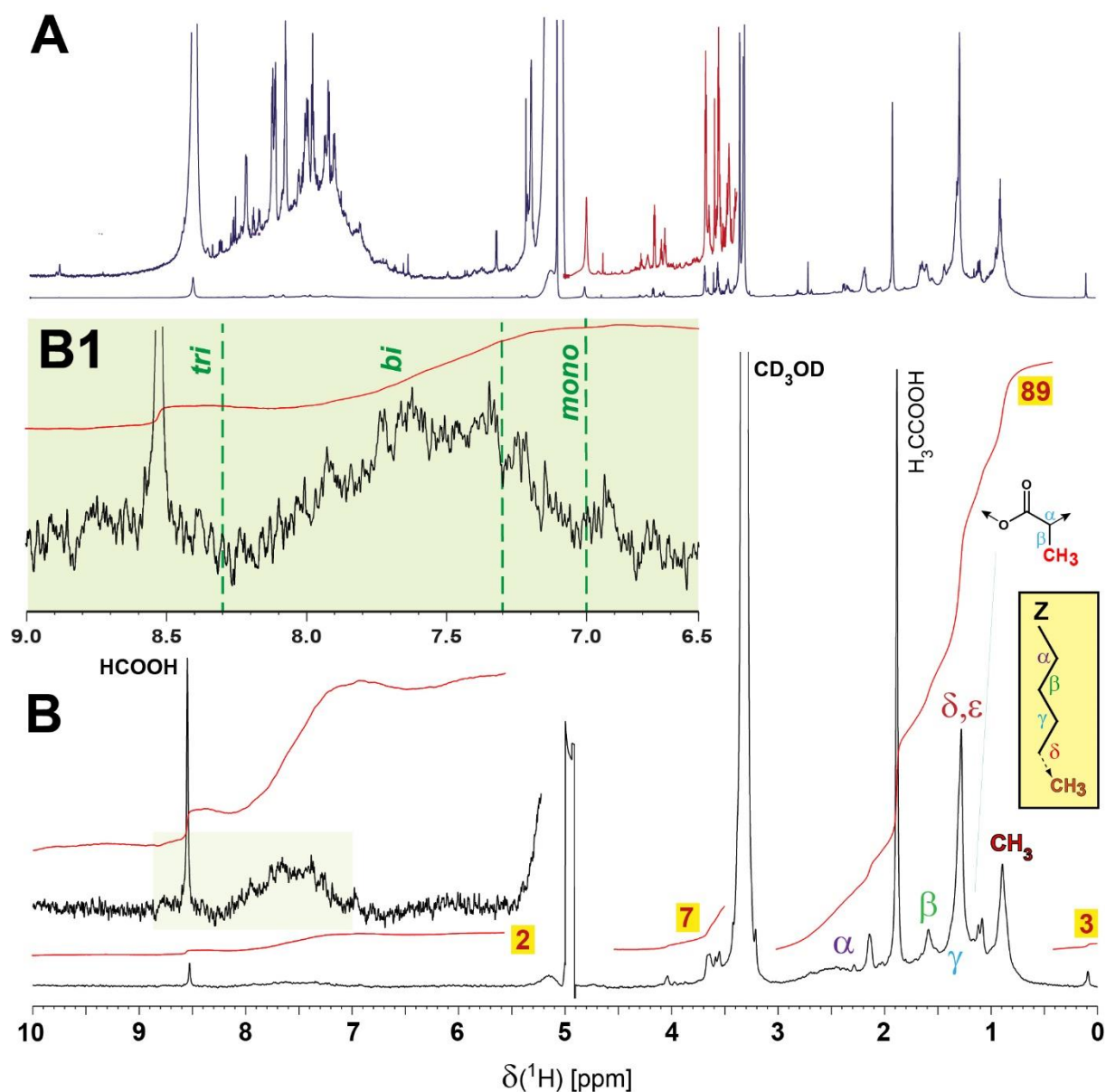
Fig. S10: The ^{1}H NMR spectra (800 MHz; CD_3OD, with solvent suppression) are shown of the Murchison methanolic extract (panel A; same data as in panel A7; Fig. 2, in Hertkorn et al., 2015) and the Flensburg methanolic extract (panel B). Panel B1 shows a section of aromatic ^{1}H NMR resonances $C_{ar}\underline{H}$, shaded in green (cf. also panel B) with common ranges of proton chemical shifts δ_H provided for common polycyclic aromatic rings of different size (Dvorski et al., 2016). Red numbers highlighted in yellow indicate percent ^{1}H NMR section integrals (with exclusion of methanol and water).
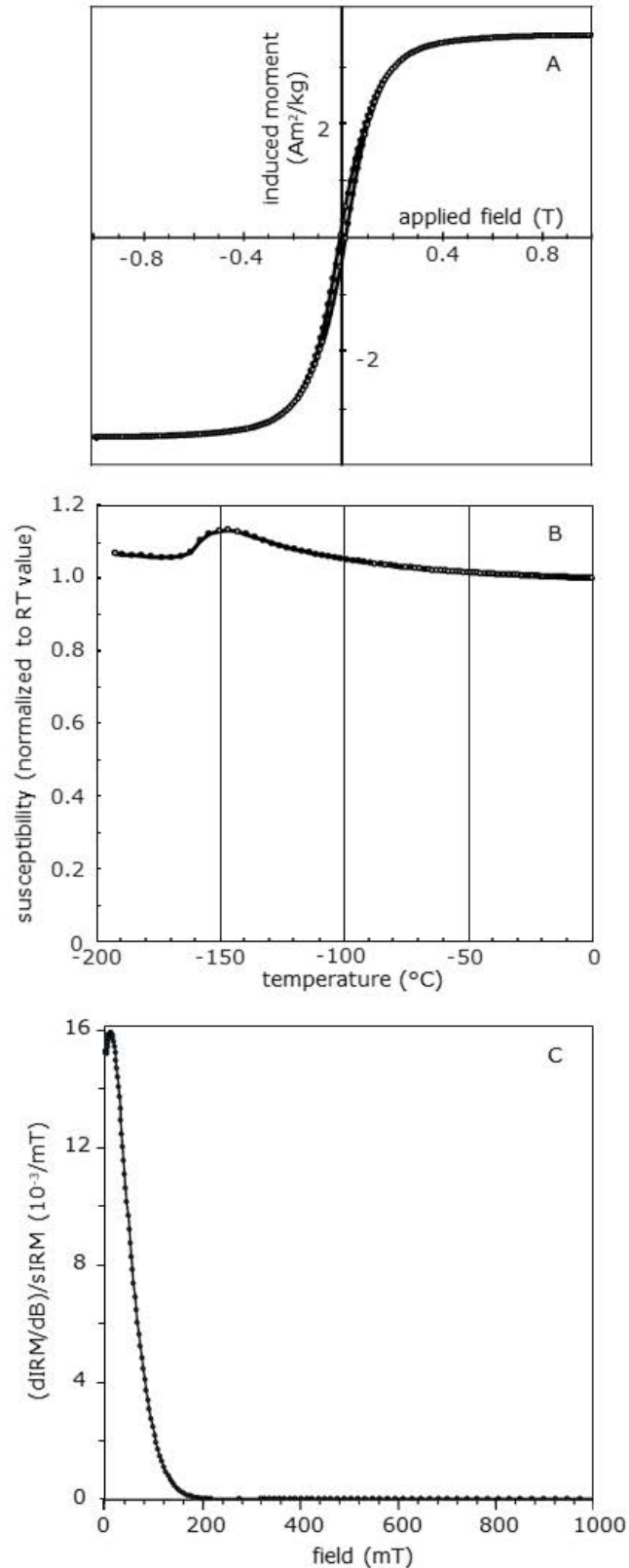
Fig. S11: All measurements were performed on the same 267 mg bulk sample without fusion crust. a) Hysteresis loop. The induced moment is corrected for the paramagnetic susceptibility computed over the 0.9-1T interval. b) Susceptibility as a function of temperature. c) Coercivity spectrum shown as the derivative of the IRM acquired as a function of acquisition field, normalized to the saturation IRM.
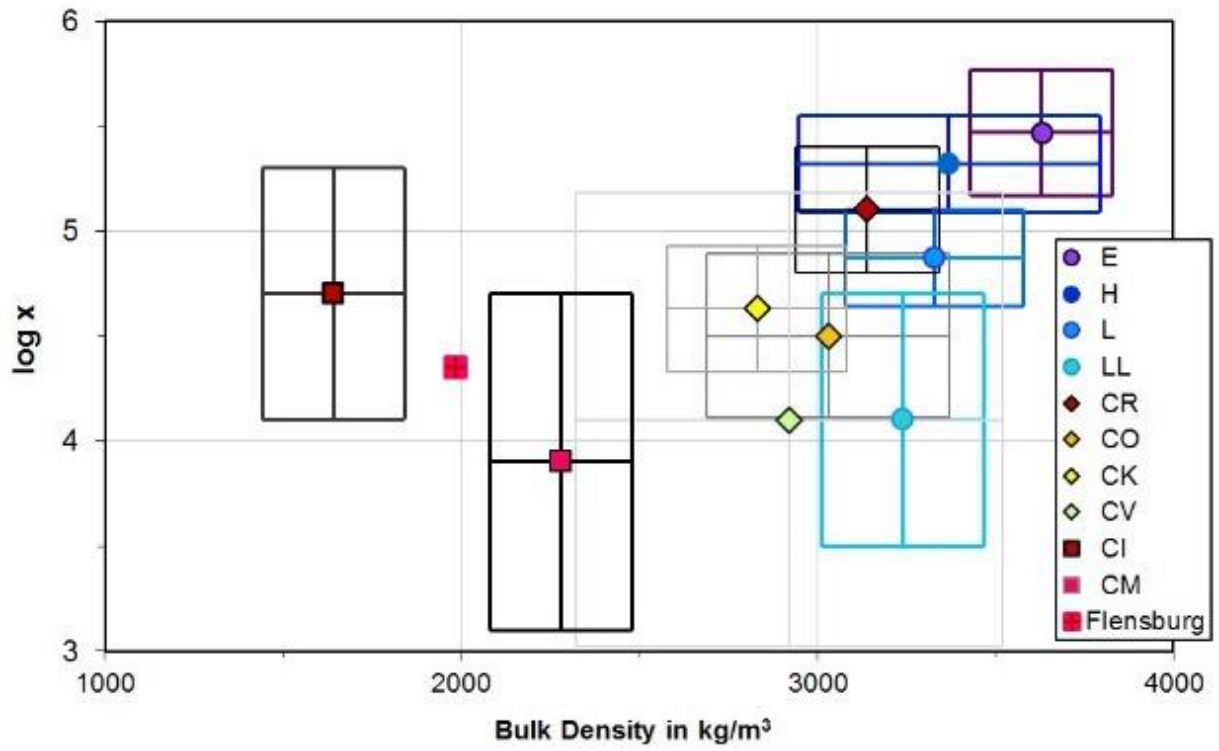
Fig. S12: Illustration of the magnetic susceptibility and density of Flensburg. Flensburg has a density plotting between the range of CI and CM chondrites.
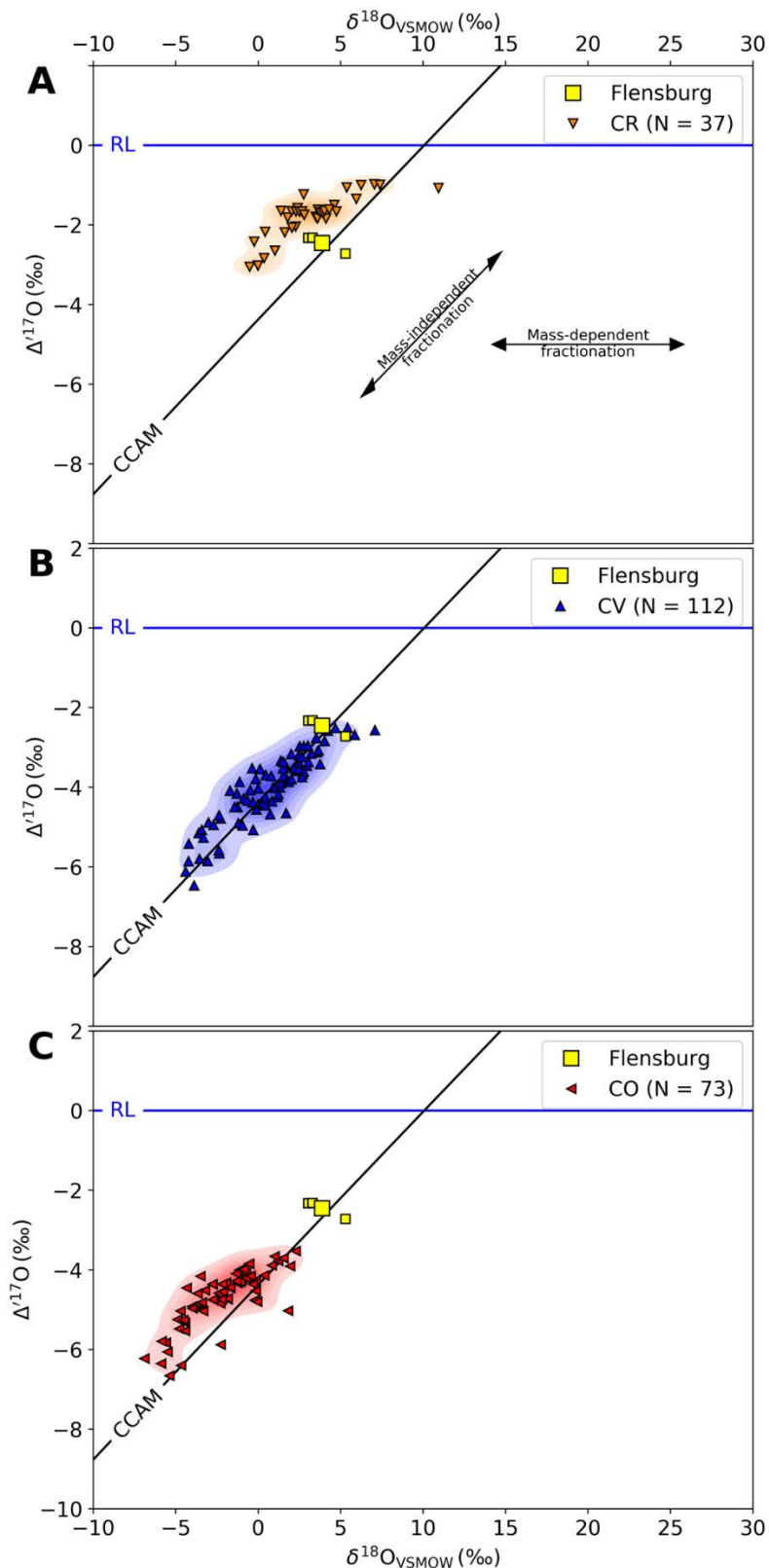
Fig. S13: Plot of the oxygen isotope composition of Flensburg in comparison to published composition of (a) CR chondrites, (b) CV chondrites, and (c) CO chondrites. The Δ'^{17}O data have been calculated using equation 1 (Supplement). The chondrite data have been obtained from the Meteoritical Bulletin database (https://www.lpi.usra.edu/meteor/, access February 2020). The carbonaceous chondrite anhydrous minerals mixing line (CCAM, δ^{17}O = 0.9467 δ^{18}O – 4.3674) is taken from Clayton (2008). RL = reference line.
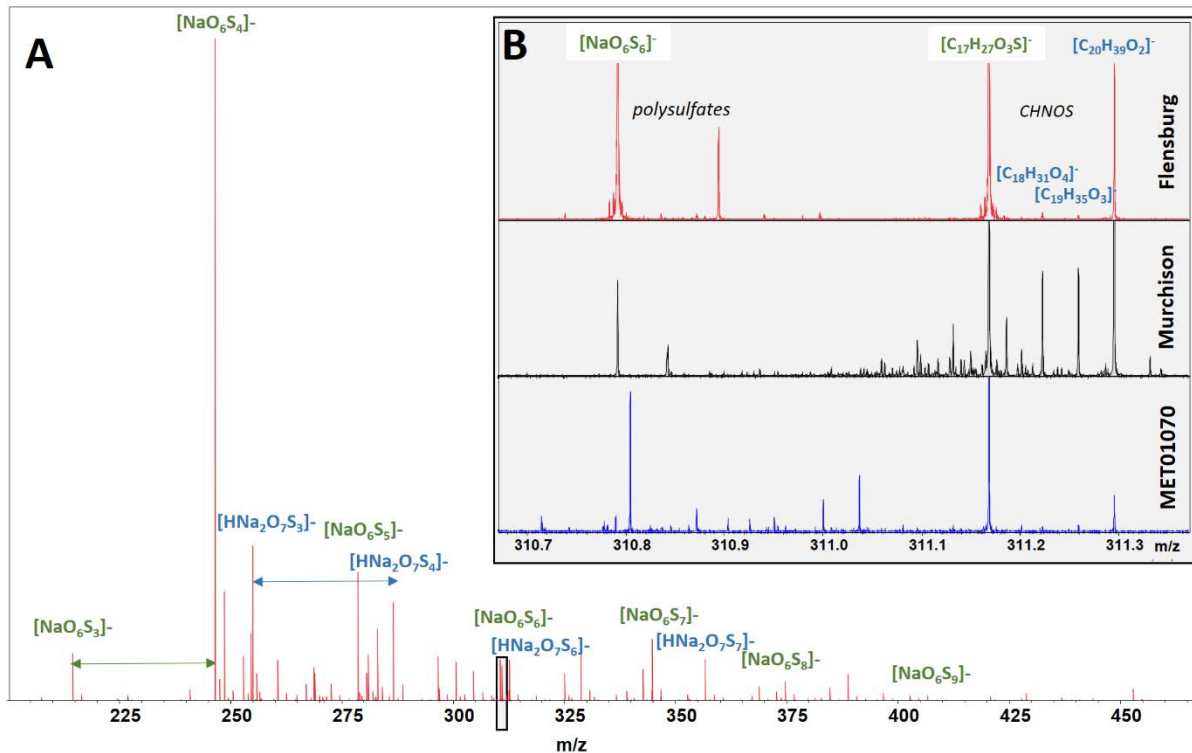
Fig. S14: Electrospray FTICR-MS spectra in the negative mode of the Flensburg methanol extract showing in panel (A), the whole mass range with subsequent intense regular signals corresponding to various polythiol species with up to 9 sulphur atoms. Panel (B) shows the detail of nominal mass 311, indicating the relatively poor chemical diversity of Flensburg compared to Murchison (CM2.5-CM6 breccia; Schmitt-Kopplin et al., 2010); both Flensburg and MET011070 (CM1) have only a few (n<10) and similar mass peaks compared to the high chemical diversity observed in Murchison (n>80).
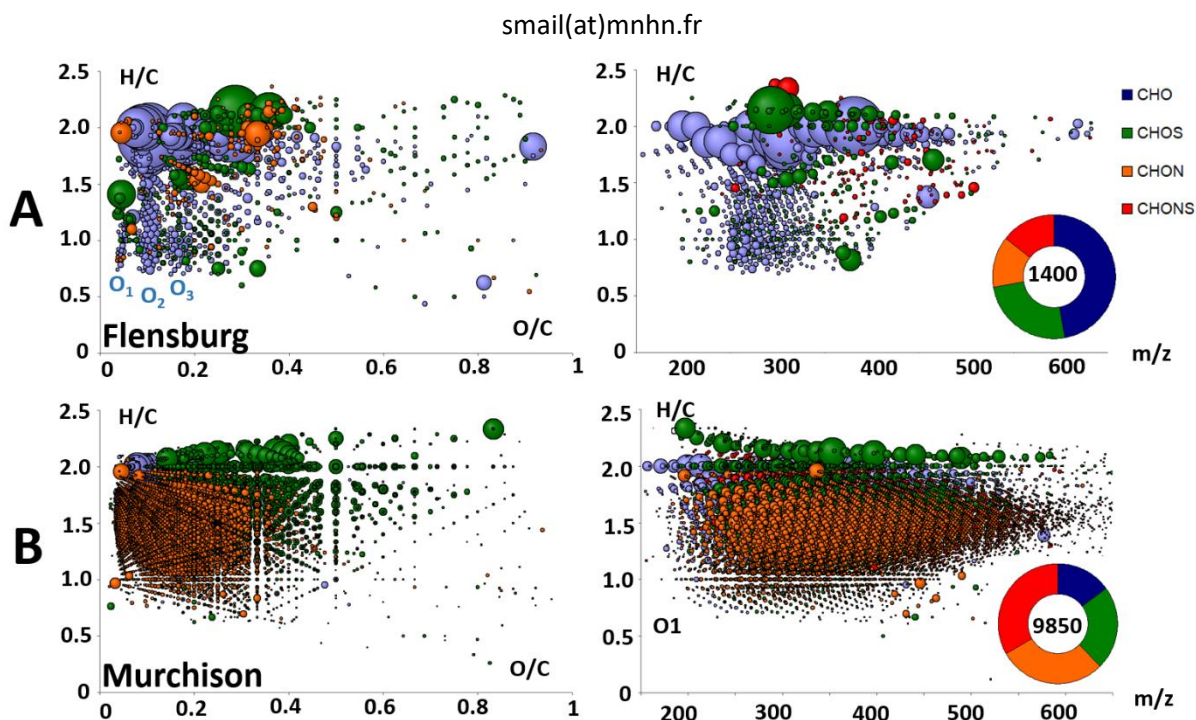
Fig. S15: Van Krevelen diagrams of the Flensburg and Murchison methanol soluble organic matter (SOM) showing the high diversity in S and N chemistry in Murchison (B) compared to Flensburg (A). For Flensburg ~1400 formula (species) are recorded, from which the CHO compounds (blue) are the most abundant, while 9850 species were found for Murchison, in which the respective molecular series decrease according to CHNOS (red) > CHNO (orange) > CHOS (green) > CHO (blue). A remarkable molecular signature of Flensburg SOM is shown representing mono-, di- and tri-oxygenated aromatic hydrocarbons (labelled O_1, O_2 and O_3), respectively), with an H/C range from 1.5 to 0.5, representative of variable extents of aliphatic groups. The bubble size expresses the relative intensity of the signals in the experimental mass spectra.
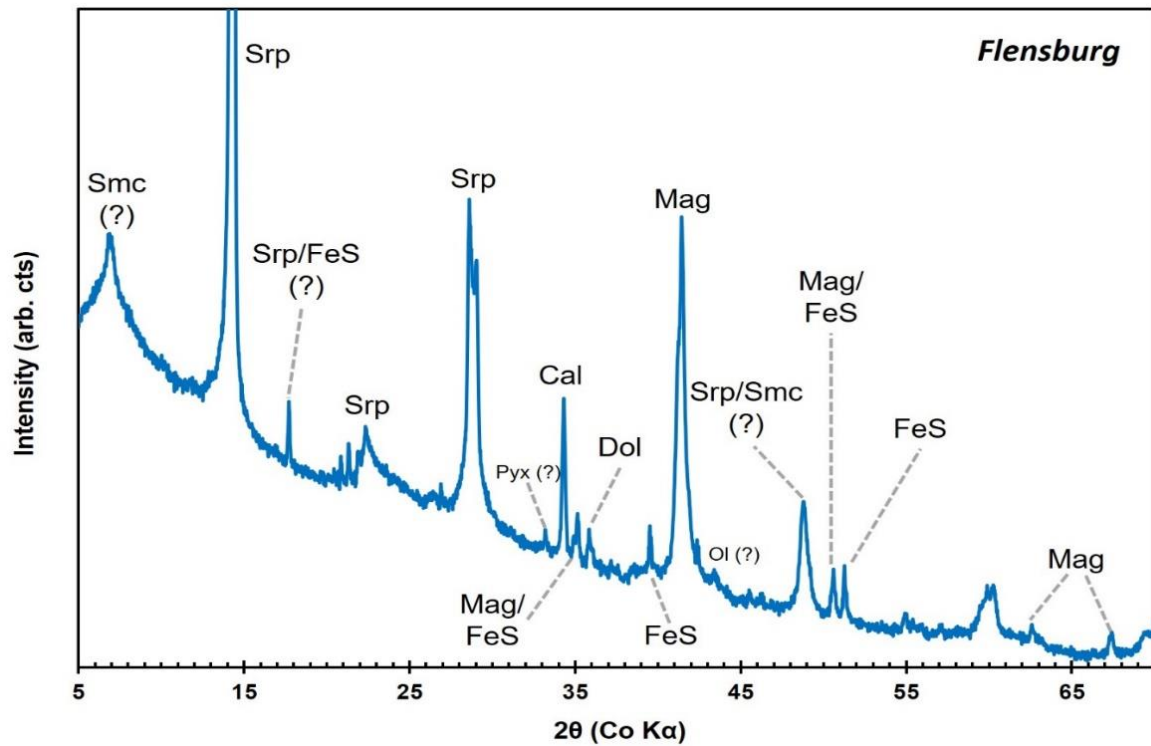
Fig. S16: XRD pattern of Flensburg collected using a PANalytical X'Pert Pro scanning XRD. Minerals identified include phyllosilicates (serpentine (Srp) and possibly smectite (Smc)), magnetite (Mag), Fe-sulphides (troilite and pyrrhotite (FeS)) and carbonates (calcite (Cal) and dolomite (Dol)). Olivine (Ol) and pyroxene (Pyx) may be present in low (<1%) abundances.
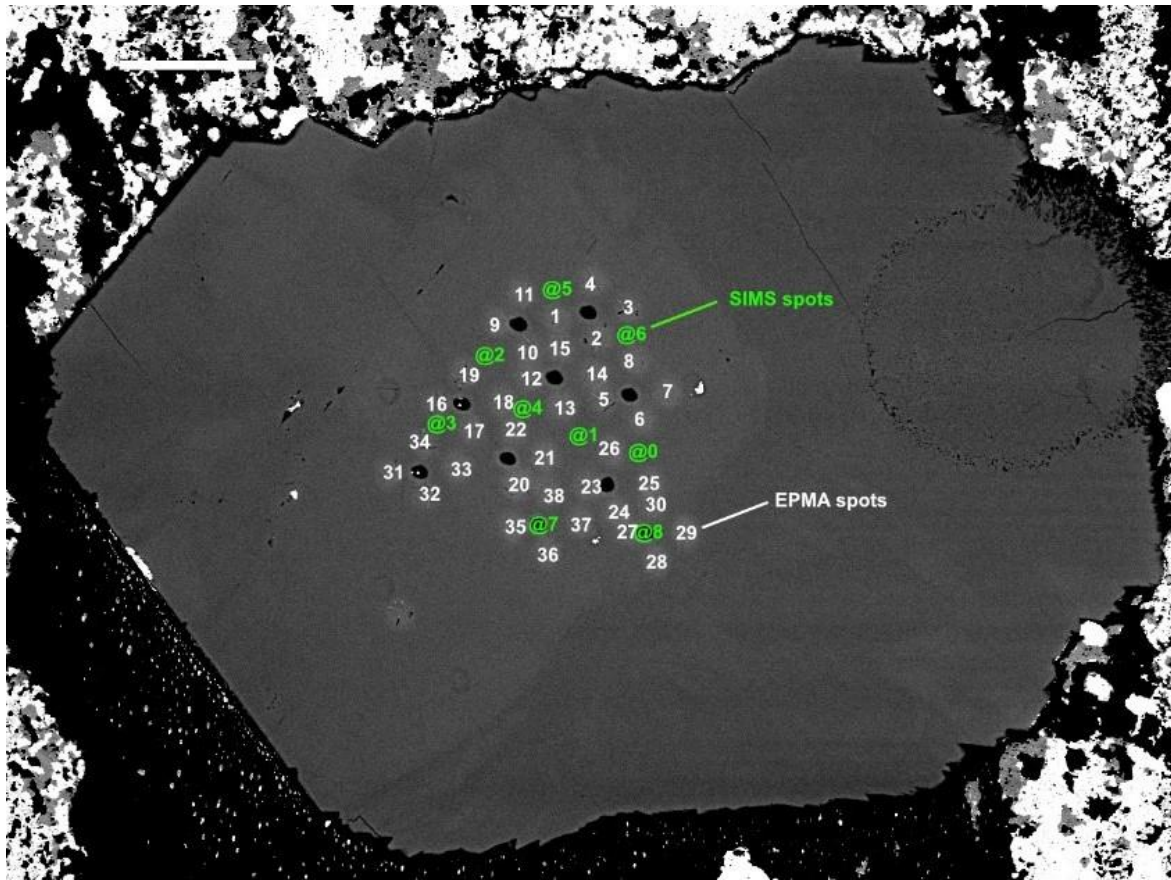
Fig. S17: BSE image of the HIGP calcite showing the analyzed EPMA spots (white numbers) and the SIMS spots (green, @). The analyses are restricted to a homogenous area and analyzed data can be found in Table S5a. The black holes are related to earlier SIMS analyses.

References-Supplement:

Akhmadaliev S., Heller, R., Hanf, D., Rugel, G., and Merchel, S. (2013) The new 6 MV AMS-facility DREAMS at Dresden, *Nucl. Instr. Meth. Phys. Res. B* **294**, 5-10.

Alexander C. M. O'D., Bowden R., Fogel M. L., Howard K. T., Herd C. D. K. and Nittler L. R. (2012) The provenances of asteroids, and their contributions to the volatile inventories of the terrestrial planets. *Science* **337**, 721-723.

Alexander C. M. O'D., Howard K., Bowden R. and Fogel M. L. (2013) The classification of CM and CR chondrites using bulk H, C and N abundances and isotopic compositions. *Geochim. Cosmochim. Acta* **123**, 244-260.

Amiguet E., Reynard, B., Caracas, R., Van de Moortele, B., Hilairet, N., and Wang Y. (2012) Creep of phyllosilicates at the onset of plate tectonics. *Earth and Planetary Science Letters* **345-348**, 142-150.

Barkan E., Musan I., and Boaz L. (2015) High-precision measurements of $\delta^{17}O$ and $^{17}O_{excess}$ of NBS19 and NBS18. *Rapid Communications in Mass Spectrometry* **29**, 2219–2224.

Barrat J.-A., Zanda B., Moynier F., Bollinger C., Liorzou C., and Bayron G. (2012) Geochemistry of CI chondrites: Major and trace elements, and Cu and Zn isotopes. *Geochimica et Cosmochimica Acta* **83**, 79-92.

Barrat J.-A., Rouxel O., Wang K., Moynier F., Yamaguchi A., Bischoff A., and Langlade J. (2015) Early stages of core segregation recorded by Fe isotopes in an asteroidal mantle. *Earth Planet. Sci. Lett.* **419**, 93–100.

Barrat J.-A., Gillet, P., Dauphas, N., Bollinger, C., Etoubleau, J., Bischoff, A., and Yamaguchi A. (2016) Evidence from Tm anomalies for non-CI refractory lithophile element proportions in terrestrial planets and achondrites. *Geochim. Cosmochim. Acta.* **176**, 1-17.

Bischoff A., Barrat J.-A., Bauer, K., Burkhardt, C., Busemann, H., Ebert, S., Gonsior, M., Hakenmüller, J., Haloda, J., Harries, D., Heinlein, D., Hiesinger, H., Hochleitner, R., Hoffmann, V., Kaliwoda, M., Laubenstein, M., Maden, C., Meier, M. M. M., Morlok, A., Pack, A., Ruf, A., Schmitt-Kopplin, P., Schönbächler, M., Steele, R. C. J., Spurny, P., and Wimmer K. (2017). The Stubenberg meteorite - an LL6 chondrite fragmental breccia recovered soon after precise prediction of the strewn field. *Meteoritics & Planetary Science* **52**, 1683-1703.

Bischoff A., Barrat J.-A., Berndt J., Borovicka J., Burkhardt C., Busemann H., Hakenmüller J., Heinlein D., Hertzog J., Kaiser J., Maden C., Meier M. M. M., Morino P., Pack A., Patzek M., Reitze M. P., Rüfenacht M., Schmitt-Kopplin P., Schönbächler M., Spurny P., Weber I., Wimmer K. and Zikmund T. (2019) The Renchen L5-6 chondrite breccia – the first confirmed meteorite fall from Baden-Württemberg (Germany). *Geochemistry – Chemie der Erde* **79**, 125525.

Brand A.B., Coplen T.B., Vogl J., Rosner M., and Prohasa T. (2014) Assessment of international reference materials for isotope-ratio analysis (IUPAC Technical Report). *Pure and Applied Chemistry* **86**(3), 425–467.

Brennecka G.A., Borg, L.E., Romaniello, S.J., Souders, A.K., Shollenberger, Q.R., Marks, N.E., and Wadhwa M. (2017) A renewed search for short-lived ^{126}Sn in the early Solar System: Hydride generation MC-ICPMS for high sensitivity Te isotopic analysis. *Geochimica et Cosmochimica Acta* **201**, 331-344.

Burkhardt C., Dauphas N., Tang H., Fischer-Gödde M., Qin L., Chen J. H., Rout S. S., Pack A., Heck P. R. and Papanastassiou D. A. (2017) In search of the Earth-forming reservoir: Mineralogical, chemical, and isotopic characterizations of the ungrouped achondrite NWA 5363/NWA 5400 and selected chondrites. *Meteorit. Planet. Sci.* **52**, 807–826.

Clayton R. N. (2008) Oxygen isotopes in the early Solar System - A historical perspective. In: MacPherson *et al.* (Eds.) *Oxygen in the solar system*. vol. **68**, American Mineralogical Society (Washington), p. 5-14.

Consolmagno G. J., Britt D. T., and Macke R. J. (2008) The significance of meteorite density and porosity. *Chemie der Erde* **68**, 1-29.

Donohue P.H., Huss G.R., and Nagashima K. (2019) New synthetic carbonates for investigation of manganese-chromium chronology by secondary ion mass spectrometry. *Lunar and Planetary Science Conference* **50**, #1959.

Dvorski S., Gonsior M., Hertkorn N., Uhl J., Müller H., Griebler C., and Schmitt-Kopplin P. (2016) Geochemistry of dissolved organic matter in a spatially highly resolved groundwater petroleum hydrocarbon plume cross-section. *Environmental Science & Technology* **50**(11), 5536–5546.

Fehr M.A., Rehkämper M., and Halliday A.N. (2004) Application of MC-ICPMS to the precise determination of tellurium isotope compositions in chondrites, iron meteorites and sulfides. *International Journal of Mass Spectrometry* **232**, 83-94.

Finocchi F. and Gail H.P. (1997) Chemical reactions in protoplanetary accretion disks. III. The role of ionisation processes. *Astronomy and Astrophysics* **327**, 825-844.

Gerber S., Burkhardt C., Budde G., Metzler K. and Kleine T. (2017) Mixing and transport of dust in the early solar nebula as inferred from titanium isotope variations among chondrules. *Astrophys. J.* **841**, L17.

Goodrich C. A., Kita N. T., Yin Q.-Z., Sanborn M. E., Williams C. D., Nakashima D., Lane M. D. and Boyle S. (2017) Petrogenesis and provenance of ungrouped achondrite Northwest Africa 7325 from petrology, trace elements, oxygen, chromium and titanium isotopes, and mid-IR spectroscopy. *Geochim. Cosmochim. Acta* **203**, 381–403.

Harries D. and Zolensky M.E. (2016) Mineralogy of iron sulfides in CM1 and CI1 lithologies of the Kaidun breccia: Records of extreme to intense hydrothermal alteration. *Meteoritics & Planetary Science* **51**, 1096–1109.

Hertkorn N., Harir M., and Schmitt-Kopplin Ph. (2015) Nontarget analysis of Murchison soluble organic matter by high-field NMR spectroscopy and FTICR mass spectrometry. *Magnetic Resonance Chemistry* **53**, 754-768.

Hilairet N., Reynard B., Wang Y., Daniel I., Merkel S., Nishiyama N., and Petitgirard S. (2007) High-pressure creep of serpentine, interseismic deformation, and initiation of subduction. *Science* **318**, 1910-1913.

Jull A. J. T., Cloudt S. and Cielaszyk E. (1998) ^{14}C terrestrial ages of meteorites from Victoria Land, Antarctica and the infall rate of meteorites. In Grady, M. M. et al. (eds) *Meteorites: Flux with time and impact effects.* Geological Society, London, Special Publication **140**, 75-91.

King A. J., Schofield P. F., Howard K. T., and Russell S. S. (2015) Modal mineralogy of CI and CI-like chondrites by Xray diffraction. *Geochimica et Cosmochimica Acta* **165**, 148–160.Kita N. T., Yin Q. Z., MacPherson G. J., Ushikubo T., Jacobsen B., Nagashima K., Kurashi E., Krot A., and Jacobsen S. B. (2013) ^{26}Al-^{26}Mgisotope systematics of the first solids in the early solar system. *Meteoritics and Planetary Science* **48**, 1383-1400.

Köhler M., Degering, D., Laubenstein, M., Quirin, P., Lambert, M.-O., Hult, M., Arnold, D., Neumaier, S., and Reyss J.-L. (2009) A new low-level γ-ray spectrometry system for environmental radioactivity at the underground laboratory Felsenkeller. *Applied Radiation and Isotopes* **67**, 736-740.

Korschinek G., Bergmaier A., Faestermann T., Gerstmann U. C., Knie K., Rugel G., Wallner A., Dillmann I., Dollinger G., Lierse von Gostomski Ch., Kossert K., Maiti M., Poutivtsev M., and Remmert A. (2010) A new value for the half-life of ^{10}Be by heavy-ion elastic recoil detection and liquid scintillation counting. *Nucl. Inst. Meth. Phys. Res.* **B 268**, 187-191.

Leya I. and Masarik, J. (2009) Cosmogenic nuclides in stony meteorites revisited. *Meteoritics & Planetary Science* **44**, 1061-1086.

Leya I., J.-C. David, T. Faestermann, M. Froehlich, N. Kivel, D. Koll, G. Korschinek, S. McIntyre, S. Merchel, S. Pavetich, G. Rugel, D. Schumann, T. Smith, and Wallner A. (2020) ^{53}Mn and ^{60}Fe in iron meteorites - new data and model calculations, *Meteorit. Planet. Sci.* **55**, 818-831.

Ludwig F., Wagner, L., Al-Abdullah, T., Barnaföldi, G.G., Bemmerer, D., Degering, D., Schmidt, K., Suranyi, G., Szücs, T., and Zuber K. (2019) The muon intensity in the Felsenkeller shallow underground laboratory. *Astroparticle Physics* **112**, 24-34.

Meija J., Coplen, T.B., Berglund, M., Brand, W.A., De Bièvre, P., Gröning, M., Holden, N.E., Irrgeher, J., Loss, R.D., Walczyk, T., and Prohaska T. (2016) Isotopic compositions of the elements 2013 (IUPAC Technical Report). Pure and Applied Chemistry 88(3): 293–306.

Merchel S. and Herpers U. (1999) An update on radiochemical separation techniques for the determination of long-lived radionuclides via accelerator mass spectrometry. *Radiochim. Acta* **84**, 215-219.

Meteoritical Bulletin Database (https://www.lpi.usra.edu/meteor)

Millet M.-A. and Dauphas N. (2014) Ultra-precise titanium stable isotope measurements by double-spike high resolution MC-ICP-MS. *J. Anal. At. Spectrom.* **29**, 1444-1458.

Nakazawa H. and Morimoto N. (1970) Pyrrhotite phase relations below 320 C. *Proceedings of the Japan Academy* **46**, 678–683.

Neumann W. and Kruse A. (2019) Differentiation of Enceladus and retention of a porous core. *The Astrophysical Journal* **882**, 47.

Neumann W., Breuer D., and Spohn T. (2014) Modelling of compaction in planetesimals. *Astronomy and Astrophysics* **567**, A120.

Neumann W., Breuer D., and Spohn T. (2015) Modelling the internal structure of Ceres: Coupling of accretion with compaction by creep and implications for the water-rock differentiation. *Astronomy and Astrophysics* **584**, A117.

Neumann W., Jaumann R., Castillo-Rogez J., Raymond C., and Russell C.T. (2020) Ceres' partial differentiation: undifferentiated crust mixing with a water-rich mantle. *Astronomy and Astrophysics* **633**, A117.

Niese S., Köhler M., and Gleisberg B. (1998) Low-level counting techniques in the underground laboratory "Felsenkeller" in Dresden. *Journal of Radioanalytical and Nuclear Chemistry* **233**, 167-172.

Norris T. L., Gancarz A. J., Rokop D. J., and Thomas K. W. (1983) Half-life of ^{26}Al. *Proc. of the 14th Lunar and Planetary Science Conference, Journal of Geophysical Research Suppl.* **8**, B331-B333.

Pack A., Tanaka R., Hering M., Sengupta S., Peter, S., and Nakamura E. (2016) The oxygen isotope composition of San Carlos olivine on VSMOW2-SLAP2 scale, *Rapid Communications in Mass Spectrometry* **30**: 1495-1504.

Passey B. H., Hu H., Ji H., Montanari S., Li S., Henkes G.A., and Levin N.E. (2014) Triple oxygen isotopes in biogenic and sedimentary carbonates. *Geochimica et Cosmochimica Acta* **141**, 1–25.

Paul M., Ahmad I., and Kutschera W. (1991) Half-life of ^{41}Ca. *Z. Phys. A - Hadrons and Nuclei* **340**, 249-254.

Peters S.T., Alibabaie, N., Pack, A., McKibbin, S.J., Raeisi, D., Nayebi, N., Torab, F., Ireland, T., and Lehmann B. (2020) Triple oxygen isotope variations in magnetite from iron-oxide deposits, central Iran, record magmatic fluid interaction with evaporite and carbonate host rocks. *Geology* **48**, 211-215.

Popova O. P., P. Jenniskens, V. Emel'yanenko, A. Kartashova, E. Biryukov, S. Khaibrakhmanov, V. Shuvalov, Y. Rybnov, A. Dudorov, V. I. Grokhovsky, D. Badyukov, Q.-Z. Yin, P. S. Gural, J. Albers, M. Granvik, L. G. Evers, J. Kuiper, V. Kharlamov, A. Solovyov, Y. S. Rusakov, S.

Korotkiy, I. Serdyuk, A. V. Korochantsev, M. Y. Larionov, D. Glazachev, A. E. Mayer, G. Gisler, S. V. Gladkovsky, J. Wimpenn, M. E. Sanborny, A. Yamakawa, K. L. Verosub, D. J. Rowland, S. Roeske, N. W. Botto, J. M. Friedrich, M. E. Zolensky, L. Le, , K. Ziegler, T. Nakamura, I. Ahn, J. Ik Lee, Q. Zhou, X.-H. Li, Q.-L. Li, Y. Liu, G.-Q. Tang, T. Hiroi, D. Sears, I. A. Weinstein, A. S. Vokhmintsev, A. V. Ishchenko, Ph. Schmitt-Kopplin, N. Hertkorn, K. Nagao, M. K. Haba, M. Komatsu, and T. Mikouchi, (the Chelyabinsk Airburst Consortium) (2013) Chelyabinsk airburst, damage assessment, meteorite recovery, and characterization. *Science* **342,** 1069-1073.

Qin L., Alexander C. M. O., Carlson R. W., Horan M. F., and Yokoyama T. (2010) Contributors to chromium isotope variation of meteorites. *Geochimica et Cosmochimica Acta* **74**, 1122–1145.

Rugel G., Pavetich S., Akhmadaliev S., Enamorado Baez S.M., Scharf A., Ziegenrücker R., and Merchel S. (2016) The first four years of the AMS-facility DREAMS: Status and developments for more accurate radionuclide data, *Nucl. Instr. Meth. Phys. Res.* **B 370**, 94-100.

Sanborn M. E., Wimpenny J., Williams C. D., Yamakawa A., Amelin Y., Irving A. J. and Yin Q.-Z. (2019) Carbonaceous achondrites Northwest Africa 6704/6693: Milestones for early Solar System chronology and genealogy. *Geochim. Cosmochim. Acta* **245**, 577–596.

Schmitt-Kopplin Ph., Gabelica, Z., Gougeon, R.D., Fekete, A., Kanawati, B., Harir, M., Gebefuegi, I., Eckel, G., and Hertkorn N. (2010) High molecular diversity of extraterrestrial organic matter in Murchison meteorite revealed 40 years after its fall. *PNAS*, **107**(7), 2763-2768.

Schumann D., Kivel N., and Dressler R. (2019) Production and characterization of ^{60}Fe standards for Accelerator Mass Spectrometry, *PloS ONE* **14**(6), e0219039.

Schwenn M. B. and Goetze C. (1978) Creep of olivine during hot pressing. *Tectonophysics* **48**, 41-60.

Sessions A. L., Burgoyne T. W., and Hayes J. M. (2001) Determination of the H-3 factor in hydrogen isotope ratio monitoring mass spectrometry. *Analytical Chemistry* **73**, 200-207.

Sharp Z.D., Gibbons, J.A., Atudorei, V., Pack, A., Sengupta, S., Shock, E.L., and Knauth L.P. (2016) A calibration of the triple oxygen isotope fractionation in the SiO$_2$–H$_2$O system and applications to natural samples. *Geochimica et Cosmochimica Acta* **186**, 105-119.

Shukolyukov A., and Lugmair G. W. (2006) Manganese–chromium isotope systematics of carbonaceous chondrites. *Earth and Planetary Science Letters* **250**, 1-2, 200-213.

Śliwiński M. G., Kitajima K., Kozdon R., Spicuzza M. J., Fournelle J. H., Denny A., and Valley J. W. (2016a) Secondary ion mass spectrometry bias on isotope ratios in dolomite–ankerite, Part I: d^{18}O matrix effects. *Geostandards and Geoanalytical Research* **40**, 157–172.

Śliwiński M. G., Kitajima K., Kozdon R., Spicuzza M. J., Fournelle J. H., Denny A., and Valley J. W. (2016b) Secondary ion mass spectrometry bias on isotope ratios in dolomite–ankerite, Part II: d^{13}C matrix effects. *Geostandards and Geoanalytical Research* **40**, 173–184.

Steele R.C.J., Heber V.S., and McKeegan K.D. (2017) Matrix effects on the relative sensitivity factors for manganese and chromium during ion microprobe analysis of carbonate: Implications for early Solar System chronology. *Geochimica et Cosmochimca Acta* **201**, 245–259.

Tang H. and Dauphas N. (2012) Abundance, distribution, and origin of ^{60}Fe in the solar protoplanetary disk. *Earth and Planetary Science Letters* **359**, 248-263.

Trinquier A., Elliott T., Ulfbeck D., Coath C., Krot A. N. and Bizzarro M. (2009) Origin of nucleosynthetic isotope heterogeneity in the solar protoplanetary disk. *Science* **324**, 374–376.

Trinquier A., Birck J. L., Allègre C. J., Göpel C., and Ulfbeck D. (2008a) ^{53}Mn–^{53}Cr systematics of the early Solar System revisited. *Geochimica et Cosmochimica Acta* **72**, 5146–5163.

Trinquier A., Birck J.-L., and Allègre C. J. (2008b) High-precision analysis of chromium isotopes in terrestrial and meteorite samples by thermal ionization mass spectrometry. *Journal of Analytical Atomic Spectrometry* **23**, 1565-1574.

Tyra M., Brearley A., and Yunbin G. (2016) Episodic carbonate precipitation in the CM chondrite ALH 84049: An ion microprobe analysis of O and C isotopes. *Geochimica et Cosmochimica Acta* **175**, 195–207.

Van Schmus W. R. (1995) Global Earth Physics. AGU Reference Shelf 1 (American Geophysical Union). Chapter A Handbook on Physical Constants. pp. 283-291.

Vermeesch P. (2018) IsoplotR: A free and open toolbox for geochronology. *Geoscience Frontiers* **9**, 1479–1493

Waldner P. and Pelton A.D. (2004) Critical thermodynamic assessment and modeling of the Fe-Ni-S system. *Metall. and Materials Trans. B* **35**, 897–907.

Wallner A., Bichler, M., Buczak, K., Dressler, R., Fifield, L. K., Schumann, D., Sterba, J. H., Tims, S. G., Wallner, G., and Kutschera W. (2015) Settling the half-life of ^{60}Fe: fundamental for a versatile astrophysical chronometer. *Physical Review Letters* **114**, 041101.

Wallner A., Feige J., Kinoshita N., Paul M., Fifield L. K., Golser R., Honda M., Linnemann U., Matsuzaki H., Merchel S., Rugel G., Tims S. G., Steier P., Yamagata T., and Winkler S. R. (2016) Recent near-Earth supernovae probed by global deposition of interstellar radioactive ^{60}Fe. *Nature* **532,** 69–72.

Weber I., Morlok, A., Grund, T., Bauch, K. E., Hiesinger, H., Stojic, A., Grumpe, A., Wöhler, C., Klemme, S., Sohn, M., Martin, D. J. P., and Joy K. H. (2018) A mid-infrared reflectance database in preparation for space missions. *Lunar Planet. Sci. Conf.* **48**, #1430.

Williams N. H. (2015) *The origin of titanium isotopic anomalies within solar system material.* PhD thesis, University of Manchester.

Wostbrock J. A., Cano E. J., and Sharp Z. D. (2020) An internally consistent triple oxygen isotope calibration of standards for silicates, carbonates and air relative to VSMOW2 and SLAP2. *Chemical Geology* **533**: 119432.

Yamakawa A., Yamashita K., Makishima A., and Nakamura E. (2009) Chemical separation and mass spectrometry of Cr, Fe, Ni, Zn, and Cu in terrestrial and extraterrestrial materials using thermal ionization mass spectrometry. *Anal.Chem* **8**, 9787–9794.

Zhang J., Dauphas N., Davis A. M., and Pourmand A. (2011) A new method for MC-ICPMS measurement of Ti isotopic composition: identification of correlated isotope anomalies in meteorites. *J. Anal. At. Spectrom.* **26**, 2197-2205.

Zhang J., Dauphas N., Davis A. M., Leya I. and Fedkin A. (2012) The proto-Earth as a significant source of lunar material. *Nature Geoscience* **5**, 251–255.

Zolensky M. E., Ivanov A. V., Yang S. V., Mittlefehldt D. W., and Ohsumi K. (1996) The Kaidun meteorite: Mineralogy of an unusual CM1 lithology. *Meteoritics & Planetary Science* **31**, 484-493.